High Fidelity Measurement Methodology of Turbulent Wall-bounded Flow Structures

by

Bihai Sun

Bachelor of Aerospace Engineering (Honours)

Supervisor: Prof. Julio Soria
Associate Supervisor: Dr. Callum Atkinson

A thesis submitted for the degree of Master of Engineering Science (Research) at Monash University in 2021

Laboratory for Turbulence Research in Aerospace and Combustion (LTRAC)
Department of Mechanical and Aerospace Engineering
Faculty of Engineering
Monash University

Copyright notice

Abstract

The identification and characterisation of coherent structures in turbulent flows have been an active area of research for decades. Coherent structures have a strong association with the production of turbulent kinetic energy, as well as the transfer of turbulent kinetic energy between different scales in the turbulent flow, which makes them the key to understand the physics behind the turbulent flows. However, due to the highly three-dimensional nature of coherent structures, traditional flow measurement techniques, such as 2C-2D PIV, can only lead to a limited understanding of them.

This thesis aims to develop a holographic based PIV measurement technique, termed 4D-DHPIV/PTV, which can produce time-resolved three-component three-dimensional velocity field measurements. The in-line 4D-DHPIV/PTV methodology builds on the standard digital hologram reconstruction and incorporates advanced digital filtering to remove the virtual image effect, 3-dimensional volume deconvolution to reduce the depth-of-focus problem and the virtual image, followed by an efficient one-pass 3-dimensional clustering algorithm coupled with a predictive inverse reconstruction approach to increase the particle reconstruction dynamic range and 3-dimensional reconstruction domain. The last step is accelerated using particle position prediction. In addition to the presentation of the details of this novel 4D-DHPIV/PTV method, performance results pertaining to bias particle position error and the uncertainty associated with the particle position are presented as a function of: (i) particle concentration and (ii) the shot noise present in the digitally recorded hologram. An experiment to measure a laminar micro-channel flow has been performed to demonstrate the 4D-DHPIV/PTV methodology.

The second part of the thesis is a consequence of the inability of carrying out the laboratory experiments using 4D-DHPIV/PTV due to COVID-19 restrictions. In this second part of the thesis, high spatial resolution (HSR) 2 component 2-dimensional (2C-2D) PIV of a zero pressure gradient (ZPG) turbulent boundary layer (TBL) in air as the basis to extract large scale motions from the measured velocity fields, as well as analyse the relationship between the wall friction and the large scale motions. A large sensor is used in the PIV experiment, that introduces a lens distortion error in the PIV measurement, therefore ,a method to correct those errors has been developed, which is analysed and discussed. The velocity field data set is analysed using proper orthogonal decomposition (POD) to extract the large scale motions from the velocity fields. A convergence analysis is performed to study the number of snapshots needed for a POD that faithfully represents the flow structures in the flow. Furthermore, the Renard-Deck decomposition of the wall skin friction coefficient is applied to study the effect of the presence of large scale motions in the flow via their conditional Reynolds shear stress contributions on the wall skin friction coefficient.

Publications during enrolment

- Journal papers:
  - Bihai Sun, Asif Ahmed, Callum Atkinson, and Julio Soria. A novel 4D digital holographic PIV/PTV (4D-DHPIV/PTV) methodology using iterative predictive inverse reconstruction. *Measurement Science and Technology*, 31(10):104002, 7 2020. doi: 10.1088/1361-6501/ab8ee8. URL https://doi.org/10.1088/1361-6501/ab8ee8
  - Bihai Sun, Muhammad Shehzad, Daniel Jovic, Christophe Cuvier, Christian Willert, Yasar Ostovan, Jean-Marc Foucaut, Callum Atkinson, and Julio Soria. Distortion correction of two-component – two-dimensional piv using a large imaging sensor with application to measurements of a turbulent boundary layer flow at $Re_\tau = 2,386$. *Experiment in Fluids*, 2021
  - Muhammad Shehzad, Bihai Sun, Daniel Jovic, Christophe Cuvier, Christian Willert, Yasar Ostovan, Jean-Marc Foucaut, Callum Atkinson, and Julio Soria. Investigation of large scale motions in zero and adverse pressure gradient turbulent boundary layers using high-spatial-resolution PIV. *Experimental Thermal and Fluid Science*, 2021
- Conference papers:
  - Julio Soria, Bihai Sun, Asif Ahmed, and Callum Atkinson. 4D digital holographic PIV/PTV with 3D volume deconvolution and predictive inverse reconstruction. In *13th International Symposium on Particle Image Velocimetry*, Jul 2019
  - Bihai Sun, Asif Ahmed, Callum Atkinson, and Julio Soria. Using a new 4D digital holographic PIV/PTV (4D-DHPIV/PTV) methodology to measure wall-bounded shear flows. In *13th International Symposium on Particle Image Velocimetry*, Jul 2019
  - Bihai Sun, Asif Ahmed, Callum Atkinson, and Julio Soria. The effect of shot noise on the accuracy of particle positions in hologram reconstruction using an inverse method. In *IX Australian Conference on Laser Diagnostics*, Dec 2019
  - Asif Ahmed, Bihai Sun, Victor J. Cadarso, Callum Atkinson, and Julio Soria. Enhancing digital holographic microscopic PIV by exploiting the contrast inversion property of weak scattering tracer particles. In *IX Australian Conference on Laser Diagnostics*, Dec 2019
  - Asif Ahmed, Bihai Sun, Victor J. Cadarso, and Julio Soria. 3D localization of the tracer particles in digital inline holographic microscopy PIV/PTV: do the bright regions in the intensity reconstruction volume really correspond to the tracer particles? In *73rd Annual Meeting of the APS Division of Fluid Dynamics*, Nov 2020

Declaration

This thesis contains no material which has been accepted for the award of any other degree or diploma at any university or equivalent institution and that, to the best of my knowledge and belief, this thesis contains no material previously published or written by another person, except where due reference is made in the text of the thesis.

Signature: [Signature hidden for archiving]

Print Name: Bihai Sun

Date: 25 June, 2021

Acknowledgements

Throughout my Master by research journey, I have received enormous help from many people around me. I would like to take this opportunity to thank everyone along the way, it is your support that make it possible for me to learn so much in my degree.

First, I would like to express my deep and sincere gratitude to my supervisors, Prof. Julio Soria and Dr. Callum Atkinson. Your expertise and guidance were invaluable, and you have put in much effort from shaping the overall structure of the project to solving day-to-day research problems. Thank you very much for bringing me in front of the mystery and the greatness of nature and babysitting me in my early research life. I hope you are glad that the baby you have been taken care of can now start to crawl onto the research road.

I also would like to thank my colleges from LTRAC, especially the co-authors of my papers, Mr. Asif Ahmed, Mr. Muhammud Shehzad and Mr. Daniel Jovic. We had many valuable discussions, and you gave me many great suggestions for my research. I want to especially thank you for your patience when reviewing my (poorly written) manuscripts, including the chapters of this thesis.

In addition, I want to thank my international collaborators, who are Dr. Christian Willert from German Aerospace Center, also Prof. Jean-Marc Foucaut, Prof. Christophe Cuvier and Dr. Yasar Ostovan from Laboratory of Fluid Mechanics of Lille - Kampé de Fériet. You have provided world-class state-of-art researching facilities and offered great help in conducting the measurement in the wind tunnel. I had a very enjoyable and fruitful research journey in France.

I also received much help from the technical staffs from Monash University mechanical and aerospace engineering workshop, especially Mr. Chris Pierson and Mr. Nat DeRose. I learnt a lot of the mechanical design and manufacturing knowledge from you, and your works in making customised parts for my experiment were prompt, precise and of high quality.

I also want to thank my families and friends in Australia and China. I've received much care and accompany from you, and I couldn't survive the research life without you constantly cheering me up and caring for me.

Finally, this research was supported by an Australian Government Research Training Program (RTP) Scholarship. Part of the funding is also provided by the faculty of Engineering, Monash University.

Contents

List of Figures

List of Tables

Chapter 1

Introduction

Although the year 2021 marks the 117th anniversary of the introduction of boundary layer theory by Ludwig Prandtl [9], to this date the study of the turbulent flow in the boundary layer is still an active area of research. The difficulty in understanding turbulent flow arises from its chaotic nature, and indeed turbulence was deemed a purely chaotic motion that could only be described statistically in the early days of the study of turbulence. However, Kline et al. [10] discovered that there are regions in the turbulent boundary layer flow where the velocity is relatively constant compared to the rest of the flow, which were referred to as "structures" in the turbulent flow. Since then, the study of these flow structures, also referred to as coherent structures began, in addition to the statistical quantification of the turbulent flow.

A more recent definition of coherent structures is provided by Robinson [11], who defined them as "*a three-dimensional region of the flow over which at least one fundamental flow variable (such as velocity component, density, temperature) exhibits significant correlation with itself or with another variable over a range of space and/or time that is significantly larger than the smallest local scales of the flow.*" The existence of the coherent structures in turbulent flow was not only confirmed by experiments as subsequent studies showed, but also can be inferred from the fundamental equations of fluid mechanics.

Considering the Reynolds decomposition of the Navier-Stokes equation, the evolution equation of the turbulent kinetic energy can be derived as,

$$\frac{\partial k}{\partial t} + U_j \frac{\partial k}{\partial x_j} = -\frac{1}{\rho_o} \frac{\partial \langle u_i' p' \rangle}{\partial x_i} - \frac{1}{2} \frac{\partial \langle u_j' u_j' u_i' \rangle}{\partial x_i} + \nu \frac{\partial^2 k}{\partial x_j^2} - \langle u_i' u_j' \rangle \frac{\partial U_i}{\partial x_j} - \nu \langle \frac{\partial u_i'}{\partial x_j} \frac{\partial u_i'}{\partial x_j} \rangle, \quad (1.1)$$

where k, p and ν represents the specific turbulent kinetic energy, pressure and viscosity, respectively. U_i represents the mean velocity in the i^{th} direction, and u'_i represents the fluctuating velocity in the i^{th} direction. In equation 1.1, the terms $\langle u'_i u'_j \rangle \frac{\partial U_i}{\partial x_j}$ and $\nu \langle \frac{\partial u'_i}{\partial x_j} \frac{\partial u'_i}{\partial x_j} \rangle$ are identified as the turbulent production and dissipation terms, respectively [12]. Therefore, the correlation between velocity fluctuations, $\langle u'_i u'_j \rangle$, plays an essential role in turbulence production as it does in turbulent momentum transportation. If turbulence were purely random, there would be no correlation between the velocity fluctuations, and thus, no means of sustaining turbulence. This suggests there must be regions in the boundary layer, i.e. the coherent structures, where the correlation between velocity components is high.

Furthermore, scale analysis of the production and dissipation reveals a transfer of energy between large scales and small scales in the turbulent flow, known as the cascade of energy [13, 14]. As the production term has a larger scale than the dissipation term, the majority of energy is transferred from large scale to small scale [12]. Also, coherent structures in the turbulent flow are associated with production and are relatively of large scale in size and time, so that the evolution and breakup of those structures is an important mechanism to transfer energy between different scales in a turbulent flow.

Therefore, the study of coherent structures can explain how turbulence is produced, its energy transferred to smaller scales and ultimately dissipated. The understanding of coherent structures will be a significant step towards the understanding of turbulent flow.

This thesis explores two high-fidelity coherent structure measurement, identification and characterisation methodologies. The first one is based on four-dimensional digital holographic particle image velocimetry and particle tracking velocimetry (4D-DHPIV/PTV), which extends commonly used 2-component – 2-dimensional (2C-2D) velocity measurements to the third component and the third dimension, whereas the second one is based on high spatial resolution 2C-2D particle image velocimetry (2C-2D PIV), which achieves a measurable range of length scales from the boundary layer thickness to about ten viscous length scales to be resolved. The COVID-19 environment during 2020 restricted and finally stopped all experimental work, which results in that the 4D-DHPIV/PTV technique not being able to be applied to a turbulent boundary layer flow. The 4D-DH PIV/PTV technique was then restricted to its development and its investigation pertaining to accuracy and suitability to capture flow structures based on numerical simulated data and measurements of a laminar channel flow.

This thesis is organised into five chapters. Chapter 2 reviews some basic concepts of turbulent boundary layer, coherent structures in the turbulent boundary layer, the current technologies to measure coherent structures. Chapter 3 introduces the novel four-dimensional digital holographic PIV/PTV methodology developed to measure 3C-3D time resolved velocity field and capture coherent structures. Chapter 4 applies 2C-2D PIV to measure the HSR velocity fields of a high Reynolds number turbulent boundary layer flow. Proper orthogonal decomposition (POD) and conditional statistics are used to study the contribution of coherent structures, and more specifically the large scale motions, to wall skin friction. Chapter 5 concludes the study in this thesis.

Chapter 2

Literature Review

2.1 Turbulent Boundary Layer

Turbulent boundary layer is one of the simplest but also most common flow phenomenons. The concept of the boundary layer was first suggested by Plantl in 1904 [9], who theorised that one effect of friction is to adhere the the wall with the fluid immediately adjacent to it (i.e., no-slip condition), and the effect of friction only presents within a thin layer of fluid near the wall, which is called the boundary layer. In this thesis, a simplified model of boundary layers is considered, where the following assumptions are made:

- The fluid is a continuum and is incompressible.
- The wall is flat, smooth, adiabatic, infinitely-long in the spanwise and streamwise directions, and aligned with the free-stream flow. Therefore the flow can be considered 2 dimensional in the wall-normal – streamwise directions and statistically homogeneous in the spanwise direction.
- At the wall, the fluid velocity is zero.
- The free-stream flow is turbulence-free.
- Before the boundary layer develops, the incoming flow has constant velocity, which value is the same as the free-stream velocity and with no turbulence.

A schematic drawing of the boundary layer flow is shown in figure 2.1, where x, y and z axis are aligned with the streamwise, wall-normal and spanwise directions, the velocity in x, y and z directions are denoted as u, v, and w, also the free stream velocity is denoted by U_0 in x direction and V_0 in y direction. The boundary layer flow can be under the condition of zero pressure gradient (ZPG-TBL) $\left(\frac{\partial P}{\partial x}=0\right)$, adverse pressure gradient (APG-TBL) $\left(\frac{\partial P}{\partial x}>0\right)$, or favourable pressure gradient (FPG-TBL) $\left(\frac{\partial P}{\partial x}<0\right)$. In Chapter 4 of this thesis, a study using a high resolution 2C-2D PIV experiment to study a zero-pressure-gradient turbulent boundary layer developing on a flat plate is presented.

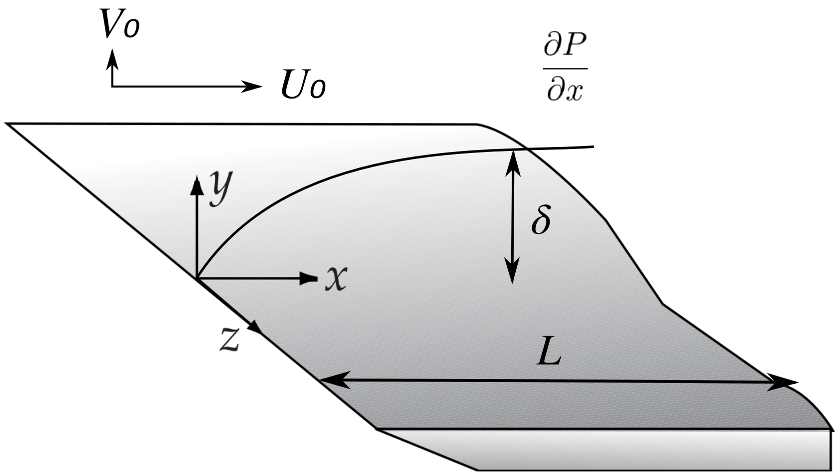

Figure 2.1: Schematic drawing of the boundary layer flow [12].

In this section, some basic concepts and discussions of the turbulent boundary layer is presented. For a more complete description and discussion, please refer to the book on turbulent flows by Pope [12].

2.1.1 Thin shear layer equation

Because the thickness of the boundary layer is much smaller than the length of the plate, the Navier-Stokes equation can be simplified via a order of magnitude analysis. Considering the 2-dimensional incompressible Navier-Stokes equation,

$$\begin{cases} \dfrac{\partial u}{\partial x}+\dfrac{\partial v}{\partial y}=0 \\ u\dfrac{\partial u}{\partial x}+v\dfrac{\partial u}{\partial y}=-\dfrac{1}{\rho}\dfrac{\partial p}{\partial x}+\nu\left(\dfrac{\partial^2 u}{\partial x^2}+\dfrac{\partial^2 u}{\partial y^2}\right) \\ u\dfrac{\partial v}{\partial x}+v\dfrac{\partial v}{\partial y}=-\dfrac{1}{\rho}\dfrac{\partial p}{\partial y}+\nu\left(\dfrac{\partial^2 v}{\partial x^2}+\dfrac{\partial^2 v}{\partial y^2}\right) \end{cases} \tag{2.1}$$

From the continuity equation, as there are only two terms, they must have similar magnitude, therefore,

$$\mathcal{O}\left(\frac{U_0}{L}\right) = \mathcal{O}\left(\frac{V_0}{\delta}\right) \tag{2.2}$$

Thus, the streamwise component of the free stream velocity is much smaller than the wall-normal component. The order of magnitude analysis of the momentum equation in x direction yields,

$$\begin{array}{ccccccccc} u\dfrac{\partial u}{\partial x} & + & v\dfrac{\partial u}{\partial y} & = & -\dfrac{1}{\rho}\dfrac{\partial p}{\partial x} & + & \nu\dfrac{\partial^2 u}{\partial x^2} & + & \nu\dfrac{\partial^2 u}{\partial y^2} \\ \mathcal{O}\left(\dfrac{U_0^2}{L}\right) & & \mathcal{O}\left(\dfrac{U_0^2}{L}\right) & & & & \mathcal{O}\left(\dfrac{\nu U_0}{L^2}\right) & & \mathcal{O}\left(\dfrac{\nu U_0}{\delta^2}\right) \end{array} \tag{2.3}$$

So the second viscous term dominates over the first viscous term, and the first viscous term can be neglected. Also, as viscosity is observed to have an effect on the boundary layer flow, the viscous term should have the same order of magnitude as the advection term. Therefore, the order of magnitude of viscosity is,

$$\mathcal{O}(\nu) = \mathcal{O}\left(\frac{U_0\delta^2}{L}\right) \tag{2.4}$$

Lastly, the order of magnitude analysis of the momentum equation in y direction yields,

$$\begin{array}{ccccccccc} u\dfrac{\partial v}{\partial x} & + & v\dfrac{\partial v}{\partial y} & = & -\dfrac{1}{\rho}\dfrac{\partial p}{\partial y} & + & \nu\dfrac{\partial^2 v}{\partial x^2} & + & \nu\dfrac{\partial^2 v}{\partial y^2} \\ \mathcal{O}\left(\dfrac{U_0^2\delta}{L^2}\right) & & \mathcal{O}\left(\dfrac{U_0^2\delta}{L^2}\right) & & & & \mathcal{O}\left(\dfrac{\nu U_0^2\delta}{L^2}\right) & & \mathcal{O}\left(\dfrac{\nu U_0^2\delta}{L^2}\right) \end{array} \tag{2.5}$$

Here every term is negligible compared to the corresponding term in the momentum equation in x direction. Therefore, for boundary layers, the two-dimensional Navier-Stokes equation can be reduced to the boundary layer equations,

$$\begin{cases} \dfrac{\partial u}{\partial x} + \dfrac{\partial v}{\partial y} = 0 \\ u\dfrac{\partial u}{\partial x} + v\dfrac{\partial u}{\partial y} = -\dfrac{1}{\rho}\dfrac{\partial p}{\partial x} + \nu\dfrac{\partial^2 u}{\partial y^2} \\ \dfrac{\partial p}{\partial y} = 0 \end{cases} \tag{2.6}$$

2.1.2 Reynolds decomposition

In 1885, Osborne Reynolds proposed that the fluid motion can be decomposed into averaged component and fluctuating component, which is later named Reynolds decomposition [15]. In the thesis, the mean values will be denoted by capital letters, the fluctuation values will be denoted by letters with superscript prime, and the averaging operation will be denoted by angled brackets. For example, the Reynolds decomposition of the streamwise velocity, u, is,

$$u = \langle u \rangle + u' = U + u' \tag{2.7}$$

Applying Reynolds decomposition to the Navier-Stokes equation and then taking the average yields the Reynolds averaged Navier-Stokes equation (RANS), and for two-dimensional incompressible flow, the RANS reduces to,

$$\begin{cases} \dfrac{\partial U}{\partial x} + \dfrac{\partial V}{\partial y} = 0 \\ U\dfrac{\partial U}{\partial x} + V\dfrac{\partial U}{\partial y} = -\dfrac{1}{\rho}\dfrac{\partial P}{\partial x} + \nu\dfrac{\partial^2 U}{\partial x^2} + \nu\dfrac{\partial^2 U}{\partial y^2} - \dfrac{\partial \langle u'^2 \rangle}{\partial x} - \dfrac{\partial \langle u'v' \rangle}{\partial y} \\ U\dfrac{\partial V}{\partial x} + V\dfrac{\partial V}{\partial y} = -\dfrac{1}{\rho}\dfrac{\partial P}{\partial y} + \nu\dfrac{\partial^2 V}{\partial x^2} + \nu\dfrac{\partial^2 V}{\partial y^2} - \dfrac{\partial \langle u'v' \rangle}{\partial x} - \dfrac{\partial \langle v'^2 \rangle}{\partial y} \end{cases} \tag{2.8}$$

Comparing equation 2.8 and equation 2.1, the additional terms in 2D-RANS are the Reynolds stresses, $\langle u'^2 \rangle$, $\langle u'v' \rangle$ and $\langle v'^2 \rangle$. The Reynolds stresses greatly alter the flow behaviour and act as a bridge to transfer energy between the mean flow and the fluctuating flow, therefore it's essential to study their behaviour in the turbulent flows. The Reynolds normal stresses are also components of the turbulent kinetic energy of flow, which is defined as

$$k = \frac{1}{2}\left(\langle u'^2 \rangle + \langle v'^2 \rangle + \langle w'^2 \rangle\right) \tag{2.9}$$

in three-dimensional flows.

Applying the order of magnitude analysis introduced in section 2.1.1, the terms with grey color in equation 2.8 can be neglected when turbulent boundary layer is considered. In addition, the fluctuation velocity in all directions have the same order of magnitude, so the $\partial/\partial x$ terms are neglectable compared to the $\partial/\partial y$ terms. Therefore, the Reynolds averaged boundary layer equation is,

$$\begin{cases} \dfrac{\partial U}{\partial x} + \dfrac{\partial V}{\partial y} = 0 \\ U\dfrac{\partial U}{\partial x} + V\dfrac{\partial U}{\partial y} = -\dfrac{1}{\rho}\dfrac{\partial P}{\partial x} + \nu\dfrac{\partial^2 U}{\partial y^2} - \dfrac{\partial \langle u'v' \rangle}{\partial y} \\ \dfrac{1}{\rho}\dfrac{\partial P}{\partial y} = \dfrac{\partial \langle v'^2 \rangle}{\partial y} \end{cases} \tag{2.10}$$

2.1.3 Scales in turbulent boundary layers

At different regions of the turbulent boundary layer, the behaviour of the flow is dominated by different mechanisms. Near the wall, the flow is dominated by viscous force, so the velocity profile is only a function of viscous-force-related quantities, which are fluid density (ρ), fluid viscosity (ν) and wall shear stress (τ_w). This region is called the inner layer of the turbulent boundary layer, and typically occupies from the wall up to 0.1δ. According to Buckingham Π theorem [16], as there are 5 free variables defined in three dimensions, they can be re-arranged to a set of dimensionless parameters. Following a dimensional analysis, the following quantities can be defined,

$$\begin{aligned} \text{Friction velocity } u_\tau &= \sqrt{\frac{\tau_w}{\rho}} \\ \text{Viscous length scale } l^+ &= \frac{\nu}{u_\tau} \end{aligned} \tag{2.11}$$

This scale is called inner scale or friction scale, and the flow variables can be non-dimensionalised by inner scale as,

$$\begin{aligned} u^+ &= \frac{u}{u_\tau} \\ y^+ &= \frac{y}{l^+} = \frac{y u_\tau}{\nu} \\ \langle u'^2 \rangle^+ &= \frac{\langle u'^2 \rangle}{u_\tau^2} \\ Re_\tau &= \frac{u_\tau \delta}{\nu} = \frac{\delta}{l^+} = \delta^+ \end{aligned} \tag{2.12}$$

The mean velocity profile of a turbulent boundary layer in the inner scale is shown in figure 2.2.

The figure shows that for different Reynolds number the mean velocity profile collapse well. In addition, two other distinct layers are observable from the figure. Below $y^+ = 5$, there is a linear relationship between the velocity and distance from the wall, which is called viscous sublayer. In this layer the effect of Reynolds stress is so small that the total stress is approximately constant and equal to wall shear stress for the whole layer.

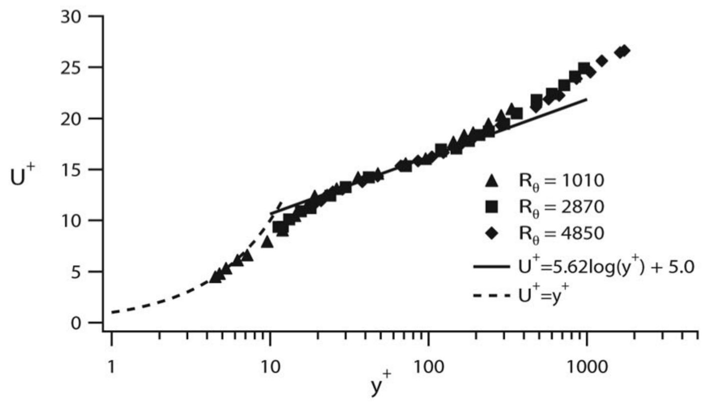

Figure 2.2: Mean velocity profiles of turbulent boundary layers scaled by inner scale [17].

There exist another layer where the velocity profile is roughly a logarithm function. This layer is called log layer and it extends roughly from $y^+ = 30$ to the end of inner layer. Between the log layer and the viscous sublayer is the buffer layer, which smoothly connect the two layers.

The Reynolds stress profiles of the turbulent boundary layer is shown in figure 2.3

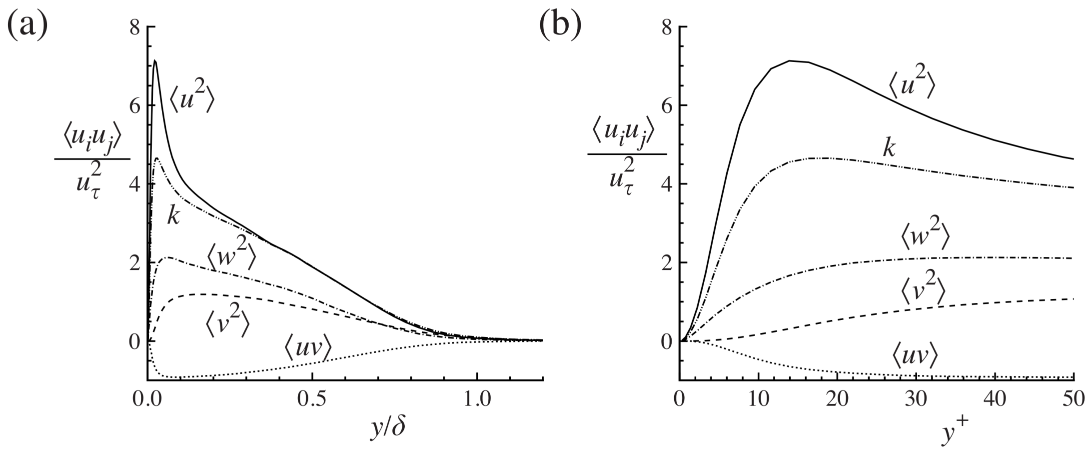

Figure 2.3: Profiles of Reynolds stresses and kinetic energy normalized by the friction velocity in a turbulent boundary layer at $Re_\theta = 1,410$ (a) across the boundary layer and (b) in the viscous near-wall region [18].

The figure shows that the streamwise velocity has the highest fluctuation, followed by spanwise velocity then wall-normal velocity,the highest values of all Reynolds stresses occur in the inner layer of the turbulent boundary layer.

2.1.4 Alternative definitions of boundary layer thickness

The boundary layer thickness is used to describe the wall-normal location which the flow is no longer effected by the wall friction. However, as the mean velocity profile approaches asymptotically to the free-stream velocity, it is not possible to find a point where the mean streamwise velocity equals to the free-stream velocity. Therefore, the boundary layer thickness is defined when the mean velocity is "closer enough" to the free-stream velocity at, rather arbitrary, 99 percent of the free-stream velocity, i.e., δ_{99}. This definition is not only poorly justified by physics, but also difficult to be precisely measured due to the small velocity differences. Thus, there are some other definitions of boundary layer thickness based on integral measurements.

The displacement thickness is defined by,

$$\delta^* = \int_0^\infty \left(1 - \frac{U}{U_\infty}\right) \mathrm{d}y \tag{2.13}$$

It represents the distance that the wall need to be moved, so that the flow rate is the same for an inviscid flow over the wall, and is graphically illustrated by figure 2.4.

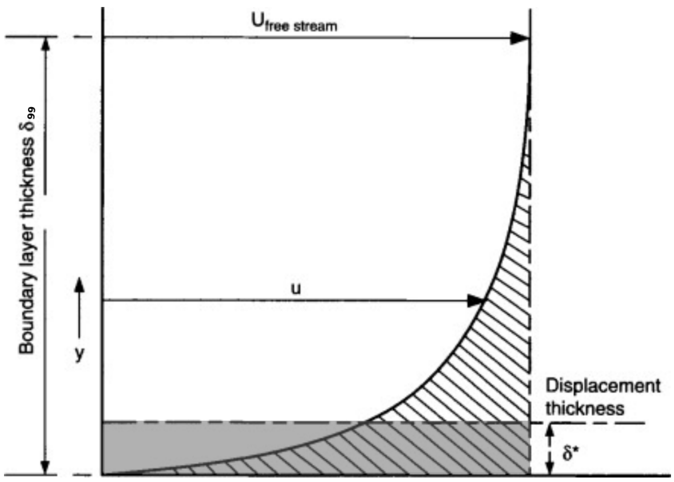

Figure 2.4: Bounday layer flow velocity profile showing the boundary layer thickness and displacement thickness. The shaded area has the same size as the gray area. [19].

Similarly, the momentum thickness is defined by,

$$\theta = \int_0^\infty \frac{U}{U_\infty} \left(1 - \frac{U}{U_\infty}\right) \mathrm{d}y \tag{2.14}$$

It represents the distance that the wall need to be moved, so that the momentum flux is the same for an inviscid flow over the wall. Based on those two thickness, the shape factor is defined as the ratio between displacement and momentum thickness,

$$H = \frac{\delta^*}{\theta} \tag{2.15}$$

And the Reynold number based on the momentum thickness is

$$Re_\theta = \frac{\rho u \theta}{\mu} \tag{2.16}$$

2.2 Flow structures reported in the literature

Numerous numerical and experimental studies have revealed a range of flow structures that might be of importance in producing turbulence kinetic energy. The structures observed have various sizes and shapes, and there are no universal definitive criteria to separate one from another. Nevertheless, a selection of typical flow structures occurring in wall-bounded turbulent flow are described in this section, which include Λ-vortex, soliton-like coherent structures, hairpin vortices, hairpin packets, low speed streaks, typical eddies and large scale motions.

A Λ-vortex is a vortex line bent into the shape of the letter Λ, as shown in figure 2.5. This structure was first observed by Hama [20] and is typically found in the later stages of transition from laminar to turbulent flow. They are essential structures that introduce further disturbance into the flow and transform into more energetic structures as the flow becomes more turbulent [21]. A hypothesis to explain the formation of Λ-vortex is provided by Theodorsen [22], which states: a two-dimensional vortex line in the spanwise direction is partially lifted off from the wall due to the natural disturbance, and interacts with higher velocity fluid further away from the wall. As the vortex line is stretched by the faster-moving fluid, it forms a Λ shape, thus a Λ-vortex is created.

Solitonlike coherent structures (SCS) are another kind of coherent flow structures that often occur simultaneously with the Λ-vortices, as seen in figure 2.5. SCS has a similar behaviour as a soliton; it is a wave packet that can travel long distances with the flow with little change in shape and amplitude. Lee [23] provides an extensive investigation of the SCS, where he reports that the wave speed of SCS is about 60% to 80% of the free stream velocity, which is lower than the surrounding fluid. Thus, the fluid directly downstream of the SCS moves from free stream towards the wall, while the fluid upstream of the SCS is pushed away from the wall. A strong shear layer is created during this process, which is necessary for the formation of the Λ- vortex. This alternative hypothesis of the generation of Λ- vortex is also widely accepted [24].

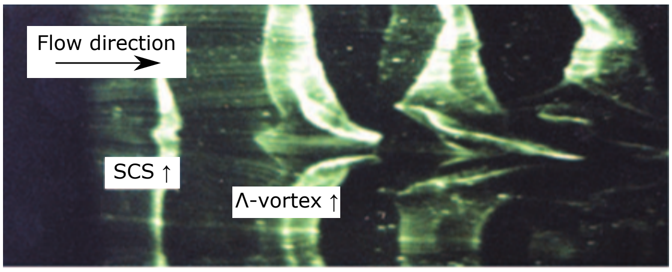

Figure 2.5: Visualisation of solitonlike coherent structures appearing upstream of a Λ-vortex. [23]

Hairpin vortices are vortex structures of the shape with a hairpin, having a round head and a pair of counter-rotating quasi-streamwise vortices, also called "legs", near the wall [11]. As the Reynolds number increase, their shape changes from arch-like to a horseshoe shape and then hairpin, as shown in figure 2.6. Hairpin vortices were first observed by Head and Bandyopadhyay [25]. They are the dominant vortical coherent structures in late transition stages and have an essential role in turbulent production [26]. Because of the counter-rotating vortex in the hairpin vortex legs, the flow is swept upwards within the head and between the necks of the hairpin vortices. Since the hairpin vortices are inclined relative to the wall, this stream flows to the wall-normal and upstream direction. In the meantime, outside the head of the hairpin vortices, high-speed fluid away from the wall is pushed to the near-wall region. These are called ejection and sweep events and are directly related to Reynolds shear stress and thus to the production term in the energy budget of turbulent kinetic energy [27]. One theory of the generation of hairpin vortices, suggested by Theodorsen [22], is that the shear layer stretches the Λ-vortex in the flow, and the tip of the Λ-vortex rolls up, forming the head of the hairpin vortex. This process was illustrated in a DNS simulation performed by Yan [21].

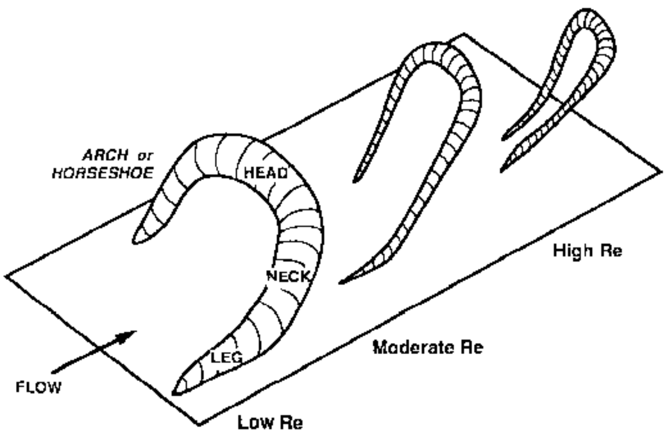

Figure 2.6: The shape of hairpin vortex in different Reynolds number [11]

Hairpin packets are compound flow structures that consist of multiple hairpin structures moving at the same speed as a packet. The presence of hairpin packets is believed to be the result of the self-generation of the hairpin vortices [28, 29]. Adrian et al. [30]

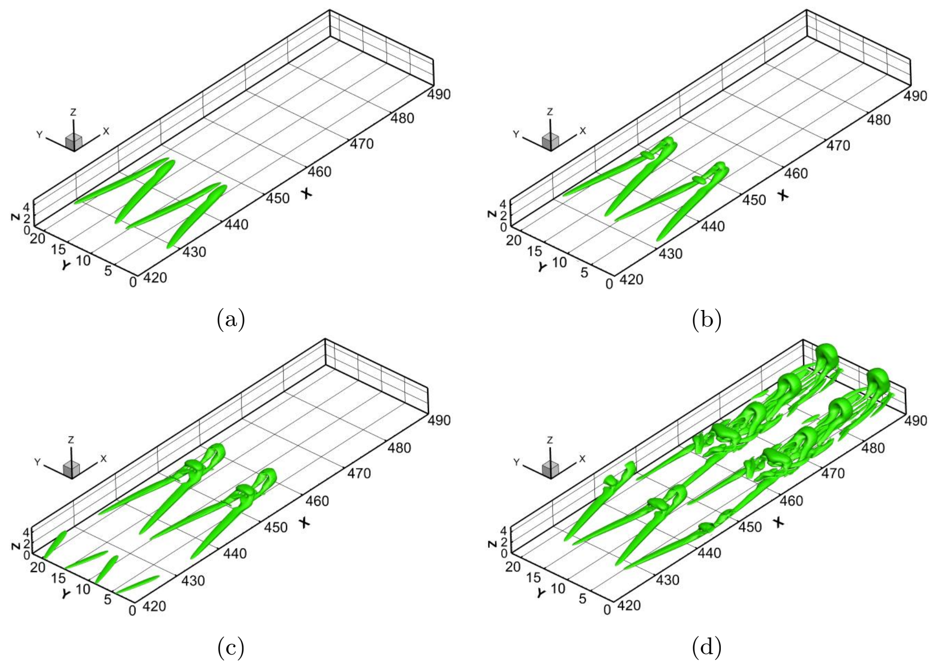

Figure 2.7: Time series of Ω contour of a DNS simulation, showing Λ-vortices a) transforming to hair-pin vortices d) [21]

summarised the experiment and simulation available [31–33] and proposed the hairpin packet structure as shown in figure 2.8, consisting three hairpin packets. The newest packet in the three is also the smallest and moves the slowest downstream. However, because of the smaller size, the newer hairpin packets produce a stronger low speed streak. There are also some hairpin vortices located further away from the wall that are not part of this packet, suggesting that other mechanisms are also capable of producing hairpin vortices in other parts of the boundary layer. The insert on the top left corner in figure 2.8 shows how the hairpin vortices are organised inside each hairpin packets so that the hairpin vortices' heads form a straight line with angle γ relative to the wall.

Low speed streaks (LSS) are elongated regions of lower local speed near the wall in a turbulent boundary layer. They are usually of the order of 1000 viscous units in length and are spaced apart in the spanwise direction by around 100 viscous lengths. Between the low speed streaks, there are regions of flow speed higher than the mean [34]. They were first reported by Hama [20] and are one of the first discovered and studied coherent structures. It is generally believed that LSSs are caused by long counter-rotating vortices [24], where the vortices may come from: i) the lifting-up of the hairpin-like structures, ii) stretched and lifted vortex flow lines [10], iii) an upflow between the legs of hairpin vortices [25], or iv) uniform momentum zones induced by hairpin vortices. However, there is also evidence showing that not all LSSs are the result of vortex structures. Kim and Lim [35] showed, using simulations, the importance of $v' \frac{\partial U}{\partial y}$ term in the generation

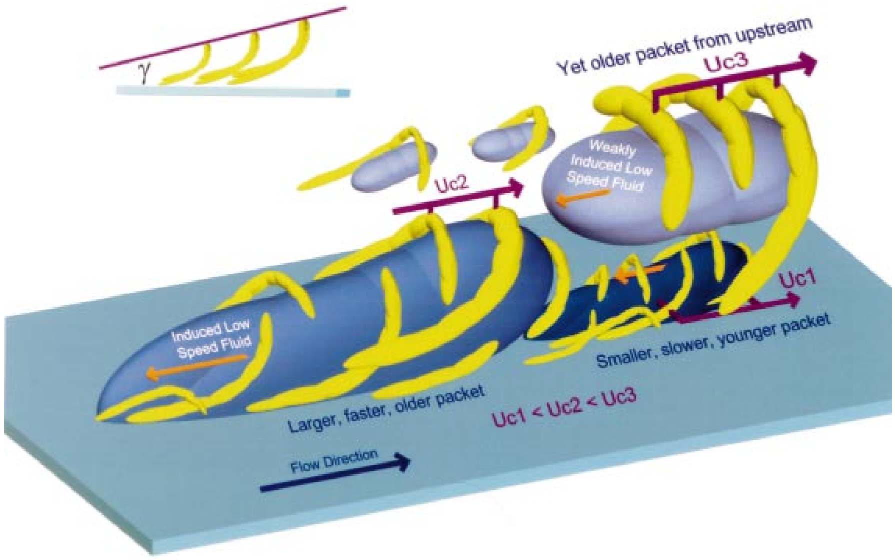

Figure 2.8: Conceptual scenario of hairpins packets growing up from the wall [30]. The dark cyan plate represents the wall, the yellow streaks represent the hairpin vortices, and blue streaks represent the low speed streaks induced by the hairpin packets, with darker colour meaning a stronger streak.

of LSSs, where v' represents the fluctuating wall-normal velocity, and $\frac{\partial U}{\partial y}$ represents the mean streamwise velocity gradient in the wall-normal direction. Lee and Wu [23] also suggest that LSS can be formed by soliton-like coherent structures. An important phenomenon associated with LSS is bursting. Kim et al. [36] provide a model of the bursting process of low speed streaks. The first stage of bursting is a LSS moving off the wall. At first, the LSS lifts slowly off the wall over a large extent of the streamwise direction, and then, after reaching some critical height, the LSS starts to turn much quicker away from the wall while moving downstream. This stage is referred to as low-speed-streak-lifting or, for brevity, streak-lifting. As the LSS lifts from the wall, the low-speed fluid is carried with it, producing an ejection event. In the second stage of bursting, at the end of lifted-up of the LSS, there is an oscillating motion that lasts for around three to ten oscillation cycles with increased size. The third and last stage of the bursting process is the breakup of the oscillating motion, when it is substituted by a more random chaotic motion. The three stages of the bursting of LSS are graphically illustrated in figure 2.10. Sweeps and ejections are important fluid motions in the bursting process, and they are also the main contributor to the turbulent momentum transportation and turbulence generation. Thus bursting events are essential for the study of turbulence in wall-bounded fluid flows.

Typical eddies are local compact regions of high vorticity concentration that occur in the outer area of the boundary layer. They were first discovered and studied by Falco [38]. The size of the typical eddies, which depends on Reynolds number, can be nearly

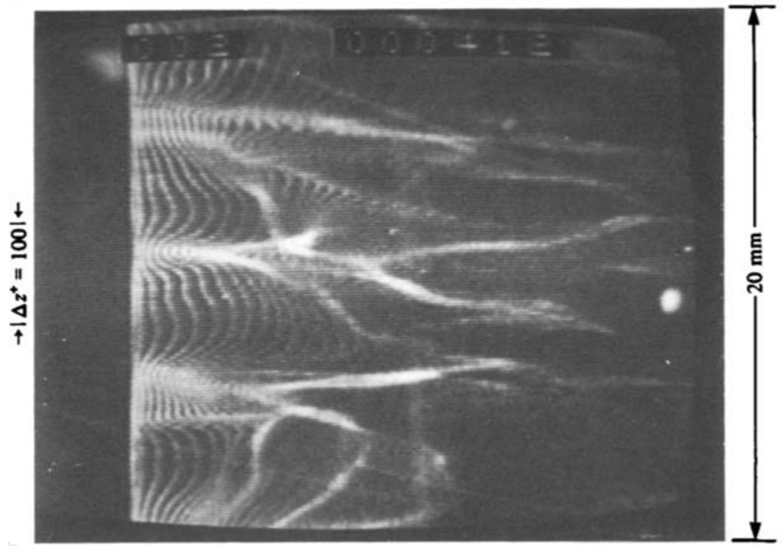

Figure 2.9: Low speed streaks visualised by hydrogen bubbles showing the typical width of the low speed streaks in turbulent boundary layer flow. [37]

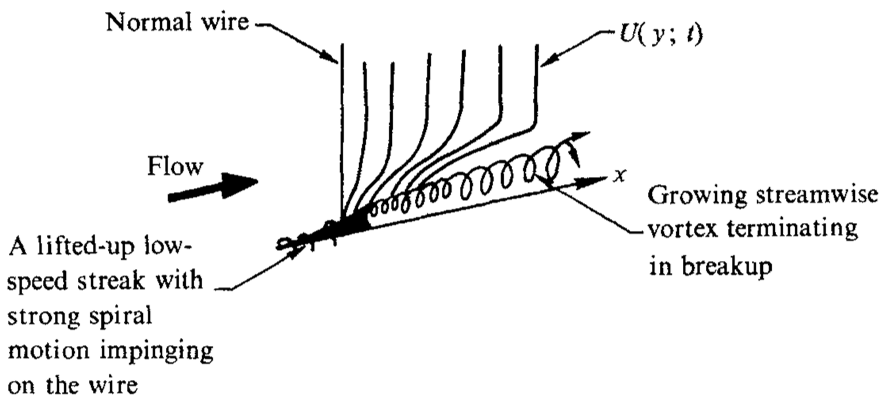

Figure 2.10: Three stages of the bursting event of low speed streak: 1) streak-lifting 2) oscillation motion 3) breakup of oscillation [36]

the boundary layer's size at low Reynolds number and much smaller at high Reynolds number, as shown in figure 2.11. It was also observed that the typical eddies contribute to the majority of Reynolds stresses in the outer region of the flow, where their contribution drops as the Reynolds number increases with the size of the typical eddies dropping much faster than their contribution to the Reynolds stress. The typical eddies are in the form of vortex rings at low and moderate Reynolds numbers, but they are highly disturbed by the turbulence at high Reynolds numbers. There are two major mechanisms of the formation of typical eddies. One mechanism is the pinch-up and reconnection of hairpin vortices lifting off from the wall, and the other equally likely mechanism is the instability of a region of fluid with high vorticity facing an external force [39]. Typical eddies produce Reynolds stress in the outer flow and promote the occurrence of near-wall flow structures such as the ejection-sweep behaviour, and the packets and hairpin vortices [40].

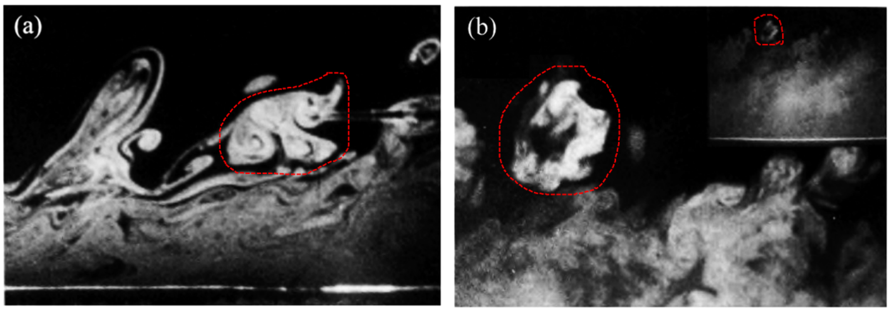

Figure 2.11: Photographic of typical eddies in turbulent boundary layer, with typical eddies highlighted in red circles, (a) at $Re_\theta = 753$ (b) at $Re_\theta = 21300$. The insert in (b) shows the whole boundary layer. Note the relative size of typical eddies relative to the boundary layer thickness. [40]

Large scale motions (LSMs), also called turbulent bulges, are another kind of compound coherent structure, which is an elongated region of streamwise velocity fluctuation with a streamwise extend of up to three boundary layer thickness [41]. Townsend [42] first speculated the existence of large scale flow structures in the turbulent boundary layer with an elongated region of length 1.4 boundary layer thickness from the time-delayed autocorrelation functions of instantaneous velocity u measurement. He also correctly inferred that a significant fraction of turbulent kinetic energy is carried by the large scale motions. Other correlation studies [43–46] confirmed and supported Townsend's observations of LSMs in the turbulent boundary layer. The spectral analysis performed by Bullock et al. [47] showed a high correlation of fluctuating streamwise velocity from the wall up to approximately one-third of the pipe radius following band filtering at 36, 72 and 108 Hz in time. This shows the existence of flow structures that are large in size and also last for a long time. Because of their relatively lower strength and larger size, LSMs were challenging to be separated from other coherent motions in the flow until the use of proper orthogonal decomposition (POD). POD separates large scales motions from the rest of the flow, with Liu et al. [48] reporting that the most energetic modes contain 50% of the turbulent kinetic energy, and that over 60% of the Reynolds stress resides in the outer flow. The generation and evolution mechanism of large scale motions are still a highly active research areas. Also there is evidence that the large scale motions can modify the motion of the other flow structure [41], as well as modify the amplitude of the small scale motion [49] near the wall.

2.3 Flow structure capturing techniques

One reason behind the increase in coherent structure studies is the advance in quantitative flow structure capturing techniques. A well-measured flow field can provide direct and unambiguous evidence for the existence of flow structures in a turbulent flow, as well as information of the generation and evolution of these flow structures. In this section, three generations of experimental flow structure capturing techniques will be reviewed, which are: (i) flow visualisation, (ii) hot-wire/hot-film anemometry, and (iii) particle image velocimetry. Meanwhile, computational fluid dynamics, especially direct numerical simulation (DNS), has significantly contributed to the identification and characterisation of turbulent flow structures and will be reviewed as well.

2.3.1 Flow visualisation

Flow visualisation is the simplest way to reveal flow structures in a fluid. Its history dates back to the 15th century when Leonardo da Vinci drew eddies visualised by air bubbles in the water stream and the experimentalists started to strategically introduce dye and seeding particles to the flow in mid-19th century. For example, Reynolds [50] observed and studied the vortex rings generated rain drops impacting on water surface by dying the water surface as early as 1875. As both water and air are transparent, the flow field can only be made visible by 1) light scatted or emitted by gas, liquid or solid particles seeding the flow; 2) behaviour of light substance attached to the solid body immersed in the flow; 3) change of refractive index of the flow [51].

The first method involves taking images of the seeding particles in the fluid, assuming that those particles faithfully follow the flow. Various particles have been used in seeding, including smoke, oil droplets, and water steam in air, and hydrogen bubbles, ink, milk and aluminium particles in water. A number of different techniques have been developed to record the fluid flow. If only a pulse of seeding particles is injected into the fluid, then a long exposure can be used to capture their trajectory, that allows the pathlines of the fluid flow to be visualised, which is mathematically represented as

$$\begin{cases} \dfrac{d\boldsymbol{x}_P}{dt}(t) = \boldsymbol{u}_P(\boldsymbol{x}_P(t), t) \\ \boldsymbol{x}_P(t_0) = \boldsymbol{x}_{P0} \end{cases}, \tag{2.17}$$

where $\vec{x}_P$ is the path of one particle as shown in the visualisation image, and $\vec{u}_P(x, t)$ is velocity of the particle along its path. Another method is to seed the flow continuously and use short exposure to record the images. In this method, all particles that pass through the seeding point are recorded simultaneously, which form streaklines in the visualisation images. Unlike pathlines, the position of the streakline not only depends on the velocity of the particle at the time of passing but also on all subsequent velocity changes. Thus, numerical methods of stepping in time are needed to calculate the streakslines computationally [52]. Streaklines coincide with pathlines and streamlines in a steady flow, however, in time-dependent flow like turbulence, they are not the same. In addition to those methods, a line of seeding devices can be deployed to generate a pulse of tracer particles, and by taking images sometime later, the lines on the image show the location of the particles that were adjacent at a given time, called timelines. Figure 2.12a shows an example of flow visualisation using pathlines, figure 2.12b shows an example of flow visualisation using streaklines and figure 2.9, the visualisation of Λ-vortices, shows an example of flow visualisation using timelines.

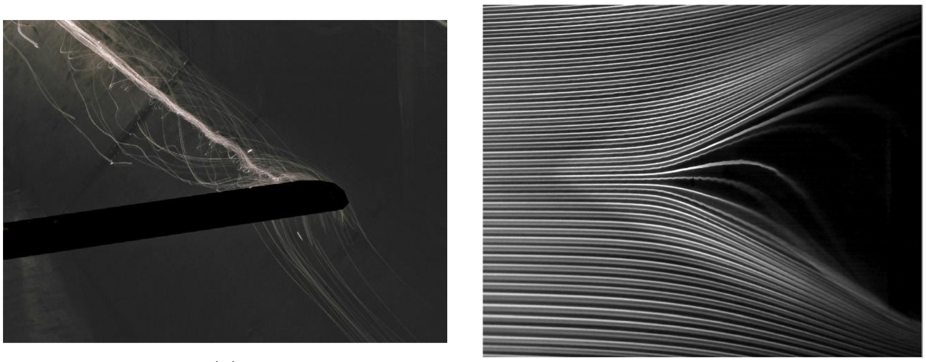

(a) (b)

Figure 2.12: (a) Wingtip vortices generated by NACA0012 airfoil under a freestream velocity of 10m/s visulised by pathlines using hydrogen bubbles [53]. (b) Flow over a rotating cone visualised by streaklines [54].

A primary drawback of flow visualisation using particles is that all pathlines, streaklines, and times lines are a function of both time and location of the tracing particle, and therefore, although flow visualisation suggests some insight into the fluid flow, it is not possible to perform quantitative flow measurement using this technique. Although regions of high vorticity concentration can be clearly shown using dye visualisation, dye fluid is less observable in areas with lower vorticity concentration, which makes these flow structures difficult to visualise. For example, flow visualisation loses effectiveness in recognising some wave structures near the wall, especially at the initial stage when the vorticity is less concentrated. Even though some flow structures are captured by flow visualisation, it is likely to be neglected in the analysis process due to the poor clarity of their existence. In addition, most of the flow visualisations are limited to a two-dimensional plane, which sometimes leads to misinterpretation of the structures present in the visualisation [24].

Nevertheless, despite of its drawback, flow visualisation by seeding the flow is still one of the most important tool to study the flow structures. This was especially the case before 1980s, when it was used to identify a range of flow structures including packets [40], Λ-vortices [55], solitonlike coherent structures [56], hairpin vortices [25], vortex packets [30], typical eddies [39], low speed streaks [10] and turbulent spots [57].

Two further methods of flow visualisation are also widely used in the investigations of fluid flow, but they are not particularly useful in the study of coherent structures. The second flow visualisation method is via paper, ropes, or strips of cloth with one end attached to the test object's surface and the other end free, called tufts. By observing the tufts' direction and movement, the researcher can tell if the flow is laminar, turbulent or reversed at the point of measurement. This method only provides a coarse view of the flow close to a measurement surface, thus it is mainly used in industrial application rather than in the turbulent flow research context where it is neither economical nor necessary to seed a large volume of fluid. An example of using tufts for flow visualisation is shown in figure 2.13.

The last method of flow visualisation is changing the refraction index of the flow and using the optical method, for example, shadowgraph, Schlieren or interferometry, to visualise and record the flow. The change of refractive index is directly associated with the fluid density via the Gladstone-Dale relation [58], so these methods are suitable to measure heated or supersonic flows where the flow density changes greatly. Coherent structures in heated and supersonic flow are out of the scope of this thesis, so they are only presented briefly here.

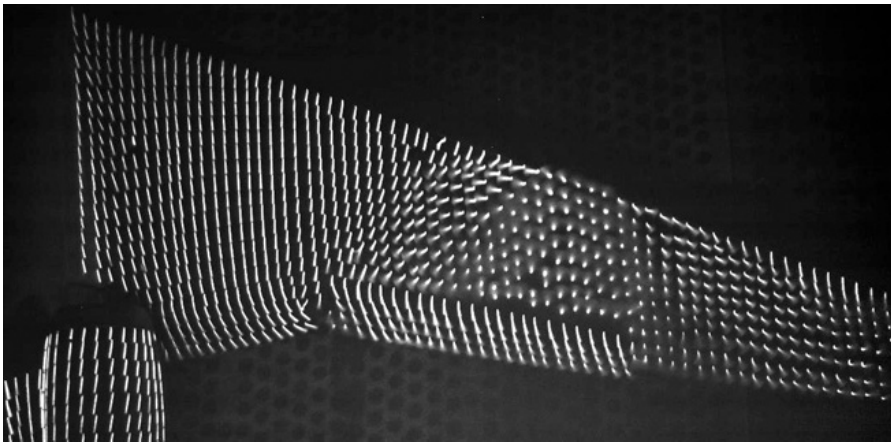

Figure 2.13: Using fluorescent mini-tufts to visualise the flow over a commercial aircraft model [59].

2.3.2 Hot-wire/Hot-film anemometry

Hot-wire/hot-film anemometry is a good supplement of flow visualisation in the study of coherent structures because of its ability to measure fluid velocity. Hot-wire or hot-film anemometers consist of a thin metal element that is heated by an electrical current and cooled by the surrounding flow, mainly by forced convection. Therefore, by sensing the temperature of the metal element by its resistance change, the mass flow rate, thus the velocity, of the flow can be calculated [60]. The application of hot-wire anemometry started as early as 1909 by Kennelly et al., [61]. However, because of the manufacture limitations and the lack of accurate resistance measurement technologies at that time, hot-wire anemometry could only measure mean velocity and hence didn't significantly contribute to the study of turbulence. It was not until the 1960s when a large number of studies were carried out due to a better understand the response of the sensors to changing flow environment, including the effect of thermal lag [62], large velocity fluctuations [63], the backbone material of hot-films [64], sensitivity change at different sensor temperatures [65], finite length of the wire [62] and wire thickness [66].

The wire in a hot-wire probe is usually 0.5 - 5 μm in diameter, 0.1 - 2 mm long and made of gold, tungsten, platinum or more rarely iridium because of their chemical stability. The wires are usually softly soldered to the supports and are typically heated up to 300 degrees in operation. The wires' ends are typically plated, so that the effective measurement length is precisely controlled. Hot-film sensors are typically 1 μm thick platinum deposited to a quartz back support, which are in the shape of a cylinder. An additional quartz coating is applied to the hot film to protect it from the electrochemical effects. Hot-films are usually used in environments that require more mechanical strength than hot wires. For example, in heavily seeded air or water flows. Hot films are typically only heated to 20 degrees to prevent water vapour bubbles from forming. Schematics of typical hot-wire and hot-file probes are shown in figure 2.14.

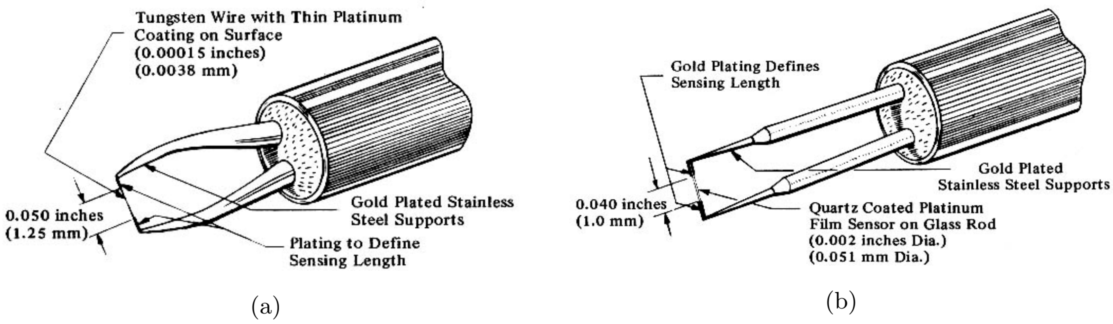

Figure 2.14: (a) The configuration of a typical hot-wire probe (b) The configuration of a typical hot-film probe.

Hot-wire and hot-film probes can be set-up with two different electrical circuits: (i) constant-current anemometers (CCA) and (ii) constant-temperature anemometers (CTA). In a CCA, a constant supply of current is supplied to the hot-wire, and a voltage drop over the hot-wire is used to calculate the resistance change. In a CTA, a Wheatstone bridge and feedback loop is used with the CTA being one of the arm of the Wheatstone bridge, with the voltage across the hot-wire is amplified, monitored and regulated to keep its temperature constant. The CTA is more common used nowadays as it can measure a larger range of velocity fluctuation without overheating the hot-wire [60]. The velocity measured by the hot-wire is highly affected by the direction of the flow. When the flow direction is not normal to the hot-wire, the sensor sees an effective velocity which is the real velocity projected to the direction normal to wire direction, and a large error is introduced. Thus, in order to measure all three components of the velocity vector at the sensor, three sensors are needed, which is called a tri-axial probe. An image of a triaxial probe is shown in figure 2.15c [67].

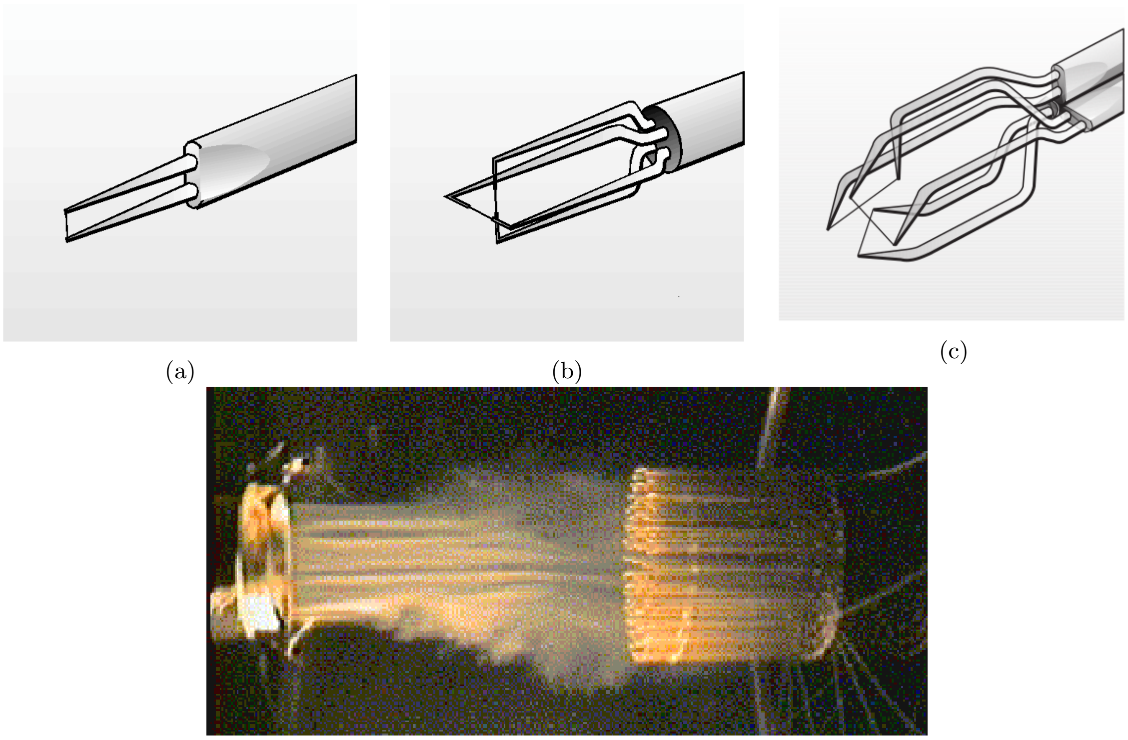

(a) (b) (c)

(d)

Figure 2.15: Different configurations of hot-wire anemometer (a) single hot-wire probe (b) X-probe (c) triaxial hot-wire probe [68] (d) hot-wire probe array consisting 138 single-wire hot-wire probes in the operation of measuring turbulent jet[69].

The spatial resolution achievable by hot-wire anemometry mainly depends on the length and diameter of the wire. When the hot-wire length is not negligible compared to the characteristic length of the flow in interest, the velocity fluctuation along the direction of the hot-wire will be smoothed out, and only the averaged value can be measured. On the other hand, if the length to diameter ratio of the hot-wire is not high enough, some heat will be transferred to the supporting prongs of the hot-wire probe and affect the measurement accuracy as well. Ligrani and Bradshaw [70] investigated the spatial resolution of the hot-wire and concluded that in order to provide an accurate measurement of a turbulent boundary layer flow, the length of the hot-wire has to be less than 20 times of the viscous length scale of the fluid, and the length-to-diameter ratio has to be larger than 200. The experiments performed by Ligrani and Bradshaw were limited to one wall-normal height at different flow speed, but the spatial decomposition of streamwise velocity u is not the same at different wall-normal positions. Therefore, Hutchins et al. [71] performed an additional study on the spatial filtering of hot-wire anemometry and arrived at a spatial filtering model which is a function of wire length, wall-normal distance, and the local frictional Reynolds number.

Because of its ability to measure flow precisely at one point, the hot-wire/hot-film anemometry is often used in conjunction with flow visualisation to study the coherent structures, where flow visualisation is used to identify the structure, and hot-wire/hot-film probes are placed at positions of interest to quantitatively study the size and evolution of flow structures. This hybrid method remained the primary experimental tool to study coherent motions until the late 1990s [72]. The major limitation of hot-wire/hot-film anemometry is that the measurement is only limited to one point in the flow. Although the hot-wire arrays have been used to increase the points of measurement in the field, as shown in figure 2.15d, the spatial information acquired is still very limited. Another limitation of the hot-wire/hot-film anemometry is being an intruding methodology, since the probes obstruct and disturb the flow.

An analogous point-wise, but non-intrusive, velocity measurement method is Laser Doppler anemometry (LDA). First introduced by Cummins et al. [73], LDA measures the Doppler shift of the light scattered by particles seeding the flow to determine the velocity at a measurement point. Because no probes need to be placed in the flow, this technique is non-intrusive thus does not disrupting the flow. However, the measured time-varying velocity is still at a single point and full-field measurement is not possible using this technique.

2.3.3 Particle image velocimetry

Particle image velocimetry (PIV) is a method to perform velocity field measurement by finding the displacement of tracer particles recorded on images. It is currently the primary experimental tool to capture coherent structures in the turbulent flow, and a range of flow structures have been captured by PIV [41, 74–77]. PIV develops from flow visualisation techniques, especially particle-streak photography [78] and Laser-speckle velocimetry[79, 80]. Base on those techniques, Adrian [81] in 1984 proposed that it is not necessary to seed the flow heavily so that a laser speckle pattern is observed; instead, it is possible to measure displacement from double-exposed images of individual particles using auto-correlation. Since then, a range of studies concerning different particle sizes, particle concentration, illumination configurations, recording media, and analysis techniques have been performed, which is thoroughly reviewed by Adrian [82] in 1991. He concluded that the preferred way to perform PIV analysis is: a) recording in multiple frames and with multiple pulses with the pulse duration δt short enough to freeze the particles, and pulse interval Δt appropriate for the velocity measured; b) using a thin laser sheet for illumination to achieve a depth-of-field which is smaller than the depth-of-focus of the lens; c) using small seeding particles, so the particle velocity lag relative to the flow is negligible as represented by a prediction with a Stokes number much smaller than 1; d) having a high enough particle concentration so that 5 - 10 particles are present in each interrogation window. The digital cross-correlation PIV analysis on single exposed images introduced by Willert and Gharib [83] removed photographic and opto-mechanical processing steps from PIV, therefore greatly simplified the analysis process and made the wide application of PIV on high-resolution high-framing rate recoding practicaly foreseeable. The multi-grid/multi-pass PIV introduced by Soria [84] increases the signal-to-noise ratio of the PIV analysis, thus significantly increased the measurement accuracy of PIV, especially when a high velocity gradient exists.

2.3.3.1 2-component 2-dimensional particle image velocimetry (2C-2D PIV)

Modern 2C-2D PIV methodology has significantly evolved since the 1990s due to the advancement of lasers, cameras, electronics and optics. The digital computing power and computing algorithm have advanced to a point which enables the cross-correlation analysis of 2C-2D PIV to be fully digital. The development of imaging sensors, especially CCD and sCMOS sensors, have reached a resolution of more than 40 million pixels [2] and a frame rate over 20 kHz [85] with superior performance to traditional films. In addition, the development of high energy Nd:YAG lasers has enabled the illumination of much larger fields of view to make the weak scattered light of micro-sized seed particles visible by the cameras. A typical experimental set-up and processing flow chart for 2C-2D PIV is shown in figure 2.16.

In a typical 2C-2D PIV experiment, the laser beam is shaped by spherical and cylindrical lenses into a sheet with thickness typically smaller than 500 μm and a width large enough to cover a large field of interest. The laser pulse duration needs to be small enough so that the displacement of the seeding particles within the pulse duration is less than 0.01 pixels, and the interval between a pair of laser pulses is selected based on the range of the fluid velocities present in the volume of measurement. The pulse energy ranges between 5mJ to 200mJ, depending on the size of the illuminated field of view, because of the relatively inefficient 90-degree scattering of the seeding particles. The seeding particles in the flow need to be large enough to ensure sufficient scattering, but small enough so that the particles faithfully follow the flow. The non-dimensionalised relaxation time for the particles is related to the Stokes number of the particle, as shown in equation 2.18.

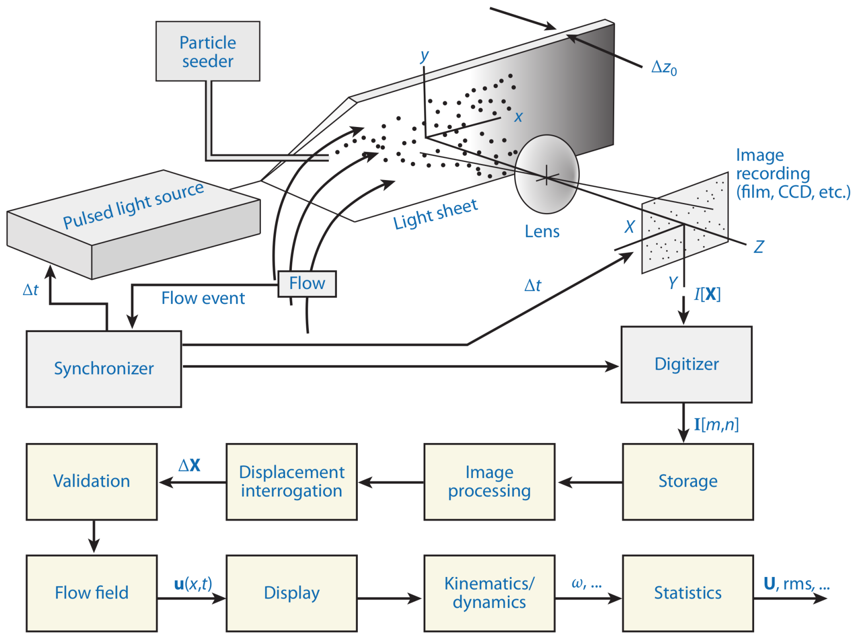

Figure 2.16: A typical experimental set up and analysis process[86].

$$\mathrm{Stk} = \frac{t_p}{t_f} = \frac{\rho_p d_p^2}{18\mu_f} \times \frac{u_f}{l_f}, \tag{2.18}$$

where t_p and t_f represent the characteristic time of the particle and the fluid respectively, whose expressions are the first and second term on the right-hand side of equation 2.18, with ρ_p representing the particle's density, d_p, the diameter of the particle, μ_f, the dynamic viscosity of the fluid, u_f, the characteristic velocity of the fluid flow, and l_f, the characteristic length of the fluid flow. A Stokes number $\ll 1$ represent a particles that follows the fluid with high fidelity. In air flow, particles with diameter of 1 μm, which are produced from smoke, fog, oil droplets or hydrogen bubbles, are typically used. In water, typical seeding particles are polystyrene or hollow glass microspheres of diameters $\approx 10\mu m$, and are sometimes coated with metal to increase reflectivity [87].

When analysing the recorded image pairs, each image is subdivided into small areas, called interrogation windows (IW). The IWs from an image pair are then digitally cross-correlated. Here only a brief description is provided, and a full detailed exposition of the digital cross-correlation PIV analysis is provided by Soria [88]. Typically, a Fourier-transformation based cross-correlation is used instead of direct cross-correlation to take advantage of the fast Fourier transform (FFT) routine. The equation to calculate the cross-correlation by FFT is shown as the equation 2.19.

$$f \star g = \mathcal{F}^{-1}(\mathcal{F}(f)^* \times \mathcal{F}(g)), \tag{2.19}$$

where $f \star g$ denotes the cross-correlation of f and g, $\mathcal{F}()$ denotes the Fourier transform, and * denotes the complex conjugate. The position of the peak relative to the centre of cross-correlation is the relative displacement between the two images. As the resultant velocity field is an average velocity of the fluid in the IW, the size of IW needs to be as small as possible to provide a high spatial resolution. However, the smallest size of the IW is limited by the maximum displacement of the particles in the IW, as the peak of cross-correlation will be wrapped in the opposite direction if the maximum displacement of the particles is more than half of the IW size. Also, as the displacement increases, the part of the image used to calculate the cross-correlation is smaller, so generally, the maximum displacement should not be larger than one-quarter of the IW size for an accurate estimation.

In order to increase the spatial resolution and the accuracy of PIV, different improvements have been developed. Although most of these techniques are developed for 2C-2D PIV, most are directly extended to a higher dimension and more components PIV analysis. One of the substantial improvements is the multi-grid/multi-pass algorithm[84]. Using this algorithm, the second interrogation window is shifted according to the displacement found in the first pass of PIV, so that the displacement between the first IW and shifted second IW is near zero. Thus it is possible to use a much smaller IW size for the second pass, as long as there are enough particles in the IWs, to achieve a much higher spatial resolution and a higher signal-to-noise ratio in the cross-correlation plane. Another commonly used technique to increase the measurement accuracy is finding cross-correlation peak to sub-pixel accuracy. A couple of approaches have been developed for this, including the centre-of-mass method, function-fitting method, and three-point estimator[87]. The centre-of-mass method finds the centroid of the peak by dividing the first-order moment and zeroth-order moment, but an appropriate threshold needs to be applied to data so that only the values near the correlation peak contribute to the centroid. It is also possible to fit the cross-correlation peak to a parabola or Gaussian peak, which is more robust than the centre-of-mass method. Finally, the three-point estimator is a simplified version of the function-fitting method, which only uses 5 points near the peak. It is computationally less demanding and especially appropriate to narrow cross-correlation peaks of size 3-5 pixels. Using those methods, the position of the cross-correlation peak can be estimated to an accuracy of 0.01 pixel[83]. The a filter applied on the cross-correlation function proposed by Hart[89] also significantly increased the signal-to-noise ratio of the cross-correlation by multiplying the cross-correlation with the result from adjacent IW thus amplifying the cross-correlation peak at the same position and suppressing the noise.

Despite using the above methods, erroneous vectors are still not completely eliminated in the PIV analysis due to the non-uniform illumination, tracer particle distribution

Validation Method	Equation
Maximum velocity check	$\lvert\boldsymbol{U}\rvert < \epsilon_{thresh} IW size$
Maximum cross-correlation peak check	$\max(CC) > \epsilon_{thresh}$
Global histogram check	$\lvert\boldsymbol{U} - \boldsymbol{U}_n\rvert < \epsilon_{thresh}$
Dynamic mean check	$\left\lvert\boldsymbol{U} - \overline{\boldsymbol{U}_n}\right\rvert < \epsilon_1 \overline{\boldsymbol{U}_n} + \epsilon_2 \sigma(\boldsymbol{U}_n)$
Dynamic median check	$\left\lvert\boldsymbol{U} - \mathrm{med}\left(\boldsymbol{U}_n\right)\right\rvert < \epsilon_1 \mathrm{med}\left(\boldsymbol{U}_n\right) + \epsilon_2 \sigma(\boldsymbol{U}_n)$

Table 2.1: The equations of some commonly used data validation criteria for PIV. $\boldsymbol{U}$ represents the velocity vector being validated, $\boldsymbol{U}_n$ represents the neighbouring velocity vectors, commonly 8 nearest vectors. ϵ_{thresh}, ϵ_1 and ϵ_2 are predefined threshold for validation, med is the median operator and σ is the standard operation operator.

and out-of-plane particle motions. Thus, post-processing data validation is essential to filter out the erroneous vectors. Some of the validation methods are based on the cross-correlation peak quality. As mentioned before, the PIV measurements are more accurate when the displacement is less than a quarter of the IW size because of the higher signal to noise ratio. Thus a maximum velocity check criterion is commonly used. Also, a high cross-correlation peak value indicates a highly correlated PIV image pair, so this yields another commonly used criterion. Other data validation techniques compare the velocity vector with the surrounding vectors. These methods are based on the following assumptions about the raw PIV data, a) the flow field is a smooth and continuous function and b) erroneous vectors only occur isolatedly, while its size and direction are considerably different from the vectors around it [90]. Global histogram check finds the absolute value of the difference between the vector being checked and the surrounding vectors, then compares this magnitude with a predefined threshold. The dynamic mean or median check compares the magnitude of the difference between the vector being checked with the mean/median value of surrounding vectors with a predefined threshold. The vector validation methods' equations are summarised in table 2.1.

PIV vector validation is still an active area of research, and there are many studies aiming to improve the vector validation methods described in table 2.1. For example, Westerweel and Scarano [91] proposed an normalised median check so that the vadilation criteria is more robust against different velocity fluctuation levels presented in the PIV velocity field. The proposed criteria is

$$\frac{\left\lvert\boldsymbol{U} - \mathrm{med}\left(\boldsymbol{U}_n\right)\right\rvert}{\boldsymbol{r}_n + a} < \epsilon_{thresh}, \tag{2.20}$$

where $\boldsymbol{r}_n = \mathrm{med}\left(\boldsymbol{U}_n - \mathrm{med}\left(\boldsymbol{U}_n\right)\right)$, and a is a small number, typically 0.1, to prevent dividing by zero. Another example is the statistical multivariate outlier detection (MVOD) technique proposed by Griffin et al. [92]. MVOD uses the joint PDF of two velocity components, and reject the velocity vectors based on the 'distance' between the individual vectors and the center of the distribution, which is more effective than single-variable based criterion when large velocity gradients exist in the PIV image.

Once the erroneous vectors are identified, they are replaced by an interpolated value from surrounding vectors. Often, an additional smoothing filter, for example, a moving median filter, is applied to the measured velocity field to remove the high-frequency noise from the PIV measurement.

2.3.3.2 3-component 2-dimensional particle image velocimetry (3C-2D PIV)

In the application of 2C-2D PIV, one of the major sources of error is particles moving out of the laser sheet. Since most of the flow structures we are interested in are three dimensional, more advanced techniques need be employed to measure this quantity instead of minimising and ignoring this motion in 2C-2D PIV. Thus, the stereoscopic PIV (SPIV) was invented to achieve 3C-2D flow measurement [93, 94]. An example of the basic set-up for SPIV is as shown in figure 2.17. In this set-up, two cameras are rotated relative to each other so that the angles between the normals of the two line of sight ($O' - O - O''$ in figure 2.17) and with the laser sheet is of an angle θ, which is also known as an off-axis angle. The uncertainty of the measured in-plane and out-of-plane velocities are a function of the off-axis angle, so an off-axis angle of 45° is often used so that the uncertainty is the same for all velocity components. Besides, the cameras need to further rotated so that the imaging plane, lens plane and object plane intercept at the same point. This requirement, known as Scheimpflug condition [95], must be fulfilled so that the entire field of view is in focus when imaging. The three-component velocity vector can be constructed from the 2C-2D velocities captured by the first and second camera, using

$$\begin{aligned} U &= \frac{U_1 \tan\theta_2 + U_2 \tan\theta_1}{\tan\theta_1 + \tan\theta_2} \\ V &= \frac{V_1 + V_2}{2} + \frac{W}{2}(\tan\phi_1 - \tan\phi_2) \\ W &= \frac{U_1 - U_2}{\tan\theta_1 + \tan\theta_2} \end{aligned} \tag{2.21}$$

where U_1 and V_1 are the velocity components in the x-direction and in-plane y-direction as defined in figure 2.17 measured by camera 1, θ_1 is the angle between the line of sight of camera 1 and y-z plane, ϕ_1 is the angle between the line of sight of camera 1 and x-z plane. U_2, V_2, θ_2, and ϕ_2 are the corresponding values for camera 2 [96]. Note that the values of $\tan\phi_1$ and $\tan\phi_2$ are typically small, so using them in the denominator for the calculation of V is avoided to increase accuracy.

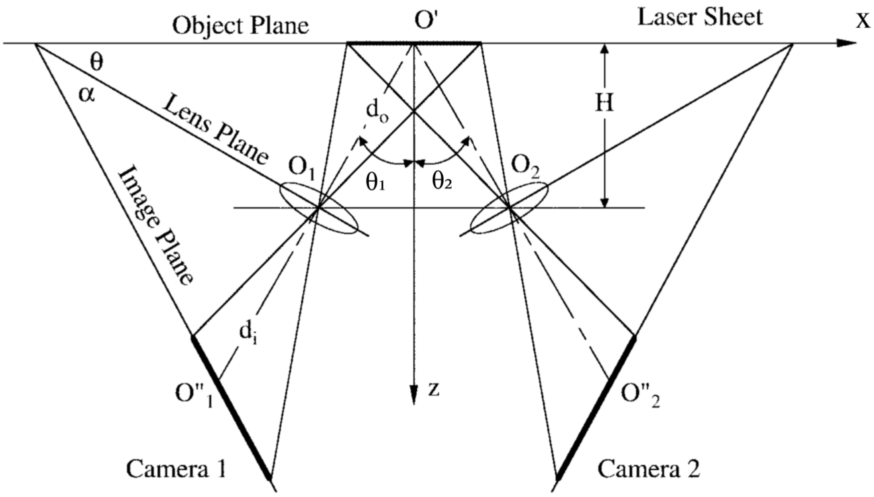

Figure 2.17: A typical experimental set up for SPIV [97].

One complication of the SPIV set-up is that the imaging magnification is not the same across the whole field of view, so that image dewarping is essential to correct the perspective error. Such a mapping function can be calculated analytically using a pinhole camera model, but it relies on the accurate measurements of the position and orientation of the cameras, which is not always easy or even possible. Instead, a more common practice is to use a calibration target consisting of markers at different z-planes to calculate the mapping functions, as well as the orientation of the cameras for 3D velocity vectors reconstruction.

2.3.3.3 3-component 3-dimensional particle image velocimetry (3C-3D PIV)

Although SPIV provides three-component velocity measurements in a 2D plane, in order to fully capture the velocity fields in a turbulent flow, it is necessary to expand the measurement into a volume, hence 3-component 3-dimensional (3C-3D) PIV is required. Over the past decades, a number of techniques have been developed that promised to yield 3C-3D velocity information of turbulent flow fields, however there is no consensus yet as to which is the best performing technique overall. A selection of most popular approaches to achieve 3C-3D PIV measurements is described below.

Tomographic particle image velocimetry (TPIV) uses multiple cameras to record tracer particle information from different angles with the three-dimensional particle intensity reconstructed from the recorded 2D images from each camera [98]. A typical experimental set-up includes a thick laser sheet illuminating a volume in the fluid, and typically 4-6 cameras viewing the flow from different directions, as shown in figure 2.18.

On each camera the Scheimpflug condition is satisfied, and a small aperture is used in the lens to create a large depth-of-focus so that all particles in the illumination volume are in focus.

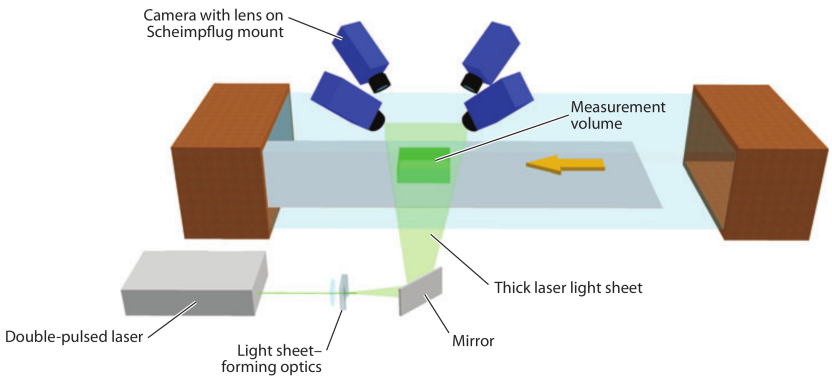

Figure 2.18: A typical experimental set up for tomographic-piv [72].

The reconstruction of a three-dimensional particle intensity map is then based on solving the line-of-sight equations,

$$P_i = \int_{s_i} I(x,y,z)\, ds_i \ , \tag{2.22}$$

where P_i is the intensity recorded by each pixel on each camera, $I(x,y,z)$ is the intensity map of the measurement volume, and s_i is the line-of-sight coordinate of each pixel. The multiplicative algebraic reconstruction technique (MART) used by Elsinga et al. [98] employs an iterative method to update each voxel value in the intensity map to map each captured pixel one-by-one, which can be computationally demanding. The Multiplied line-of-sight – Simultaneous algebraic reconstruction technique (MLOS-SMART) proposed by Atkinson and Soria [99] takes advantage of the fact that most of the voxels are of zero intensity as the particles only occupy a small portion of the measurement volume. This method considers all recoded pixels values in one iteration of voxel intensity calculation, thus, significantly reducing the computation requirement without compromising reconstruction accuracy. Lagrangian particle tracking has also been used to assist in reconstructing the 3-dimensional intensity map in the recently proposed shake-the-box method [100] which considerably reduces the presence of false-positive particles (also known as ghost particles) as well as the time required in the reconstruction.

One of the limiting factors of the TPIV is the noise introduced during reconstruction due to ghost particles, which impacts the spatial resolution and the maximum field of view in the depth direction. Furthermore, due to the usage of multiple cameras, a complex calibration process and large optical access to the flow are required for this method. These issues limit the application of TPIV to turbulent flows [101].

Other 3C-3D velocity field measurement techniques include synthetic aperture particle image velocimetry, which uses a mapping function between the particle location and image coordinates to refocus the image and reconstruct the tracer particles in a three-dimensional volume. This method can be applied using higher particle concentrations and a larger field of view in the depth direction than TPIV at the cost of using more cameras, typically 8 to 15, which in turn requires more complex calibration and additional optical access to the flow [102].

A more recent alternative uses a single plenoptic camera to record the light field image of the tracer particles [103]. Light field imaging coupled with 3D cross-correlation PIV analysis [84] is referred to as light-field PIV (LFPIV) [104–106]. LFPIV eliminates the need to use multiple cameras with a simple calibration process, which is one of the major sources of error of the multi-camera techniques. However, the performance of LFPIV is limited by the pixel-to-microlens ratio of the plenoptic camera and the measurable tracer particle concentration is smaller than that which can be used with the TPIV method.

The photogrammetry methods mentioned so far belong to the Incoherent Imaging family of 3C-3D Velocimetry methods because from a fundamental point of view, they do not require a coherent light source such as a laser, and other illumination sources such as diode illumination [107, 108] are sufficient to illuminate the fluid volume of interest containing the scattering tracer particles. The digital holographic PIV (DHPIV) technique differs from the above described methods in that it requires coherent light, and the diffraction patterns of the particles interfering with the reference wave are recorded instead of the images of tracer particles. In this thesis, a novel iterative 4D-DHPIV/PTV method is introduced in Chapter 3, which greatly increases the accuracy of the direct holographic PIV measurement.

2.3.4 Numerical methods

Due to the continuously accelerating development of computational resources and the development of massively parallel computational fluid dynamics (CFD) algorithms, the turbulent flows can now be simulated with a high enough accuracy and resolution to probe their detailed structure. Therefore, it has become a great supplement to experimental studies [21, 109, 110]. The primary numerical method to study coherent structures of turbulent flows is the direct numerical simulation (DNS), which numerically solves the Naiver-Stokes equations including all the length scales in the turbulent flow without modelling.

The advantage of using numerical methods to capture turbulent flow structures are that the velocity fields produced from DNS are three-dimensional and fully resolved in both time and space. Such measurements are currently impossible to acquire experimentally, and having both time and spatially resolved data is crucial in the study of the dynamics of turbulent flow structures. Furthermore, using DNS, the size and position of initial disturbances used to trigger turbulence are easily controllable. Thus it is possible to numerically study the link between some specific flow behaviours and causality. For example, Zhou et al. [29] studied how Q2 event generate hairpin vortices by numerically producing a Q2 event at a single point in a channel flow. Such a numerical experiment is not possible in real-life experimental flow set-ups.

Chapter 3

Four-dimensional Digital Holographic PIV/PTV (4D-DHPIV/PTV) †

Holography was first invented by Gabor [111] in 1948 and first applied to particle recording in 1967 [112]. But despite its long history, holographic techniques were not applied to particle image velocimetry in the early development stage, due to the complex film development and optical reconstruction process. However, thanks to the advancements in laser, camera sensor and computing technology, holograms can now be recorded by cameras with high spacial resolution and a large field of view, as well as be reconstructed and analysed digitally. Therefore, the DHPIV has become more widely used [108, 113–117]. A significant advantage of DHPIV is its very simple optical arrangement, especially for the in-line configuration. Since it only requires one camera, it is easier to set up and can be used where optical access is limited, such as for example in microscopic applications. However, its performance can be greatly affected by the noise in the reconstruction volume due to the twin image that is also present, as well as a large depth of focus and the small field of view in the depth direction as a consequence of comparatively weaker signal from the particles located further away from the imaging plane.

In this chapter, a 4D-DHPIV/PTV method is presented which aims to conquer these limitations. The methodology builds on the standard digital hologram reconstruction

† The content of this chapter has been published in Measurement Science and Technology, see Bihai Sun, Asif Ahmed, Callum Atkinson, and Julio Soria. A novel 4D digital holographic PIV/PTV (4D-DHPIV/PTV) methodology using iterative predictive inverse reconstruction. *Measurement Science and Technology*, 31(10):104002, 7 2020. doi: 10.1088/1361-6501/ab8ee8. URL https://doi.org/10.1088/1361-6501/ab8ee8

[116, 118] by incorporating advanced automatic digital filtering to reduce human interventions, 3-dimensional volume deconvolution to reduce the depth-of-focus problem and the virtual image effect, an efficient one-pass 3-dimensional clustering algorithm coupled with a novel inverse reconstruction approach accelerated by a particle prediction process to increase the particle reconstruction dynamic range and 3-dimensional reconstruction domain. The measurement uncertainty of this methodology is first quantified using simulated data under different conditions, then experimentally implemented to measure the flow of a micro-channel with the results compared against the theoretical velocity profile for a laminar micro-channel flow.

3.1 Theoretical background

Similar to other electromagnetic waves, optical wave fields have a complex distribution, which means they are characterised by both the amplitude and phase information. Generally, in photography when an optical field is recorded with a recording material such as a CCD/CMOS sensor or photographic film, only the intensity (amplitude squared) of the wave is recorded, and the phase information is lost during the recording process. Unlike photography, in holography two waves, an object wave and a reference wave, with the same frequency interfere and the intensity of the interference pattern containing both amplitude and the phase information is recorded. The recorded interference pattern, known as a hologram, can then be illuminated by the reference wave to reconstruct the object wave with its complex distribution, i.e. both the object wave amplitude and phase information are reconstructed.

In the process of recording holograms using an in-line configuration, a monochromatic, coherent, polarised single-mode and collimated light is used to illuminate the tracer particles in the flow. A part of the illuminating light is scattered by the particles and creates the object wave, whereas the un-scattered light is the reference wave. These two waves with the same frequency interfere to generate the hologram as shown in figure 3.1.

3.1.1 Diffraction calculation by angular spectrum

In order to derive the equation for light propagation, consider a wavefront U at $z = 0$ propagated to $z = z_0$. The Fourier transform of U can be expressed as

$$A\left(f_x, f_y, 0\right) = \iint_{-\infty}^{\infty} U(x, y, 0) \exp\left(-j2\pi\left(f_x x + f_y y\right)\right) dx\, dy, \tag{3.1}$$

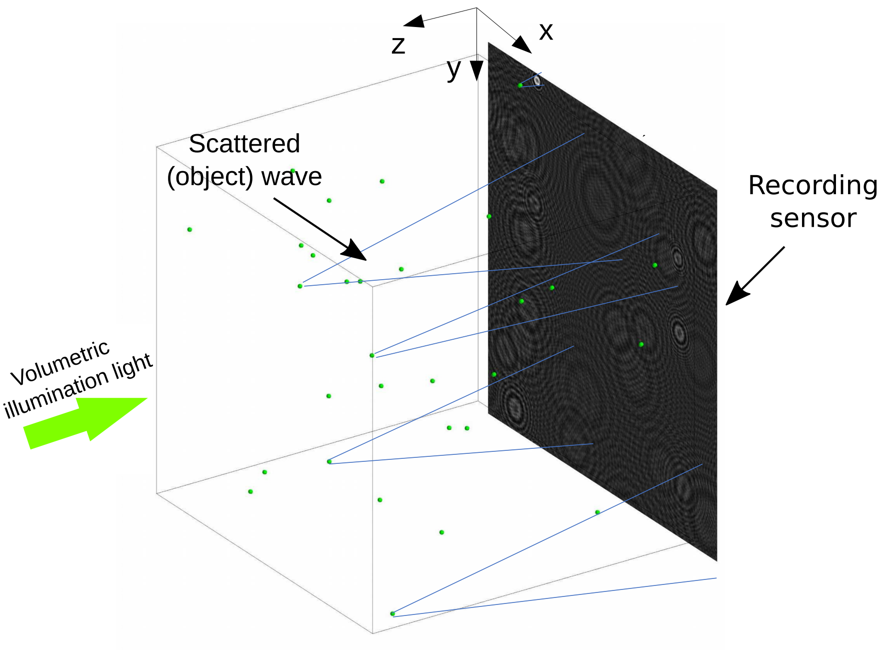

Figure 3.1: The in-line hologram recording process

where j is the imaginary unit, f_x and f_y are the wave-numbers in x and y direction and $A\left(f_x, f_y, 0\right)$ is the Fourier transform of $U\left(x, y, 0\right)$, also called the angular spectrum of $U\left(x, y, 0\right)$. Thus, the wave front at $z = 0$ and $z = z_0$ can be expressed as the inverse Fourier transform of the corresponding angular spectrum

$$U\left(x, y, 0\right) = \iint_{-\infty}^{\infty} A\left(f_x, f_y, 0\right) \exp\Big(j2\pi\left(f_x x + f_y y\right)\Big)\, df_x\, df_y \tag{3.2}$$

$$U\left(x, y, z_0\right) = \iint_{-\infty}^{\infty} A\left(f_x, f_y, z_0\right) \exp\Big(j2\pi\left(f_x x + f_y y\right)\Big)\, df_x\, df_y \tag{3.3}$$

The propagation of waves are governed by the Helmholtz equation, which states that at any source free position, the wavefront must satisfy

$$\nabla^2 U + k^2 U = 0 \tag{3.4}$$

where k is the wave number. Substituting equation 3.3 into equation 3.4,

$$(\nabla^2 + k^2) \iint_{-\infty}^{\infty} A\left(f_x, f_y, z_0\right) \exp\Big(j2\pi\left(f_x x + f_y y\right)\Big)\, df_x\, df_y = 0 \tag{3.5}$$

Because $(\nabla^2 + k^2) \exp\Big(j2\pi\left(f_x x + f_y y\right)\Big)$ is not zero except at origin, equation 3.5 implies

$$\nabla^2 A\left(f_x, f_y, z_0\right) + k^2 A\left(f_x, f_y, z_0\right) = 0 \tag{3.6}$$

As the propagation is only in the z-direction, the Laplacian term becomes $\frac{\partial^2 A}{\partial z^2}$ and the wavenumber in z direction can be written in terms of f_x and f_y,

$$k_z = 2\pi f_z = 2\pi\sqrt{\frac{1}{\lambda^2} - f_x^2 - f_y^2} = \frac{2\pi}{\lambda}\sqrt{1 - \lambda^2 f_x^2 - \lambda^2 f_y^2} \tag{3.7}$$

Thus, equation 3.6 can be written as

$$\frac{\partial^2}{\partial z^2} A\left(f_x, f_y, z_0\right) + \left(\frac{2\pi}{\lambda}\right)^2 \left(1 - \lambda^2 f_x^2 - \lambda^2 f_y^2\right) A\left(f_x, f_y, z_0\right) = 0 \tag{3.8}$$

Equation 3.8 is a partial differential equation of the angular spectrum A. Given the initial condition of A at $z = 0$, the angular spectrum at $z = z_0$ can be solved from the equation 3.8, to be

$$A\left(f_x, f_y, z_0\right) = A\left(f_x, f_y, 0\right) \exp\left(\frac{j2\pi z}{\lambda}\sqrt{1 - \lambda^2 f_x^2 - \lambda^2 f_y^2}\right) \tag{3.9}$$

Thus, converting back to spatial domain using inverse Fourier transform, the propagated wavefront $U(x, y, z)$ can be expressed as

$$U(x, y, z) = \mathcal{F}^{-1}\left(\mathcal{F}\left(U(x, y, 0)\right) \exp\left(\frac{j2\pi z}{\lambda}\sqrt{1 - \lambda^2 f_x^2 - \lambda^2 f_y^2}\right)\right) \tag{3.10}$$

The result shows that within the circle $f_x^2 + f_y^2 = 1/\lambda^2$ the light propagation kernel, $\exp\left(\frac{j2\pi z}{\lambda}\sqrt{1 - \lambda^2 f_x^2 - \lambda^2 f_y^2}\right)$, has an amplitude of 1 and varied phase, which suggest under this regime, the propagated wavefront is transformed to planar waves travelling towards different directions by the Fourier transform, the phase of each plane wave evolves according to the distance propagated, and then those propagated plane waves are transformed back to form a new wavefront. However if the condition $f_x^2 + f_y^2 = 1/\lambda^2$ is not satisfied, the light propagation kernel becomes an amplitude attenuation with exponential decay. The energy of the incident light will quickly drop to zero. This kind of wave is called evanescent wave, and it is only visible in the experiment if the light is propagated to a very small distance, and also the sensor is very sensitive to light to record the quickly diminishing wave front, which is generally not satisfied. Thus, in the following discussion, the f_x and f_y frequencies are assumed to satisfy $f_x^2 + f_y^2 = 1/\lambda^2$, and the evanescent wave case is ignored.

The angular spectrum method can be easily implemented by the numerical method using fast Fourier transform algorithms, and has minimal approximations in all scalar diffraction theories. However, the analytical solution of diffraction patterns using angular spectrum method is very difficult to get, thus some other diffraction models are introduced in Appendix A.

3.1.2 Models for scattered light by particles

3.1.2.1 Lorenz–Mie scattering model

For most experimental conditions for the 4D-DHPIV/PTV measurements, the sizes of seeding particles are of the same order of the wavelength. Thus, Lorenz–Mie scattering solution[119, 120] is applicable to the light scattered by those seeding particles. The Lorenz-Mie scattering model states that the scattered light from a homogeneous sphere illuminated by an electromagnetic wave has the following form

$$\mathbf{U}_s(k\mathbf{r}) = \sum_{n=1}^{\infty} \frac{j^n(2n+1)}{n(n+1)} \left(j\alpha_n \mathbf{N}_{e1n}^{(3)}(k\mathbf{r}) - \beta_n \mathbf{M}_{o1n}^{(3)}(k\mathbf{r}) \right), \tag{3.11}$$

where k represents the wavenumber and $\mathbf{r}$ represents the distance vector from scattering point to observing point. Equation 3.11 is an infinite sum of vector spherical harmonics $\mathbf{N}_{e1n}^{(3)}(k\mathbf{r})$ and $\mathbf{M}_{o1n}^{(3)}(k\mathbf{r})$ weighted by α_n and β_n. The weighting parameters depend on the refractive index of medium and particle, as well as the size of the particle, and can be calculated by

$$\begin{aligned} a_n &= \frac{m\psi_n(mx)\psi_n'(x) - \psi_n(x)\psi_n'(mx)}{m\psi_n(mx)\xi_n'(x) - \xi_n(x)\psi_n'(mx)}, \\ b_n &= \frac{\psi_n(mx)\psi_n'(x) - m\psi_n(x)\psi_n'(mx)}{\psi_n(mx)\xi_n'(x) - m\xi_n(x)\psi_n'(mx)}. \end{aligned} \tag{3.12}$$

In this equation $m = n_p/n_m$ represents the relative refractive index, k represents wavenumber of the incident wave and $x = k \times r$ represents the size parameter. In addition, $\psi_n(\rho) = \rho j_n(\rho)$, where $j_n()$ represents the spherical Bessel functions of the first kind, and $\xi_n(\rho) = \rho h_n^{(1)}(\rho)$, where $h_n^{(1)}()$ represents the Hankel functions of the first kind. Finally, the $\psi_n'(x)$ and ξ_n' functions are the derivatives of $\psi_n(\rho)$ and ξ_n respectively.

Once the complex scattering light of the particle is found, the reference wave, which is modelled as a plane wave with phase zero at particle position, is added to the scattered wave (object wave), and the hologram can be calculated by taking the squared amplitude of the compound wave.

The Lorenz-Mie theory is numerically implemented using an efficient recursive algorithm [121] and the number of terms included are determined from the criteria introduced by Bohren and Huffman [122]. However, a major drawback of simulating hologram using Lorenz–Mie scattering theory is the long computational time it requires. A typical calculation time is of the order one second for the simulation of a 512 × 512 hologram containing one particle, thus the total calculation time for bigger holograms containing more particles would be not foreseeable in analysis. In addition, once there are more than one particles in the measurement volume, the illumination light of some particles will not have a planar wavefront, so the Lorenz–Mie scattering theory will not be applicable.

3.1.2.2 2D Gaussian particle model

In order to reduce the calculational requirement for simulating holograms with many particles, the scattering from a particle can be approximated by a single Gaussian function. Thus, the particles are approximated by a two-dimensional Gaussian function blocking the incoming light, with the transmission function as following

$$T = 1 - \frac{1}{r\sqrt{2\pi}} \exp\left(-\frac{1}{2}\left(\frac{\sqrt{(x-x_0)^2+(y-y_0)^2}}{r}\right)^2\right) \tag{3.13}$$

In order to simulate a hologram using this particle model, the following process is used. First, without the loss of generality, the phase of the illumination light is assumed to be to zero at the position of the first particle. Second, the illumination light is multiplied with the transmission function of the first particle. Then, the transmitted light is propagated to the z position of the next particle, where the transmission function of the second particle is multiplied with the transmitted light. The process is iterated until the last particle, then the incident wave is propagated to the imaging sensor. This process is also illustrated in figure 3.2.

Under this model, the reference wave for each particle is different as a result of the hologram produced by particles further away from the imaging sensor, and the reference wave and object wave are not strictly separated but combined as one propagating wave, which is a better model of the light propagation process in reality. Figure 3.3 shows the comparison between the hologram produced by a single particle of size 2 μm located at 500 μm away from the sensor illuminated by 532 nm light, using Mie scattering and 2D Gaussian particle model. For Mie scattering calculation, the refractive index of the particle is 1.59, and the refractive index of the medium is 1.33, corresponding to polystyrene and water, respectively.

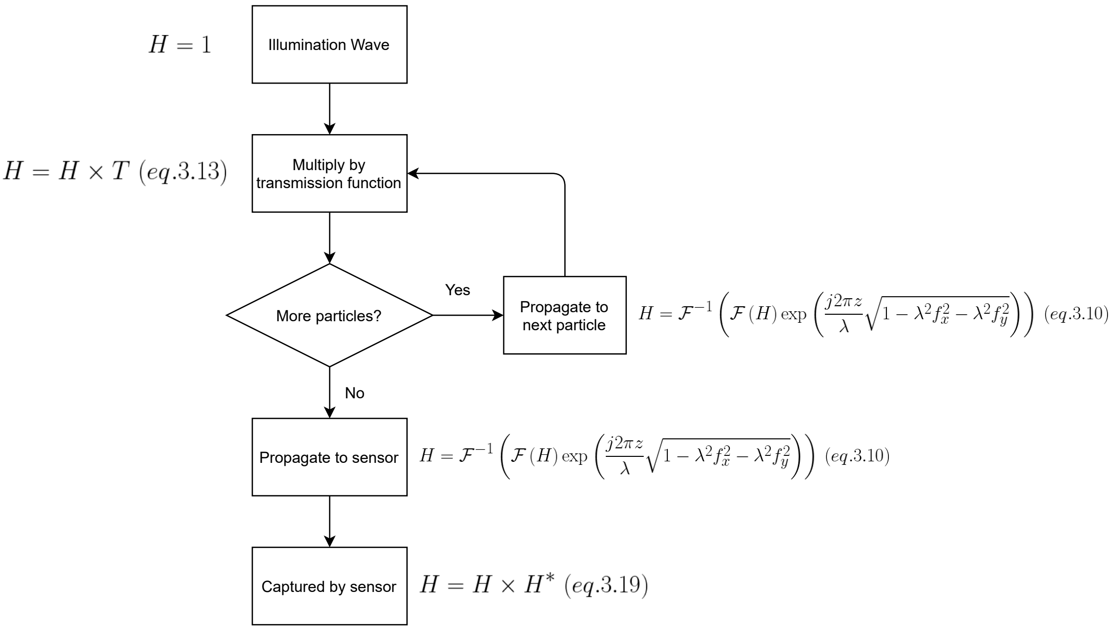

Figure 3.2: Process chart for simulating the hologram

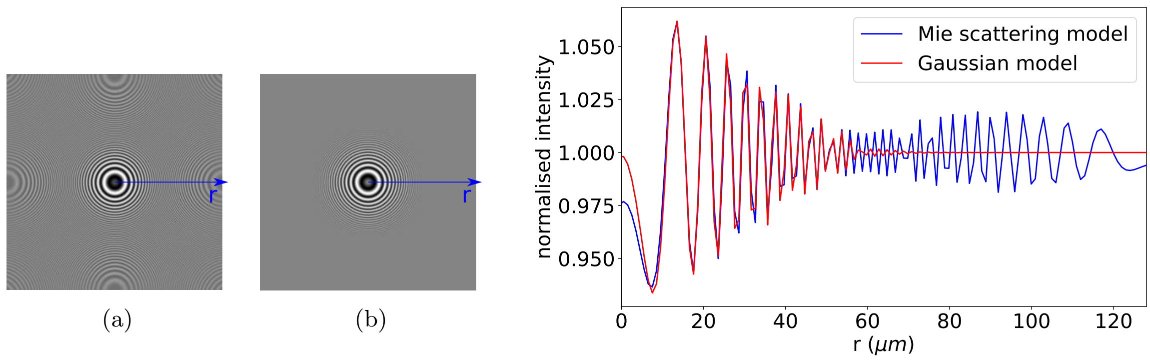

(a) (b)

(c)

Figure 3.3: Hologram simulated by (a) Mie scattering model (b) 2D Gaussian particle model. The particle being imaged is of radius 1 μm, located 500 μm away from the sensor, and illuminated by 532 nm light. The dimensions of the simulated holograms are $1024 \times 1024 \mu m$. For Mie scattering calculation, the refractive index of the particle is 1.59, and the refractive index of the medium is 1.33, corresponding to polystyrene and water, respectively. (c) The radial intensity profile of the hologram calculated by Mie scattering model and 2D Gaussian particle model.

.

As shown in figure 3.3a and figure 3.3b, the hologram simulation based on a Gaussian particle and based on Lorenz-Mie theory yields similar result. However, there are some artefacts at the edge of the hologram created based on Mie scattering. These artefacts are caused by the under-sampling of the numerical simulation, as the wavelength of the amplitude oscillation is smaller than the pixel size.

From the figure 3.3c, the radial profiles of hologram pattern predicted by the two models agrees except for the center of the particle, ignoring the artefacts in the hologram created by Mie scattering. Because the refractive index of the medium and the particle are not considered in the 2D Gaussian particle model, the particle radius stated in the model may not be the actual radius of the particles. For 4D-DHPIV/PTV application, the absolute size of the particles are not a concern, instead, the hologram produced from the 2D Gaussian particle model should be fitted to real hologram to find out the relationship between the radius used in the model and the real radius of the particle.

To calculate the holograms shown in figure 3.3 which are of size 256 × 356 pixels, the time it took to simulate the hologram using Mie scattering method is about 1,000 time longer than using 2D Gaussian particle model. Thus, the 2D Gaussian particle model was preferred for our application than the Lorenz–Mie scattering model.

3.1.2.3 2D Gaussian particle model with phase change

When the refractive index of the particle is similar to that of the medium, it is no longer appropriate to simulate the particle as a blockage of the light. Instead, the light going through the particle is of importance. Because of the difference in refractive index, the light going through the particle has a longer optical path than the surrounding reference wave, a phase change occur at the particle position [123]. Because the size of the particle is normally less than 3 pixels in the hologram, we can assume that the phase change is constant across the particle, thus the transmission function of a 2D Gaussian particle model with phase change is as below:

$$T = 1 - \frac{1}{r\sqrt{2\pi}} \exp\left(-\frac{1}{2}\left(\frac{\sqrt{(x-x_0)^2+(y-y_0)^2}}{r}\right)^2 + j\theta\right) \tag{3.14}$$

The phase induced is the same for all the particles given the same imaging condition, thus to replicate an experimental hologram by simulation, a hologram of one particle can be taken before the experiment, and the phase change can be found by fitting the simulated hologram with the experimental hologram, and the apparent radius for the model can be found by fitting as well.

Figure 3.4 compares the hologram generated using 2D Gaussian particle model and 2D Gaussian particle model with phase change with an experimental captured hologram using polystyrene particles (refractive index = 1.59) suspended in water (refractive index = 1.33).

As shown in the figure 3.4d, there is a pair of bright and dark regions in front of and behind the particle in the reconstruction volume from experimental hologram, and by

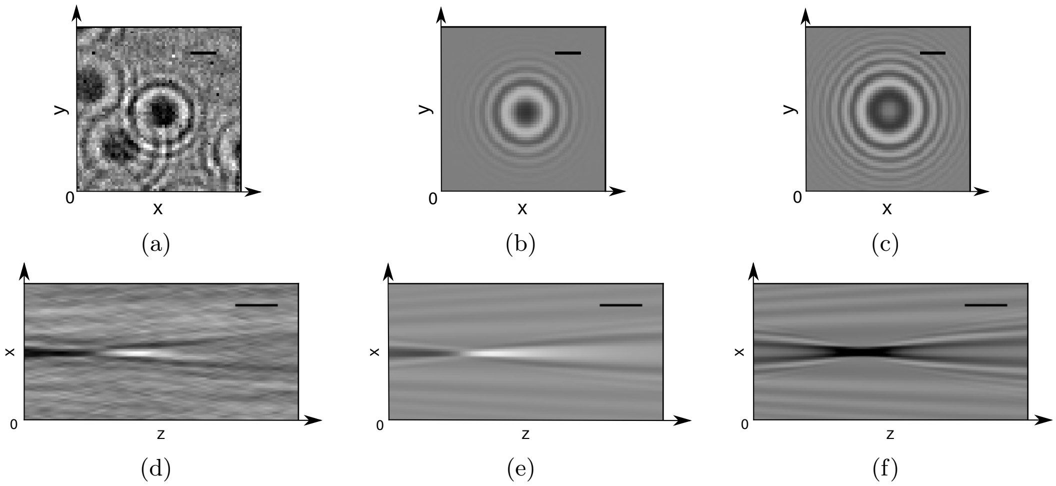

Figure 3.4: (a) A sample hologram taken in the experiment (b) fitted hologram with phase change using equation 3.14 (c) fitted hologram without phase change using equation equation 3.13 (d - f) the x-z slice of the reconstruction volumes from (a - c) at the particle. Scale bars in (a - c) are 7μm and in (d - f) are 14μm.

adding the phase change term at the particle, this phenomenon can be captured by the model, as shown in the figure 3.4e. The model without phase change will not produce the correct scattering profile in the z-direction nor a correct hologram, so the patterns created from the particle are correctly modelled without accounting for the phase change.

3.1.3 Illumination using tilted and expanding beams

In the experiment, it is almost impossible to obtain a completely planar illumination wave normal to imaging plane. Thus, the effect of tilted and expanding reference wave on the recorded hologram is investigated here.

3.1.3.1 Tilted illumination

The imaging set-up with tilted illumination is shown in figure 3.5. From the figure, the input to the hologram simulation process is a wave with linearly changing phase angle, expressed as

$$U_{illumination} = \exp\left(j\left(\frac{2\pi x\sin(\theta_{t_x})}{\lambda} + \frac{2\pi y\sin(\theta_{t_y})}{\lambda}\right)\right) \tag{3.15}$$

where θ_{t_x} is the tilting angle in the x direction, and θ_{t_y} is the tilting angle in the y direction.

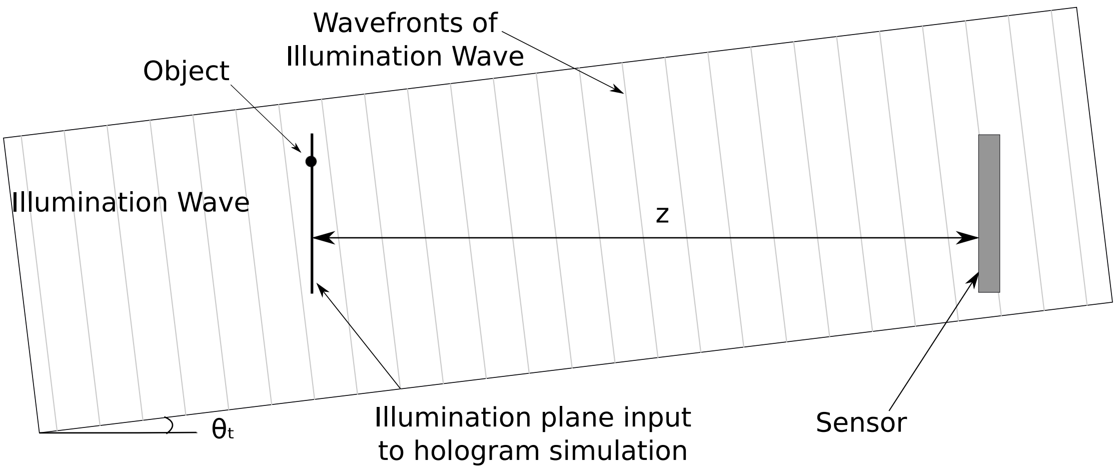

Figure 3.5: Optical setup of recording hologram with tiling beam. θ_t represents the tilting angle. Tilting in only one direction is shown in the figure, but the same applies to tilting in the other direction.

As the illumination beam is tilted, the object wave is tilted to the same angle, thus the hologram generated will be shifted from the particle position by $\tan(\theta_t) \times z$. However, because when taking the hologram, the phase information of the object wave is lost, so the reconstruction is normal to the image plane, and the shift of reconstructed particle will be the same position as the hologram. The shift caused by a tilted illumination plane is presented in figure 3.6.

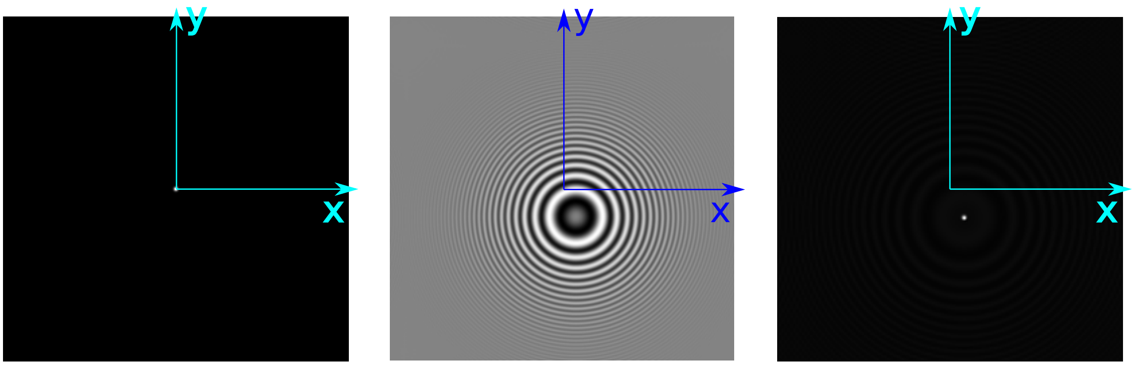

(a) (b) (c)

Figure 3.6: Simulated hologram and reconstruction using a reference wave tilted 2.38°in horizontal direction and 1.19°in vertical direction. The particle being imaged is of radius 1 μm, located 500 μm away from the sensor, and illuminated by 532 nm light. (a) The image of the particle at the center of the sensor. (b) Simulated hologram using tilted beam. The center of hologram pattern is 21.0 μm towards right and 10.5 μm downwards relative to center. (c) reconstructed particle from (b). The position of reconstructed particle is 21.0 μm towards right and 10.5 μm downwards relative to center.

3.1.3.2 Expanding/converging illumination

To exam the effect of expanding or converging reference waves, we can assume that the illuminating wave is coming from a point source of z_r away from the imaging plane, as shown in the figure 3.7. The complex light field for illumination can be expressed as

$$U_{illumination} = \exp\left(j\left(\frac{2\pi}{\lambda}\sqrt{x^2+y^2+z_r^2}\right)\right) \tag{3.16}$$

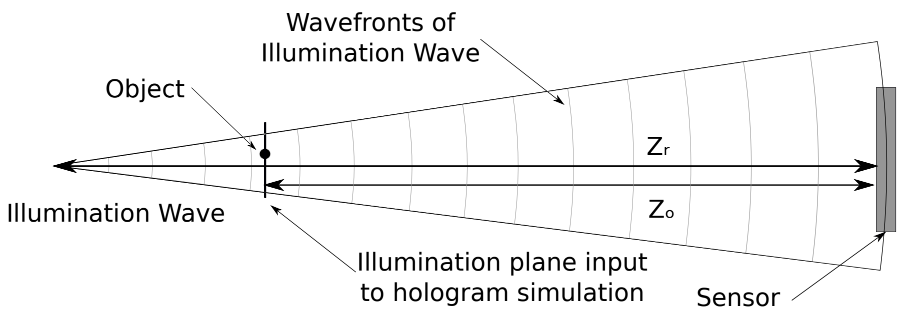

Figure 3.7: Optical setup of recording hologram with expanding beam. The converging beam has a negative z_r value.

Following the analysis given by Goodman [124], a hologram recorded by illumination from point-source will lead to a magnification in both transverse directions and axial direction, which can be calculated as:

$$\begin{aligned} M_{transverse} &= \left(1-\frac{z_o}{z_r}\right)^{-1} \\ M_{axial} &= M_{transverse}^2 \end{aligned} \tag{3.17}$$

Because of the axial magnification, the position of the reconstructed plane will change as well, so the reconstructed distance $z_{reconstructed}$ for a object at z_o will be

$$z_{reconstruct} = \left(\frac{1}{z_o}+\frac{1}{z_r}\right)^{-1} \tag{3.18}$$

3.1.4 Recording of the hologram

The hologram captured by the sensor can be written as

$$\begin{aligned} H &= (O+R)(O+R)^* \\ &= OO^* + OR^* + RO^* + RR^*, \end{aligned} \tag{3.19}$$

where H is the recorded hologram, O is the object wave and R is the reference wave. In the above equation, OO^* is the squared magnitude of the object wave, OR^* is the real image, RO^* is the virtual image, and RR^* is the squared magnitude of the reference wave. Because the magnitude of the object wave is much smaller than the magnitude of the reference wave, $OO^* \ll RR^*$ and the OO^* term can be neglected from the equation 3.19

In the experiment, the reference wave is often not perfectly planar, and the pattern in the reference wave will propagate as the hologram being reconstructed, introducing additional noise in the reconstruction. Thus, to extract the object wave from the hologram, the hologram is normalised by the squared magnitude of reference wave before reconstruction, as below:

$$\begin{aligned} \frac{H}{RR^*} &= \frac{OR^*}{RR^*} + \frac{RO^*}{RR^*} + \frac{RR^*}{RR^*} \\ &= \frac{O}{R} + \frac{O^*}{R^*} + 1 \\ &= \mathrm{Re}\left(\frac{O}{R}\right) + 1 \end{aligned} \tag{3.20}$$

3.1.5 Aliasing in digital hologram

The smallest resolvable scale of the reconstruction is determined by the size of the hologram after magnification. Considering an object at a distance of z from the hologram imaging plane, imaged by a sensor of size L_x, as shown in figure 3.8, the numerical aperture of this imaging system can be given as

$$NA = \sin\theta_{imaging} \approx \frac{L_x}{2z} \tag{3.21}$$

Here the small angle approximation for $\theta_{imaging}$ is used. From the Abbe diffraction limit, the minimum resolvable length of the system is,

$$\Delta x = \frac{\lambda}{2NA} = \frac{\lambda z}{L_x} \tag{3.22}$$

If a hologram is simulated without large enough sensor size, aliasing will occur, and the whole diffraction pattern will not be contained in the hologram. Figure 3.9 compares a holograms which are efficient large in size and an aliased hologram.

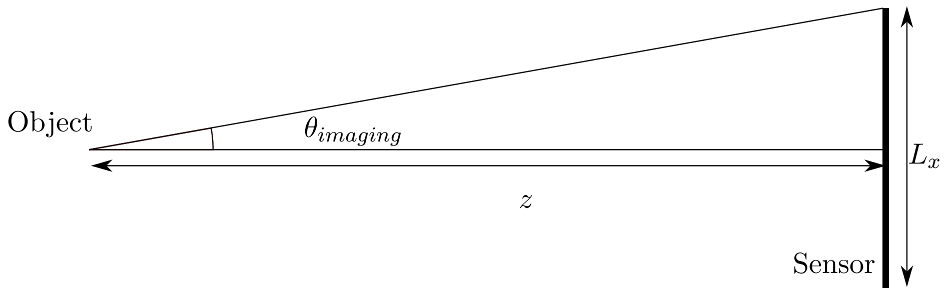

Figure 3.8: Hologram recording process of a finite imaging sensor.

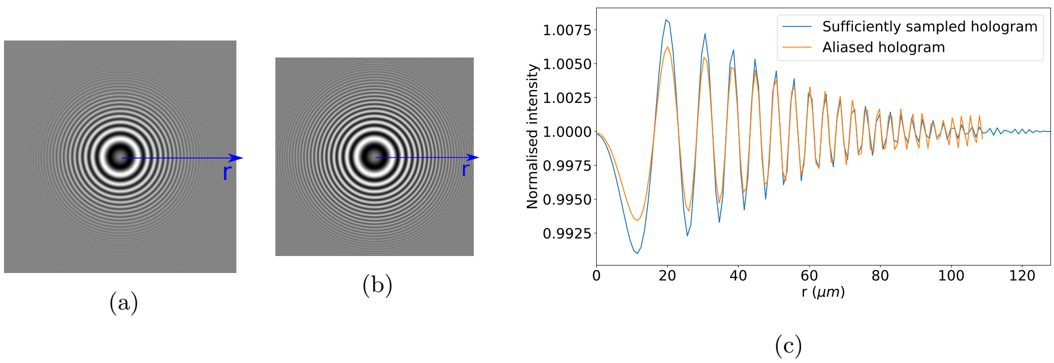

Figure 3.9: (a) A hologram just big enough to avoid aliasing. (b) The hologram with the same imaging condition as (a), but 27% smaller, which is aliasing. (c) The radial intensity profile of the holograms, blue: Hologram (a) orange: Hologram (b).

3.1.6 Propagation through the medium of different refractive index

The discussion above all apply to the light propagation though uniform medium, however, in experiment, the laser often passes through layers of different medium, for example, water tunnel with glass walls. To account for the different refractive index, the wavelength used in the propagation equation needs to be adjusted by,

$$\lambda_{eff} = \frac{\lambda}{n} \tag{3.23}$$

where n is the refractive index of the material. This effective wavelength will pose a scaling factor to the reconstruction distance, so that

$$z_{real} = n \; z_{reconstract} \tag{3.24}$$

3.1.7 Off-axis Hologram

In all the discussion above, the reference wave and the object wave is in the same direction, therefore this configuration is called an in-line configuration. In contrast, if an angle exists between the propagation directions of the reference and object wave, it is an off-axis configuration. The advantage of using an off-axis configuration is that the virtual and the real images in the reconstruction volume would be offset, making it easier to separate the two. A typical optical set-up to record off-axis holograms is shown in Figure 3.10. In the set-up the objective and reference wave a separated by a beam splitter from the laser, and when recombining the two there is an off-axis angle θ exists. The off-axis angle can have a in-plane component (y direction of the recorded hologram) as well as a out-of-plane component (x-direction of the recorded hologram).

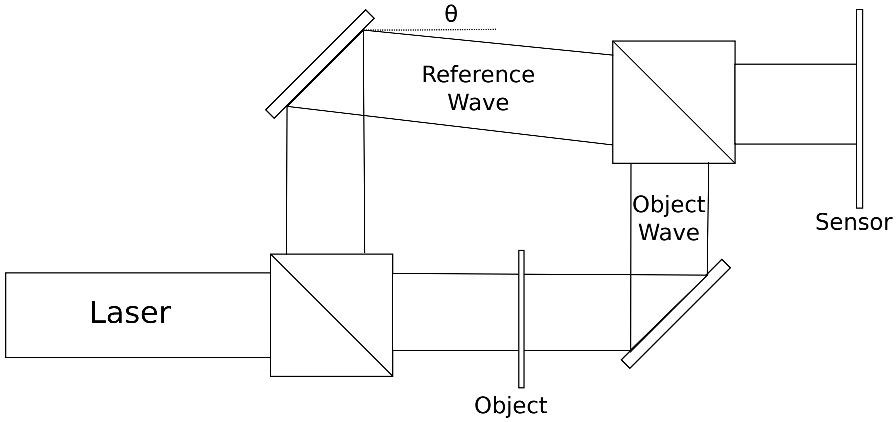

Figure 3.10: Typical experimental set-up of off-axis hologram recording.

The off-axis hologram can be expressed as,

$$H = \underbrace{OO^* + RR^*}_{\text{order 0}} + \underbrace{OR^* e^{jk\sin\boldsymbol{\theta r}}}_{\substack{\text{order +1}\\ \text{Real Image}}} + \underbrace{RO^* e^{-jk\sin\boldsymbol{\theta r}}}_{\substack{\text{order -1}\\ \text{Imaginary Image}}}. \tag{3.25}$$

To reconstruct off-axis holograms, the order +1 peak is shifted to the center of the Fourier plane, which corresponds to multiplying the hologram with a phase shift term $e^{-jk\sin\boldsymbol{\theta r}}$. Therefore, the shifted hologram is,

$$He^{-jk\sin\boldsymbol{\theta r}} = OO^* e^{jk\sin\boldsymbol{\theta r}} + RR^* e^{jk\sin\boldsymbol{\theta r}} + OR^* + RO^* e^{-2jk\sin\boldsymbol{\theta r}}. \tag{3.26}$$

To separate the real image from the other terms, a low-pass filter is applied to the shifted hologram. In this process, the assumption of the hologram satisfying Whittaker-Shannon sampling theorem is made. Under this assumption, the zeroth peak and the first peak is separated enough in the Fourier space, so that all information of the real image is contained in the center peak. In this perfect situation, the low pass filtering will completely remove all terms in equation 3.26 except for the real image term. So the resulting hologram is

$$H_{\text{processed}} = OR^*. \tag{3.27}$$

The processed hologram is then propagated as if it's an on-axis hologram. This process is also graphically illustrated in figure 3.11, along with the reconstructed particle using off-axis and in-line holograms.

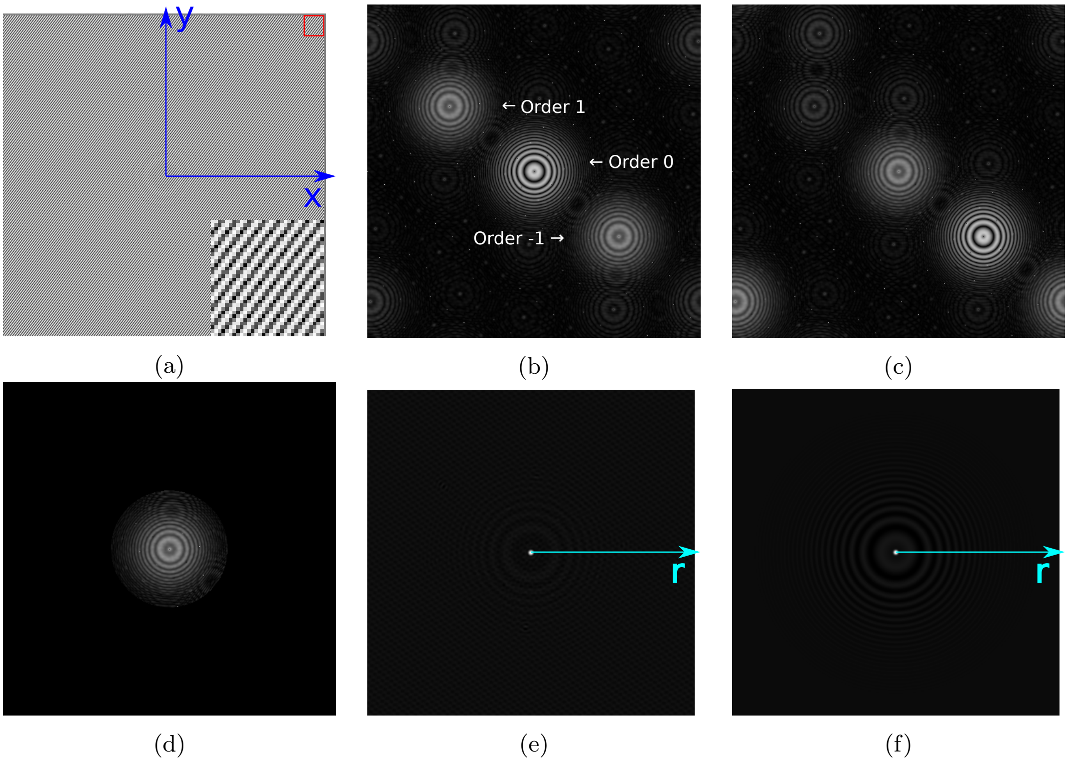

Figure 3.11: Simulated off-axis hologram and the reconstruction process of the simulated hologram. The hologram is simulated using a illumination wavelength of 532nm, and it's captured by a 512×512 array of pixel size $1\mu m$. The object being imaged is a spherical particle of diameter $2\mu m$ located 1mm away from the imaging sensor. (a) The simulated off-axis hologram. The insert is a zoomed-in view of the red square in the top right corner. The zoom-in view corresponds to an area of $30\mu m \times 30\mu m$. (b) The Fourier transformed hologram. (c) The shifted (b) so that the 1st order peak is at the center of the Fourier plane. (d) (c) after low-pass filtering (e) The reconstructed particle at focus position. (f) The reconstructed particle produced by an in-line configuration under the same imaging condition. The DC term has been removed in all Fourier transformed plots to better show the pattern.

By comparing figure 3.11e and figure 3.11f, the virtual image in the reconstruction, which are the rings around the particle, has been greatly suppressed by the off-axis configuration. To better compare the reconstruction result, the radial profiles of the particle construction by two methods is compared in figure 3.12.

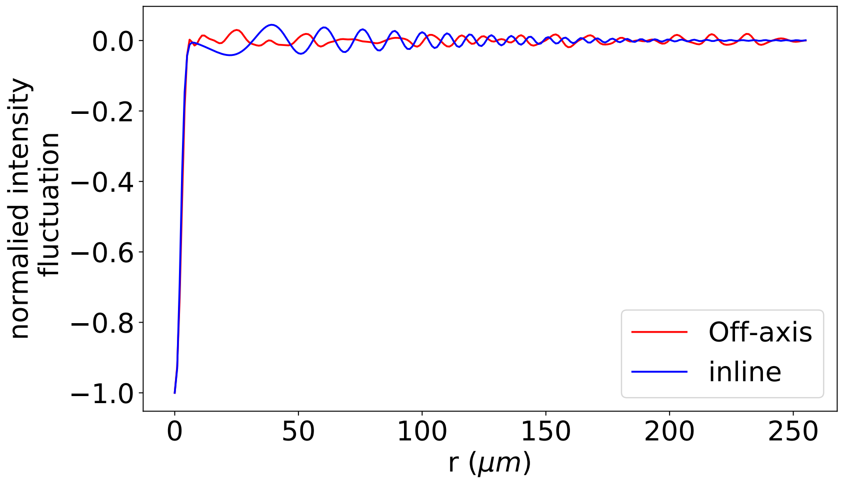

Figure 3.12: Typical experimental set-up of off-axis hologram recording.

Although the off-axis configuration can greatly suppress the virtual image in the reconstruction, because of the low-pass filtering, the spatial resolution of the off-axis holograms is much smaller than that of the in-line holograms and will degrade the reconstruction especially when there are more particles in the volume. Also as in experimentally acquired holograms the Whittaker-Shannon sampling theorem will not be fully satisfied, the processed hologram would be contaminated by the zeroth and higher order peaks, which will also introduce additional noise to the reconstruction. This greatly limits the capacity of the hologram imaging system therefore is not implemented in the 4D-DHPIV/PTV.

3.2 Direct reconstruction of holograms

The direct reconstruction process back track the light propagation numerically using equation 3.10. The object wave extracted from the recorded hologram is propagated to different z position, and the propagated images are stacked together to form the direct reconstruction volume.

The reconstruction volume created by propagation has a few problems. Firstly, when the hologram is taken by the camera, the phase informations is lost. Thus, there is an ambiguity of the direction of propagation of light and both a real and virtual image will be present in the reconstruction, as shown in figure 3.13. The presence of the virtual image in the reconstruction volume introduces additional noise and will decrease the measurement accuracy.

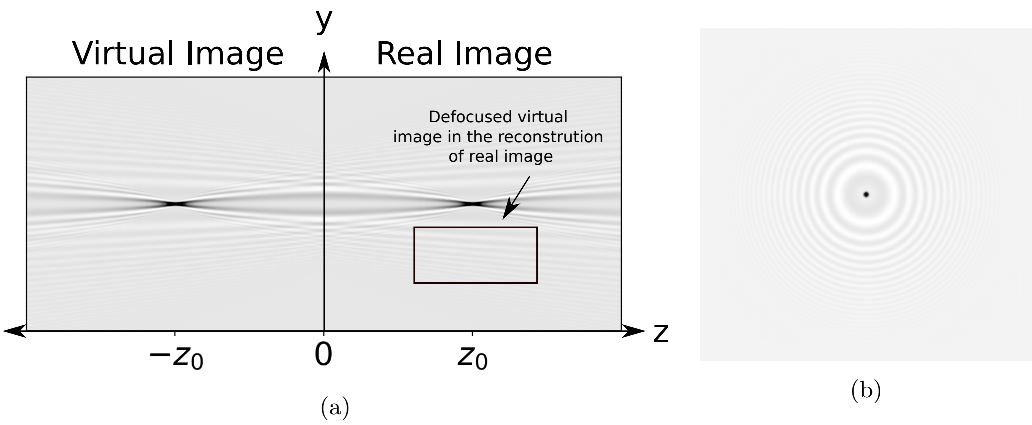

Figure 3.13: (a) y-z plane cut of the directly reconstructed volume through the center of the particle. The hologram is at $z = 0$. (b) x-y plane of the reconstruction at $z = z_0$, showing the focused real image in the center and defocused virtual image around the real image.

Secondly, the limited numerical aperture of the system produces elongated particles in the reconstruction. Because the size of the imaging sensor is typically much smaller than the distance between the sensor and the object, the numerical aperture of holographic imaging is typically much smaller than normal photography, which leads to a larger depth of focus and reconstructed particles looks stretched in the light propagation direction. Instead of the particle being in focus at the particle position only, it is in focus also in front of and behind the particle, therefore the particle looks elongated in the reconstruction. The large depth of focus introduces a large uncertainty in the precise determination of the z position of the particles, which subsequently can result in inaccurate velocity measurement [116].

Thirdly, as the intensity of the diffraction patterns drops rapidly as the particle become further away from the sensor, the pattern is often masked by the brighter diffraction patterns produced by particles which are closer to the imaging plane. Also particles close to the edge of the field of view will produce a diffraction pattern that is only partially recorded, leading to incomplete reconstructions. All the restrictions above limits the field of view of the holographic flow measurement, as well as the maximum particle concentration achievable by this technique.

3.3 Iterative PIV/PTV method adapting an inverse approach

To overcome the shortcomings of the direct recontruction, the proposed iterative 4D-DHPIV/PTV method illustrated schematically in figure 3.14 has been developed and can be briefly summarised as follows. The iterative reconstruction process of the proposed 4D-DHPIV/PTV method starts with a direct reconstruction. The reconstructed volume is deconvolved using a simulated three-dimensional point spread function (PSF) resulting in a deconvolved volume with a higher signal-to-noise ratio, the removal of the twin image and a reduced depth of focus. The intensity distribution of the particles in the deconvolved volume is determined using an efficient 3D clustering algorithm. This is followed by an inverse reconstruction step to improve the determination of the position of the particles by matching the input hologram at each iteration level with a simulated holograms from the detected particles at that iteration level. Once the accurate positions of the particles are found, a simulated hologram using the accurate particle positions is subtracted from the original hologram, exposing additional diffraction fringes resulting in general from particles that are further from the recording plane, smaller in size or outside the projected volume of the image sensor area. This process is repeated (i.e. iterated) until no more further new particles can be found in the hologram because the remaining hologram signal is at the noise level. The velocity field is computed from two particle intensity fields that are separated by a time Δt using a hybrid PIV/PTV method [125]. Furthermore, after 4 time steps, since the trajectory of each particle is known, it is used to predict the corresponding particle location in the subsequent time step by assuming a constant acceleration. This predictive step is used to accelerate all subsequent hologram reconstructions. Each step of the iterative 4D-DHPIV/PTV method shown in figure 3.14 is now presented in more detail.

3.3.1 Deconvolution

In the hologram imaging process, we can assume that the tracer particles are of similar size, and the diffraction pattern created by each particle only exerts a small disturbance on the reference wave so that all particles are illuminated by a planar wave. Under this assumption, the virtual image and the elongated shape of all particles will be the same, and thus can be represented by the three-dimensional convolution between the true particle distribution and a point spread function (PSF) [126], i.e.

$$U(x_0, y_0; z) = \mathcal{F}^{-1}[\mathcal{F}[U_{real}(x_0, y_0, z)]\mathcal{F}[U_{PSF}(x, y, z)]] \tag{3.28}$$

Thus, the true particle distribution field U_{real} can be retrieved using deconvolution. To generate the PSF, a particle with a very small radius (e.g. 10^{-6} of the linear size of the sensor) modelled by equation 3.13 is placed at the centre of the image, and propagated for a distance given from the centre of the reconstruction volume to the imaging plane

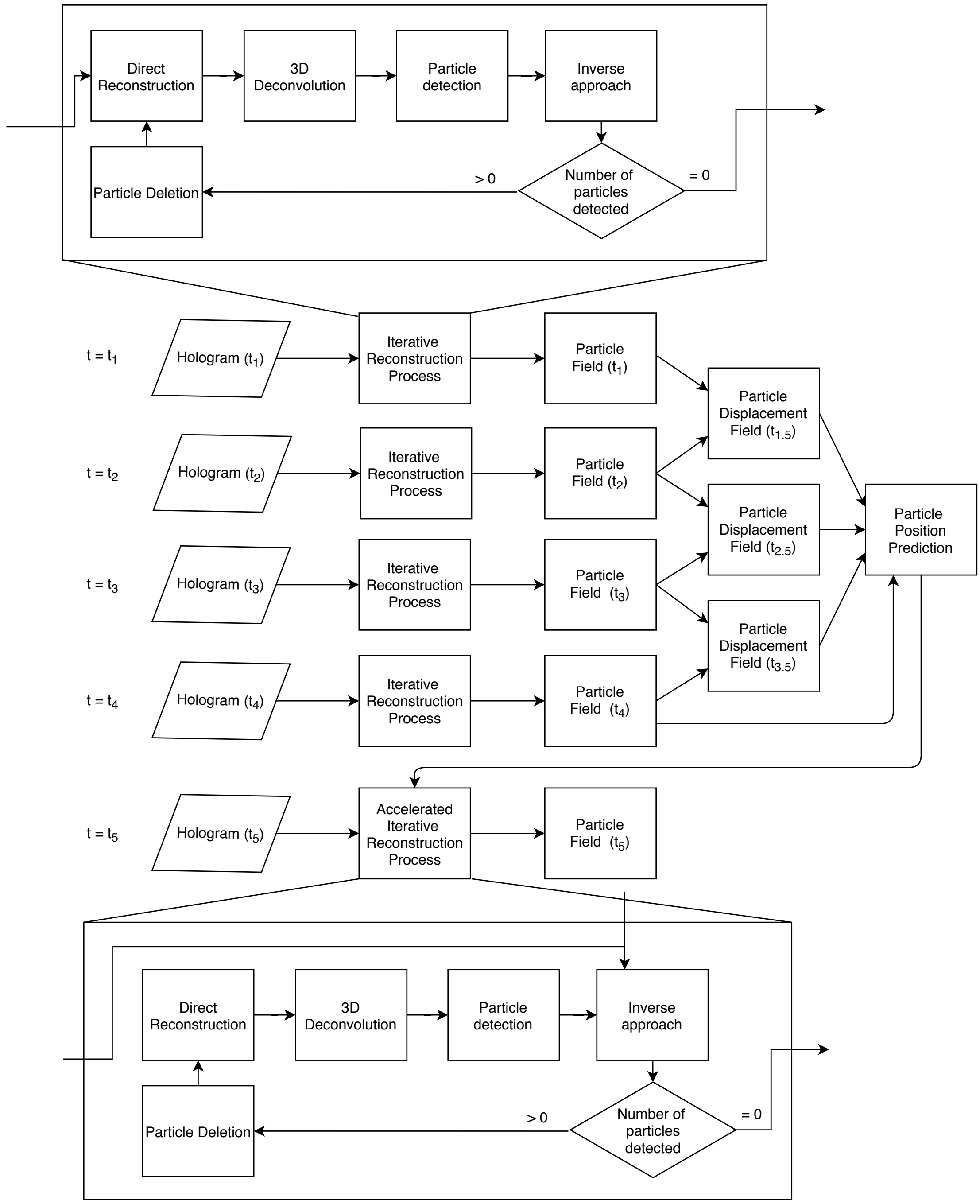

Figure 3.14: Flow chart of the proposed novel iterative 4D-DHPIV/PTV methodology.

where the hologram is recorded. The hologram of the PSF is then propagated to every z-plane corresponding to the reconstruction volume.

Although equation 3.28 can be solved by direct division, any zero value in the $\mathcal{F}[U_{PSF}(x,y,z)$ will create a divide by zero error, thus a small number is added to the $\mathcal{F}[U_{PSF}(x,y,z)$ term before dividing, called direct deconvolution

$$U_{real}(x_0, y_0, z) = \mathcal{F}^{-1}\left[\frac{\mathcal{F}[U(x_0, y_0; z)]}{\mathcal{F}[U_{PSF}(x, y, z)] + \epsilon}\right], \tag{3.29}$$

where the value of ϵ is typically 10^{-4}. However, a problem with direct deconvolution is that typically the high frequency components in both U_{real} and U_{PSF} are zero, resulting in high frequency component in U being zero. In the process of direct deconvolution, U is divided by ϵ where $\mathcal{F}[U_{PSF}] = 0$, therefore the high frequency noise in U is greatly amplified, resulting much noise in the calculated U_{real}. Therefore, another deconvolution method is used in the present algorithm, which is Richardson-Lucy deconvolution.

The Richardson-Lucy deconvolution method is an iterative process aimed at finding the most probable deconvolved field that will produce the input field, based on Bayes theorem [127, 128]. This method has more tolerance to noise than the direct deconvolution by division [126]. The Richardson-Lucy deconvolution method is given by the iterative relationship:

$$\hat{U}_{real}^{(t+1)} = \hat{U}_{real}^{(t)} \cdot \left(\frac{U}{\hat{U}_{real}^{(t)} \otimes PSF} \otimes PSF^*\right) \tag{3.30}$$

In this equation, $\otimes$ is the convolution operator performed by multiplication in Fourier space, $\hat{U}_{real}^{(t)}$ represents the estimated deconvolved volume at t^{th} iteration and PSF^* represents the flipped PSF. Since the PSF is symmetrical for our case, $PSF^* = PSF$. The iterative process starts by setting $\hat{U}_{real}^{(0)}$ to be the averaged value of reconstruction volume, with the iteration stopped when the correlation of $\hat{U}_{real}^{(t)}$ between two iterations reaches 0.9. The result of direct reconstruction followed by deconvolution is shown in figure 3.15.

Note that in the direct reconstruction volume, there is significant noise on both sides of each particle in the z-direction, and the shape of the noise around each particle in the reconstruction volume is the same. After deconvolution, most of the noise around the particles has been removed. However, the particles are still elongated, which can be seen in the zoomed-in view shown in figure 3.15c. Thus, the uncertainty in the location of the z-component of the particle position is still unacceptably high.

3.3.2 Particle detection and inverse approach

In order to find the 3D particle intensity distribution of all reconstructed particles and hence, an estimate of their position from the deconvolved 3D intensity volume, an efficient one-pass 3-dimensional Hoshen Kopelman (HK) clustering algorithm is used [129].

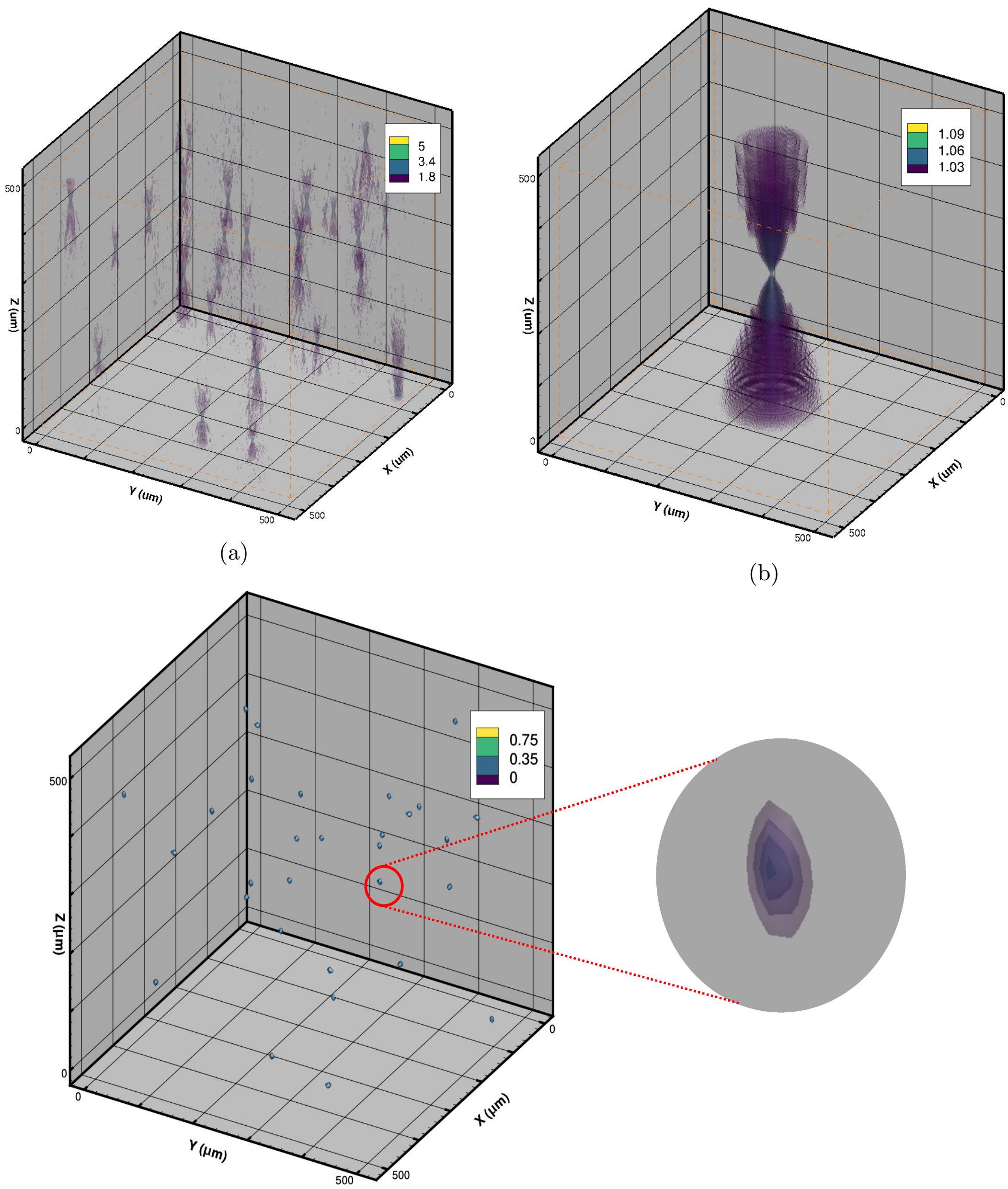

(c)

Figure 3.15: (a) Direct reconstructed volume. (b) 3D point spread function. (c) Deconvolved volume. For better visibility the deconvolved volume has been dilated with spherical structuring element with a larger diameter. The zoomed plot shows the detailed shape of the particle marked in the deconvolution volume.

The optimised threshold for clustering is selected based on percolation theory by finding the threshold for which the number of clusters found in the volume changes the most. Once the 3D particle intensity distributions of all particles are determined using the HK algorithm, their centroids are calculated using an intensity weighted method.

The estimated positions found after the clustering process are then further improved by using an inverse reconstruction approach [130]. In the inverse reconstruction method, a hologram is computed using the particle model described in section 3.3.1 using all the particles that have been detected to this point. The computed hologram is compared with the hologram obtained from the experiment, and the particle position is further improved by minimising the squared difference between two hologram images given by the equation equation 3.31:

$$\epsilon = \Sigma((H_{expeimental} - \bar{H}_{expeimental}) - (H_{simulated} - \bar{H}_{simulated}))^2, \tag{3.31}$$

where the over-bar represents the average intensity value of the hologram. The optimisation variables are the three-dimensional centroid coordinates of the particles, their radii and the amplitude of the perturbation in the simulated hologram. This non-linear optimisation problem is solved using a limited memory Broyden–Fletcher–Goldfarb–Shanno with simple box constraints (L-BFGS-B) algorithm [131]. In this algorithm, the quasi-Newtonian method is used to compute the derivatives of ϵ with respect to the optimisation variables due to the complex nature of this task. Box constraints are imposed on the variation of the optimisation variables to limit the domain of optimisation of the particle positions to within the positional uncertainty from the estimated position, which is typically less than 10λ.

This inverse step with the optimisation process not only finds the required particle characteristics but also identifies “noise particles” that may have been mistakenly identified as particles in the previous steps. As computed hologram produced from the “noise particles” will not produce a good fit to the input hologram with a very low amplitude from this step, simple thresholding of the optimisation result efficiently rejects the false “noise particles”.

3.3.3 Particle deletion

After the accurate particle positions are found, a hologram is computed and subtracted from the original hologram - we refer to this process as “particle deletion”. Particle deletion reveals the interference patterns of the particles which are further away from the hologram imaging plane and were masked by nearer particles, whose holograms have now been removed. This process can significantly increase the number of particles detected from the hologram and expands the maximum field of view in the depth direction. The hologram with the detected particle interference pattern removed then undergoes a further iteration of reconstruction, deconvolution, particle detection, inverse reconstruction and position refinement followed by particle deletion until all particles have been detected and removed from the hologram, and only the noise floor of the hologram remains in the residual hologram as illustrated in figure 3.16.

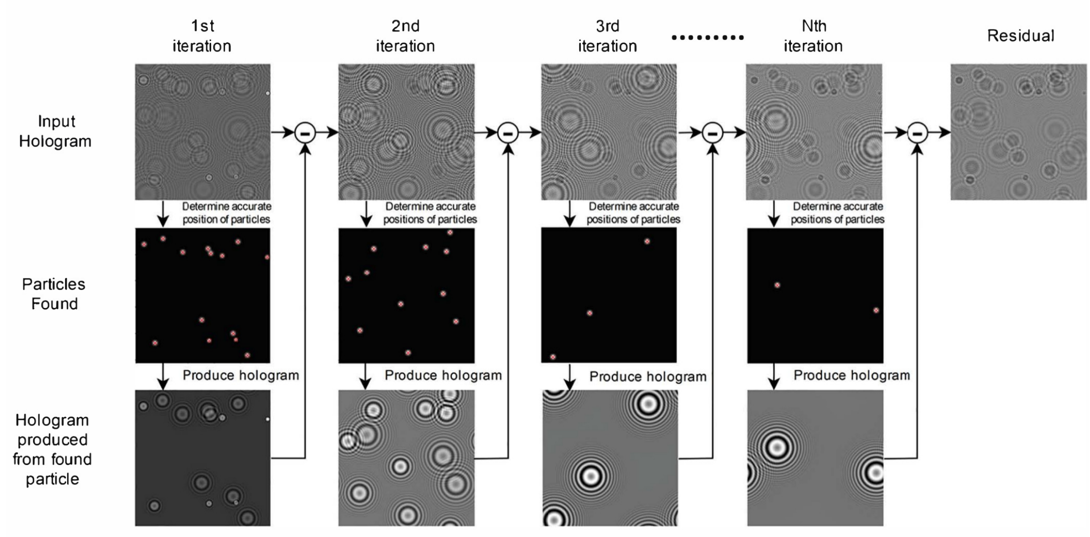

Figure 3.16: The particle removal and iteration process

3.3.4 Velocity extraction and prediction

After all particles are reconstructed in two sequential holograms, a hybrid PIV/PTV method [125] is used to extract the velocity of corresponding particle pairs from the reconstructed volumes produced from the two holograms. Firstly, a 3C-3D cross-correlation PIV analysis is performed on the reconstruction volumes, and the resulting displacement vectors serve as displacement predictors for the identified particle pairs. The displacement predictor significantly decreases the size of the search region in the second reconstruction volume while looking for the particle pair. In order to identify the particle pairs, a smaller interrogation volume (IV) containing the particle is generated within the sequential reconstruction volumes. In the first reconstruction volume, the IV is generated around the detected particle position, whereas, in the second reconstruction volume the IV is generated around the estimated particle position based on the PIV analysis. These corresponding smaller IVs are 3C-3D cross-correlated which yield the particle displacement (PTV) at the spatial resolution of the mean distance between the particles in the reconstructed volume and an IV which effectively is represented by the size of the particle, and therefore this PTV step results in velocity measurements with much higher spatial resolution compared to the velocity found from the 3C-3D cross-correlation PIV analysis.

Once the velocity is known at four consecutive time steps, this PTV information during the trajectory of the identified particle over the last 4 time steps, with an assumption of constant acceleration, is used to predict the position of the identified particle at the next time step. This predicted particle position is then used to accelerate the iterative reconstruction process for the hologram by directly proceeding to the inverse method step as shown in the figure 3.14 [117].

Because of the large amount of analysis required and the iterative nature of the 4D-DHPIV/PTV method, the computational time required to extract velocity vectors from holograms are much longer than the 2C-2D PIV. Although the required computational time and it scaling with key parameters is not thoroughly studied, the analysis of a 64×64 hologram with 20 particles in them requires a average time of around 2.5 CPU hours. The key parameters that will affect the analysis time are hologram size and the number of particles in the hologram. Some parameters, such as the threshold for rejecting particles and the peculation analysis in the clustering step, can also be optimised based on the hologram quality to speed up the analysis process.

3.4 Uncertainty quantification using simulated data

Simulated data is used to analyse the error between exact and measured particle position. In this study, the influence of: (i) particle concentration and (ii) shot noise on measurement uncertainty are investigated.

A hologram with multiple particles is simulated in the following way. Firstly, a reference wave is assumed to have zero phase angle and unit amplitude at the first particle encountered without loss of generality. The transmission function of the particle is given by equation equation 3.13. The scattered light field of the "first" particle is propagated to the z location of the next particle using equation equation 3.10. Note that during the computation of a hologram, the sign of z is opposite from that during reconstruction. Here, the light field is multiplied by the transmission function of the second particle, which is then propagated to the third particle. The process is repeated for all particles encountered along the z-direction until the sensor is reached.

3.4.1 The effect of particle concentration on iterative hologram reconstruction

For this numerical study, the wavelength of the laser illumination is set at $\lambda = 532nm$. Particles were randomly distributed in a volume of $64\mu m \times 64\mu m \times 109\mu m$ where the largest dimension is the out-of-plane z-direction normal to the recording sensor plane. The particles have a diameter uniformly distributed between 1.5 - 2.5 μm ($\sim 2.82\lambda - 4.7\lambda$), which is typical for particles used in air-based experiments or water-based microflow experiments. The numbers of particles used within this volume were 10, 20, 30, 40, 50 and 80, resulting in corresponding particle concentrations of $2.2 \times 10^{-5}, 4.5 \times 10^{-5}, 6.7 \times 10^{-5}, 9.0 \times 10^{-5}, 1.1 \times 10^{-4}$ and 1.8×10^{-4} particles/μm^3, respectively. In terms of particles per pixel, those concentration corresponds to 0.0024, 0.0049, 0.0073, 0.0098, 0.0122 and 0.0195 ppp. The simulated holograms assume a pixel size of 1 μm and are therefore 64 x 64 pixel^2 in size.

The simulation evaluates the intensities of each pixel as the function value at the centre of the pixel. Except for the 80 particles per volume case 18,000 numerical sample volumes were generated and analysed. For the 80 particles per volume case, 7,814 numerical sample volumes were generated and analysed. Figure 3.17 shows the percentage of real particles detected using the direct hologram reconstruction and the iterative hologram reconstruction as a function of particle concentration. These results show the superior performance of the iterative hologram reconstruction approach, which significantly outperforms the direct hologram reconstruction method by correctly identifying more than 70% of all particles even for high particle concentrations, whereas the direct method at the lowest concentration detects at best 35% of all particles. Only for the highest particle concentration does the detection drop to 40% of all particles for the iterative hologram reconstruction approach. However, for this concentration, the direct hologram reconstruction is only able to detect one order less at around 4% of all particles. It is noteworthy to realise that a concentration of 1.1×10^{-4} particles/μm^3 corresponds to 110,000 particles in a volume of 1 mm^3, whereas the highest concentration used here of 1.8×10^{-4} particles/μm^3 corresponds to 180,000 particles in a volume of 1 mm^3, which is an exceedingly high particle concentration and probably never realizable in an experiment.

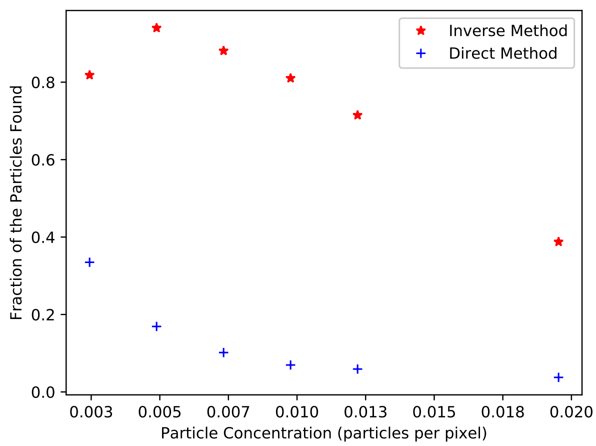

Figure 3.17: Fraction of real particles found using the direct hologram reconstruction method and the iterative hologram reconstruction method as a function of particle concentration.

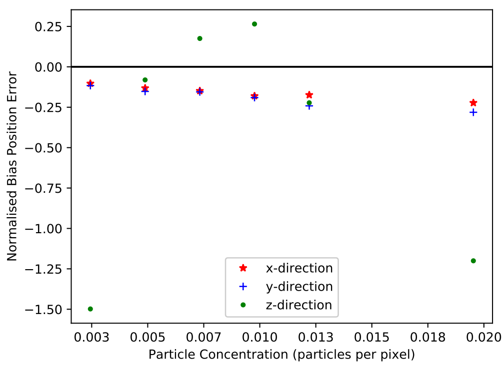

(a)

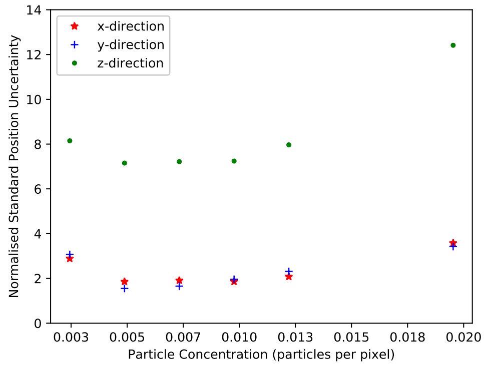

(b)

Figure 3.18: Uncertainty in the particle centroid position using the iterative hologram reconstruction as a function of the particle concentration; (a) Normalised bias error and (b) normalised standard uncertainty. Normalisation is with respect to the wavelength $\lambda = 532$ nm.

Figure 3.18a and figure 3.18b show the normalised bias error and normalised standard uncertainty, respectively, of the particle centroid position in the in-plane (x, y) directions and the out-of-plane z-direction, using the iterative hologram reconstruction. The normalisation is with respect to the illumination wavelength, i.e. $\lambda = 532$ nm. The bias error of the centroid position is typically less than 0.25λ for the in-plane coordinates for all particle concentrations used in this study, characterised by an underestimation. The bias error in the out-of-plane position is of the same order as the in-plane except for the lowest and highest concentration, where the bias error is found to be at most 1.5λ, characterised by both underestimation and overestimation. The standard uncertainty shown in figure 3.18b does not exceed 3.5λ for the in-plane particle centroid coordinates with a minimum at the concentration of 0.0049 ppp of less than 2λ. The standard uncertainty for the out-of-plane particle centroid coordinate is significantly higher and of the order of 8λ or less except for the highest concentration, where the standard uncertainty peaks at slightly above 12λ. The variation of the standard uncertainty for the out-of-plane particle centroid coordinate shadows the in-plane standard uncertainties but with more of a minimum plateau between the particle concentrations of 0.0049 - 0.0122 ppp.

3.4.2 The effect of shot noise on iterative hologram reconstruction

Shot noise, also known as Poisson noise, is unavoiable in experimental holograms, and arises from the quantum nature of light. When light strikes the sensor of the camera, it is in the form of photons, and the sensor counts the number of photos that fall onto each pixel as an intensity reading [132]. However, as each photon must be counted as a whole, and the photons arrive randomly on the sensor, the intensity reading is neither continuous nor exact, but follows a Poisson distribution. Thus, the probability function of the shot noise can be modelled as follows:

$$P\left(a=k\right)=\frac{N^{k}e^{-N}}{k!} \tag{3.32}$$

The most critical parameter in equation equation 3.32 is N, the expected number of events which happens in a given interval. In the context of imaging, the interval is the exposure time, which is kept the same throughout the simulation. Therefore, the value of N for each pixel is directly proportional to the intensity of the incoming light, and its value can be determined by the desired signal to noise ratio of the image. For an image, the signal to noise ratio can be calculated by the following equation [133].

$$SNR=\frac{P_{signal}}{P_{noise}}=\frac{\mu}{\sigma} \tag{3.33}$$

where μ is the average intensity of the noise-free image, which is the average value of N across the image, and σ is the standard deviation of the difference between the noisy image and noise-free image. For a large number of pixels, σ is approximated by the averaged standard deviation of the Poisson distribution for each pixel, which is the square root of N. Thus, the signal to noise ratio can be calculated as follows:

$$SNR=\frac{\mu}{\sigma}=\frac{N_{avg}}{\sqrt{N_{avg}}}=\sqrt{N_{avg}} \tag{3.34}$$

Also, in terms of decibel,

$$SNR_{db}=10\log_{10}\left(\sqrt{N_{avg}}\right) \tag{3.35}$$

Hence, in order to generate a noisy image with a specific signal to noise ratio, the intensity of the noise-free image needs to be scaled so that the average intensity of the image equals the square of signal to noise ratio. Then for each pixel, the pixel value is selected randomly from the Poisson distribution with N equal to the scaled intensity.

The original hologram and the noisy hologram with different signal to noise ratios are shown in figure 3.19. Six cases were investigated in this study with signal-to-noise ratios ranging from 5, 7.5, 10, 12.5 to 15dB, as well as the noise-free case. For each case, more than 600 holograms with 64 × 64 pixels in size containing 20 particles were generated. The simulated volume is $64\mu m\times64\mu m\times64\mu m$, corresponding to a particle concentration of 76,000 particles per mm^3, or 0.0049 ppp. Particles in each hologram are distributed

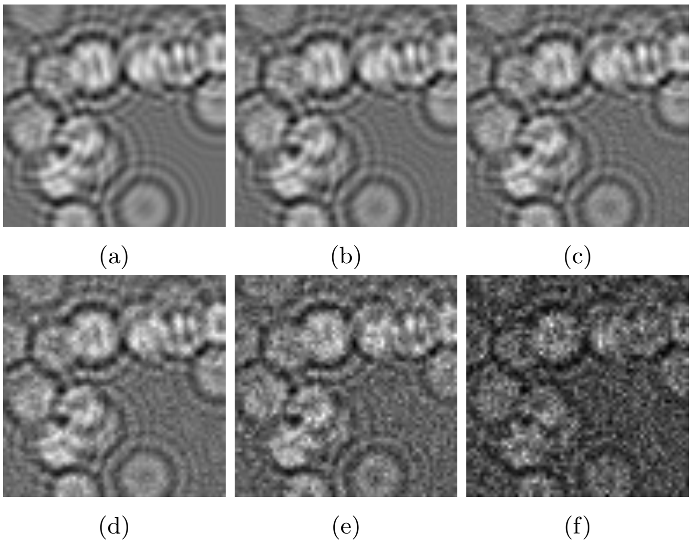

Figure 3.19: (a) The simulated hologram with no noise; (b - f) holograms with additional noise for SNR of 15 dB, 12.5 dB, 10 dB, 7.5 dB, 5 dB respectively.

randomly within the volume located between 50 μm to 100 μm ($\sim 94\lambda - 188\lambda$) away from the imaging plane.

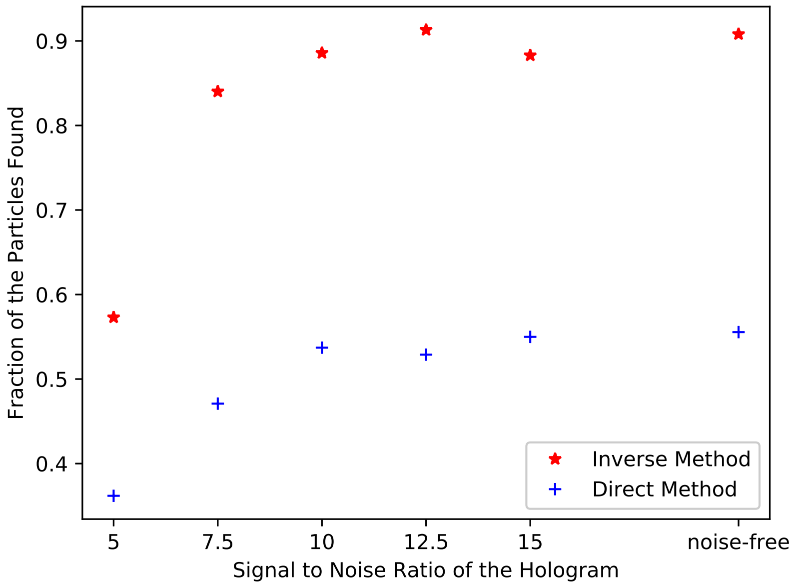

Figure 3.20: The percentage of particles detected using the inverse and direct methods as a function of SNR of hologram.

Figure 3.20 shows that the shot noise adversely affects the percentage of the particles found if the SNR is below 10 for both methods. Except for the SNR equal to the 5 dB and 7.5 dB cases, the inverse method finds about 90% of the particles, while the direct method finds only about 55% of the particles. Thus, the inverse method generally results in an increased number of correctly detected particles in the volume by 60% for all noise levels studied compared to the direct method.

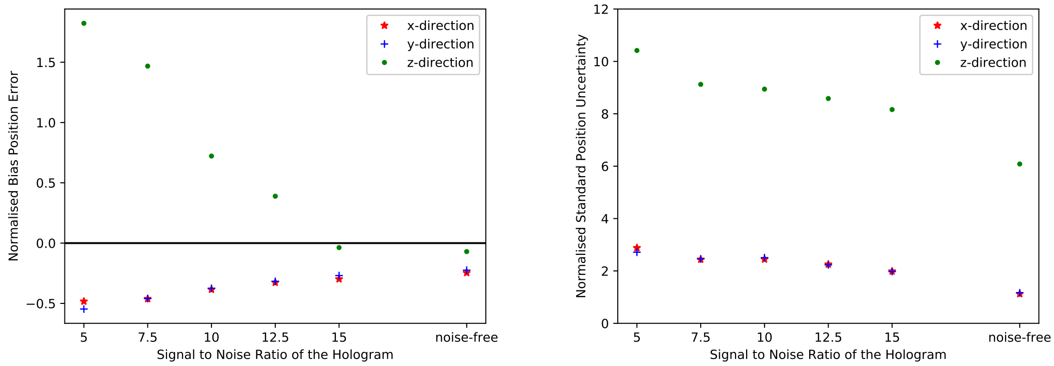

(a) (b)

Figure 3.21: Uncertainty in the particle centroid position using the iterative hologram reconstruction. (a) Normalised bias error and (b) normalised standard uncertainty. Normalisation is with respect to the wavelength $\lambda = 532$ nm.

Figure 3.21 shows that the bias error in x and y directions stays below 0.6λ for all noise level, while in the z-direction the bias error increases from below 0.1λ to approximately 1.8λ as the shot noise in the image increases. The inverse method achieves a standard uncertainty below 3λ in the in-plane directions, while for the out-of-plane direction, the uncertainty reaches 10λ in the noisiest case and is between 8λ and 9λ for the other noisy cases. Generally, the standard uncertainty in the out-of-plane direction is four times the standard uncertainty in the in-plane directions.

3.5 Application of the 4D-DHPIV/PTV method to a micro-channel flow

The 4D-DHPIV/PTV method presented in this section has been applied in a micro-channel flow experiment shown in figure 3.22. A continuous solid-state laser of wavelength 532 nm was used as the illumination source, which is expanded by the beam expander before entering the micro-channel as shown in figure 10. A microscope objective was used to map the camera sensor closer to the volume of interest, resulting in an effective smaller pixel size. The working characteristics of the microscope objective was a magnification of 9.07 times with a numerical aperture of 0.2. A sCMOS camera with physical pixel size 6.5 μm, which mapped to 0.71 μm, was used to record holograms at 15 frames per second. The recorded holograms were 1438 $\times$ 880 pixels in size with the mapped imaging plane 86 μm from the centre of the channel. On average, 330 particles were recorded on each hologram, which corresponds to an approximate particle concentration of 0.0003 ppp.

The requirement of the laser for holographic PIV is different to the laser for 2C-2D PIV. Because the object wave needs to interfere with the reference wave at the camera, the entire optical path needs to be within the coherent length of laser. A typical Nd:YAG laser can't provide long enough coherent length, thus a diode pumped solid-state (DPSS) laser, which typically provides a beam of better coherence, is used. The model number of the laser used is SLIM-532 and it's supplied by OXXIUS. At the mean time, a spatial filter can be incorporated in the light path to increase beam quality. By removing higher order noise, the coherent length is "reset" at the position of the pinhole. However, amplitude of the laser will be greatly reduced at the pinhole, and a laser with high output energy is required to provide enough illumination through the spatial filter.

Because of the small dimensions involved in the measurement, the accuracy of the positioning and the alignment between the laser, camera and lens is beyond the ability of experimental adjustment of the set-up. Therefore, the position and the alignment needs to be measured in-situ and be corrected in the post-processing step. In order to calibrate the set-up, a 1951 USAF resolution test chart is used as the calibration target. The USAF target contains accurately shaped and spaced bars from 500 μm to 2 μm in size, and as the bar spacing is the same as the bar width, their size in pixels can be determined to sub-pixel accuracy by autocorrelation. Three parameters are determined in the calibration process, which are magnified pixel size, illumination beam tiling angle, and illumination beam expansion angle. The magnification is controlled by the distance between the microscopic lens and the camera, and it can be determined by taking a focused image of the USAF target and measuring the spacing of the bars in pixels. Secondly, the camera and the lens are moved away from the calibration target using a micrometre so that the distance moved is known, then a hologram of the target is taken and propagated to the focusing position. By measuring the magnified pixel size of the reconstructed calibration target, the expansion angle of the illumination beam can be found in equation 3.17. Finally, after correcting for the beam expansion, the beam tilting angle can be determined by measuring the relative shift between the reconstructed calibration target and the focused image of the calibration target via cross-correlation. Because the correlation peak positions can be estimated to sub-pixel accuracy, the tilting and expansion angle of the beam can be estimated to the accuracy of 0.001 degrees in a typical experimental set-up, and the reconstruction volume can be corrected accordingly to ensure accurate measurement of the particle positions.

The micro-channel has a width, w = 1.5 mm, a height, h = 50 μm and a length of 40 mm. Polystyrene microspheres (Polysciences Inc.) with a nominal diameter of 1 μm were used to seed the flow, and a syringe pump (KD Scientific) was employed to provide the continuous flow in the micro-channel. The Reynolds number of the flow based on the channel height was 0.1, yielding a laminar flow. Also, as the width of the channel is 30 times the height of the channel, the flow in the channel can be considered to be two-dimensional. The measurement volume was located 20 mm (i.e. 400 h) downstream from the inlet of the micro-channel to ensure that the flow was fully developed at the measurement volume location.

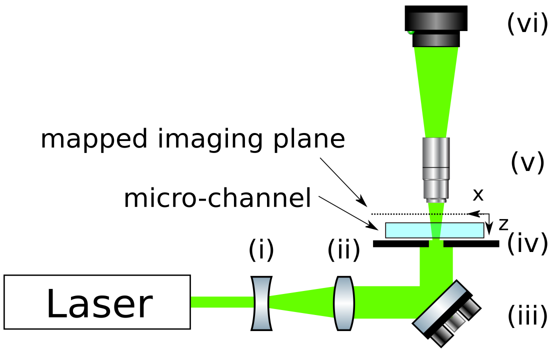

(a)

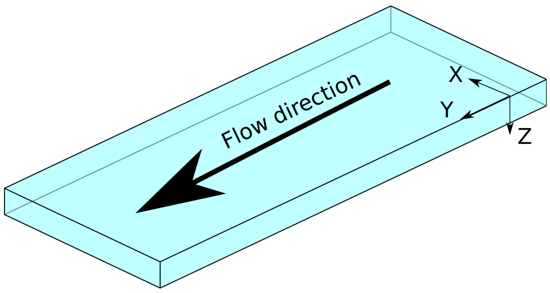

(b)

Figure 3.22: (a)The experimental set-up to demonstrate the DHPIV/PTV method. (i) concave lens (ii) convex lens (iii) mirror (iv) sample table (v) microscope objective (vi) camera. (b) the coordinate system used for the micro-channel flow. (micro-channel size not to scale)

A correction in z scale is required due to the different refractive indices between water and air. In the reconstruction process, it is assumed that the medium of light propagation is uniform. However, in the experiment, the object wave travels from water to glass to air. Hence, as discussed in section 3.1.6, a scale factor will be posed on the reconstruction distance z. As the scattered light from all particles travels the same distance in glass, the relative position between them is not changed. However, as the scattered light travels in water for a different distance, the measured z position of the particles need to be adjusted using equation equation 3.36.

$$z_{real} = z_{measured} \times \frac{n_{glass}}{n_{water}} \tag{3.36}$$

where n_{glass} and n_{water} represents the refractive index of glass and water respectively. Figure 3.23a shows a typical directly reconstructed volume with figure 3.23b showing the deconvolved reconstructed volume prior to the iterative reconstruction steps of the 4D-HPIV/PTV method.

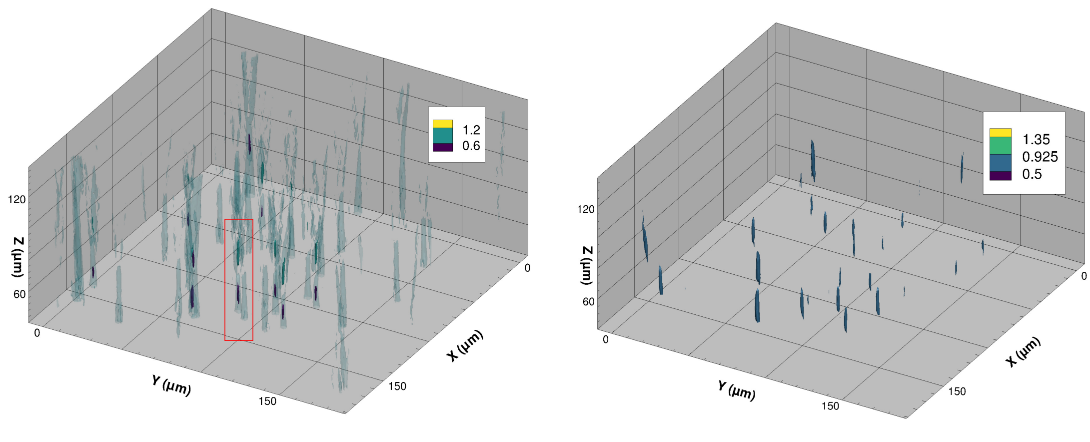

(a) (b)

Figure 3.23: (a) Part of the reconstruction volume generated from experimental hologram. The red rectangle highlights the scattering pattern of a single particle, showing the bright part (green) and the dark part (purple), also presented in figure 3.4d. (b) The corresponding deconvolved volume.

The resulting PTV velocity data is binned into 30 × 30 bins in the x-z cross plane of the micro-channel. Since the flow is fully-developed, the streamwise velocity profile is independent of the streamwise y direction and no binning is required in the y direction. Within each bin, the particle velocities that deviate by more than 1 standard deviation from the mean are discarded. The resulting mean non-dimensional streamwise velocity, V/V_c and non-dimensional standard deviation σ_v/V_c are shown in the figure 3.24, where V_c is the mean centreline streamwise velocity.

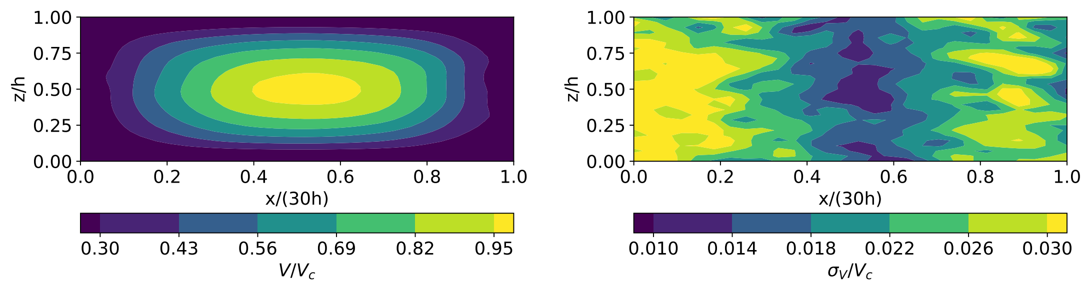

(a) (b)

Figure 3.24: (a) The non-dimensional mean distribution of the streamwise velocity across the channel. (b) The standard deviation of the streamwise velocity.

The standard deviation of the measurement is minimum at the centre of the channel, and increases towards the wall. This is partially because of the higher velocity gradient near the wall, thus the velocity measurements varies more within a bin. Also, there are more particles at the centre of the channel than near the walls, so the velocity gradient near the walls might not be well resolved. Another contributing factor for the high standard deviation, especially in the y direction, is the rounded corner of the micro-channel used for the experiment, which distorts the hologram.

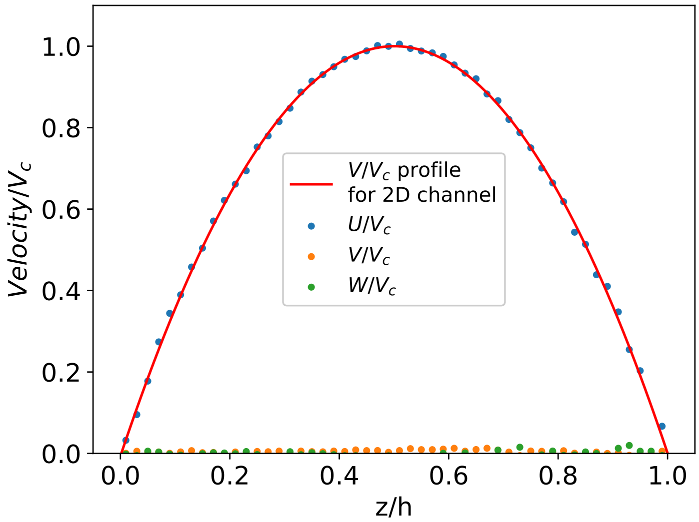

Figure 3.25: The measured velocity profile of the channel flow at the mid-plane in the x direction, with the velocity normalised by the theoretical centreline velocity (V_c = 136.7 μm/s) and the position normalised by the micro-channel depth (h = 50 μm). The 95% confidence interval of the velocity measurement is smaller than the markers. Measurement point omitted at z = 0.98h due to insufficient particles detected in that bin to create a statistically significant measurement.

As the width of the channel is 30 times larger than the height, at the centreline the flow can be assumed to be a 2D laminar channel flow. Figure 3.25 shows the measured velocity profiles at the mid-plane of the channel, i.e. $x = 15h$ and compares it to the theoretical parabolic profile for a 2D laminar channel flow. The agreement is quite good. Comparison of the experimental results of the 4D-DHPIV/PTV method with the theoretical profile indicates a standard uncertainty of 0.38%, 0.93% and 0.85% relative to the centreline velocity, V_c, for the velocity measurements in the x, y and z directions, respectively. Using the uncertainty as the resolution floor for the velocity measurements indicates that the iterative 4D-DHPIV/PTV method can measure turbulence fluctuations down to at least 1% relative to a full-scale deflection.

Chapter 4

High Resolution 2C-2D PIV Measurement of Turbulent Boundary Layer Flow

While the previous chapter presents a novel method to measure the turbulent flow in all three dimensions with high accuracy, this chapter discusses methodology to extract the coherent flow structures from measured velocity fields. As a consequence of the limited access to the laboratory due to the COVID-19 pandemic, it was not possible to set-up the 4D-DHPIV/PTV techniques in the LTRAC turbulent channel flow as was planned as part of this research project and employ 4D-DHPIV/PTV to study turbulent wall-bounded coherent structures. In instead, the results presented in this chapter are produced in an experimental campaign undertaken in late 2019 at the high Reynolds number turbulent boundary layer wind tunnel at the Laboratoire de Mécanique des Fluides de Lille (LMFL). A very high spatial resolution sensor was used to acquire high resolution 2C-2D PIV data.

The study in turbulent boundary layer flow has been ongoing for more than a century, but we still lack a fundamental understanding of its detailed structure and dynamics, particularly at high Reynolds numbers. This is partially due to the lack of experimental data at a sufficiently high Reynolds number with sufficient spatial resolution to resolve and characterise flow structures from its largest energy-containing dynamic scales down to the smallest significant dynamic scales. When performing particle image velocimetry (PIV) measurements, the largest resolvable scale is the size of the magnified imaging array, i.e. the field of view, and the smallest resolvable scale is the size of $\mathcal{O}(10)$ magnified pixels. This suggests that in order to capture the fluid motion of all dynamically relevant length scales, the ratio between the pixel size and the array size, i.e. pixel count, needs to be at least of the same order as the relevant length scale ratio in the flow. However, even for small to medium scale industrial applications, the ratio of the largest to the smallest length scales can reach up to 10^5 and at the time of writing, the resolution required cannot be provided by any single sensor currently available on the market.

Nevertheless, recent developments in sensor technology are now producing commonly available cameras with sensors that have a linear size of over 5,000 pixels, with some recent sensors reaching a linear size exceeding 10,000 pixels. While these sensors still do not yield sufficient spatial resolution to capture all the length scales, utilising such large sensors allows researchers to capture and study turbulent flow behaviour that was previously not possible [134–136], unless multiple cameras are simultaneously used in complex array-type arrangements [137, 138]. Along with all the advantages of using a large sensor, it also introduces more possible source of error into the PIV measurement. For example, the large sensors can induce large imaging angle at the edges of the sensors, introducing perspective error which means the velocity in the out-of-plane direction imprints on the 2C-2D PIV measurement and contaminates the velocity fields. Although there is no method to correct for this error using a single-camera in 2C-2D PIV, the perspective error can be reduced by using long focal length lenses or telecentric lenses [139].

Section 4.1 describes the high resolution 2C-2D PIV measurement of a turbulent boundary layer flow with with a frictional Reynolds number $Re_\tau = 2386$. A single-camera with 47 megapixels is used to capture the flow, which has a field of view of 2.5×1.5 boundary layer thickness defined by the location where the mean velocity reaches 99% of the free-stream velocity and is spatially resolved to 5.4 wall units in the wall-normal direction.

Section 4.2 presents a detailed analysis of the uncertainly in the dewarping functions caused by the uncertainties in measuring the physical positions of the calibration markers on the target, as well as uncertainties in measuring the position of markers in the calibration image, when second-order rational functions and third-order polynomials are used to model lens distortion. Furthermore, from the analysis it was found that the bias error produced by the lens distortion locally within an interrogation window is comparable or below the uncertainty of a typical PIV measurement and therefore, indistinguishable from the experimental uncertainty of 2C-2D PIV. Thus, a simplified image dewarping approach is suggested, whereby the 2C-2D cross-correlation digital PIV analysis is performed on the uncorrected images, and the velocity vector positions are shifted to the corrected positions using the dewarping functions determined from calibration. This approach is applied to high spatial resolution (HSR) 2C-2D PIV measurements of a zero-pressure-gradient turbulent boundary layer (ZPG-TBL), and its performance is compared via the corresponding velocity statistics with the traditional method of dewarping the distorted images prior to 2C-2D cross-correlation digital PIV analysis.

Section 4.3 uses Proper Orthogonal Decomposition (POD) to extract coherent flow structures from the 2C-2D velocity fields. POD is one of the tools available to characterise and study the dominant features of a turbulent flow by capturing the most energetic patterns observed in the data. In the context of fluid dynamics, the patterns captured by POD analysis correspond to coherent flow structures in the turbulent flow [140]. Since POD is purely a data-driven analysis, in order to produce the POD modes that accurately represent the dominant features in the flow, enough velocity fields need to be provided to the algorithm for the analysis. This aspect is investigated in section 4.3 where the number of velocity fields required for a high-fidelity representation of the persistent structures in the turbulent boundary layer flow is studied via a convergence test of the eigenvalues of the most dominant POD modes.

Section 4.4 explores how the large scale motions (LSMs) affect the skin friction of the turbulent boundary layer. Specifically, the turbulent kinetic energy production term identified by Renard-Deck decomposition (RD decomposition) of the skin friction coefficient [141]. In the RD decomposition, the mean friction coefficient is decomposed in an absolute reference frame into a viscous dissipation term, a turbulent kinetic energy production term, and a boundary layer growth term. As the coherent structures are an essential mechanism of turbulent production, the relationship between the presence of LSMs and the value of the turbulent kinetic energy term in RD decomposition is studied using conditional sampling.

4.1 HSR PIV Measurements of high Reynolds number ZPG-TBL

The HSR 2C-2D PIV experiments were carried out in the High Reynolds Number Boundary Layer Wind Tunnel of the Laboratoire de Mécanique des Fluides de Lille (LMFL). This wind tunnel has a streamwise test section length of $20.6m$, and a cross-sectional area of $2m$ wide by $1m$ high. The facility is constructed using a metal frame with high quality $10mm$ thick glass walls along the entire test section providing complete optical access throughout its test section.

The free-stream flow velocity for the experiment was set to $U_\infty = 9m/s$ at the inlet of the test section with the measurements taken $6.8m$ downstream of the tripping location of the turbulent boundary layer. The ZPG-TBL at the measurement location has a Reynolds number based on the momentum thickness, $Re_\theta = 8,120$, a boundary layer thickness defined by the location where the mean velocity reaches 99% of the free-stream velocity of $\delta \approx 103mm$ and a viscous length $l^+ \approx 40\mu m$.

The wind tunnel was seeded using a water/glycol smoke generator for the PIV experiments, which generated seeding particles with a mean diameter $d_p \approx 1\mu m$ [138]. HSR 2C-2D PIV images were acquired in a streamwise – wall-normal plane located along the centreline of the wind tunnel. The field of view (FOV) was $254mm$ long in the streamwsie direction by $152mm$ high in the wall-normal direction, which was illuminated using a dual-cavity BMI Nd:YAG laser with an output energy of $200mJ$ per pulse at a wavelength of $532nm$. The laser sheet was formed using two spherical lenses with focal length $-800mm$ and $500mm$, as well as two cylindrical lenses with focal lengths $-60mm$ and $-25mm$, resulting in a light sheet thickness of approximately $300\mu m$ across the FOV.

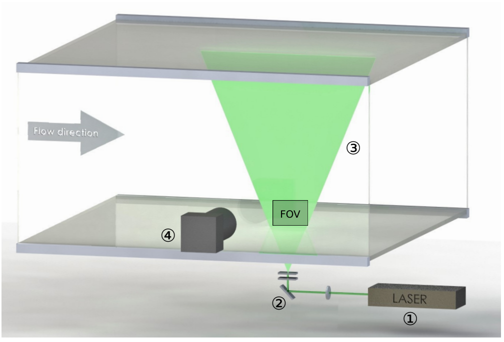

Figure 4.1: Experimental set-up 1: dual pulse laser 2: sheet forming optics 3. laser sheet 4. camera

The single-exposed PIV images were acquired using an Imprex Tiger T8810 CCD camera with 47 megapixel array and a dynamic range of 12 bits. The camera's sensor has a pixel array of $8,864 \times 5,288$ with a pixel size of $5.5\mu m$, resulting in a $48.7mm \times 29.0mm$ ($56.7mm$ diagonal) array. The synchronisation between the pulses of the Nd:YAG laser and the camera is the same as used in previous PIV experiments in the same facility [138].

This sensor size is larger than the full-film DSLR cameras, requiring a suitable lens to minimise distortion over the entire image. The use of an unsuitable lens will result in large lens distortion at the edges and corners of the image that will invalidates the premise introduced in the introduction section that the local velocity measurement remains unaffected by lens distortion within the experimental uncertainty of 2C-2D cross-correlation digital PIV analysis with only the spatial location of the 2C-2D velocity measurement affected by the lens distortion, which will not allow the application of the simplified distortion correction method presented in this paper. In the presented experiments, a telephoto lens (Hasselblad Zeiss Sonnar 250mm f/5.6) with a $45mm$ extension tube was used. This lens is designed for medium format films with a clear aperture of $80mm$ and less than 1% distortion across the entire image. The long focal length of this lens enables the camera to be further away from the imaged object plane with light rays at the edge of the sensor to be nearly perpendicular to the sensor, thus, minimising the perspective error in the 2C-2D PIV. Furthermore, the high dynamic range of the camera ensures that the full image has sufficient contrast, even where the illumination is reduced due to vignetting. The camera lens combination was used to image the near-wall region of the high Reynolds number ZPG-TBL at a large magnification of $M = 0.19$, corresponding to a pixel size of $28.9\mu m$ in object space, resulting in a measurement area of $2.46\delta \times 1.45\delta$. The imaging set-up is shown in figure 4.2.

In order to account for the increase in magnification and the reduced laser sheet thickness, the seeding was increased by a factor of approximately 3 to 4 in comparison to the similar previous PIV experiments in the same facility reported by [138]. This was necessary given the significantly higher spatial resolution of the present study to ensure that there was an optimal amount of seeding particles illuminated in the images for the subsequent 2C-2D cross-correlation digital PIV analysis. The single-exposed PIV image pairs were processed using an in-house multigrid/multipass 2C-2D cross-correlation digital PIV analysis algorithm [84]. The PIV acquisition parameters are summarized in table 4.1.

All 2C-2D PIV experiments suffer from perspective error caused by the imaging light rays not being perpendicular to the focusing plane. This results in the normal velocity of the seed particles within the 2D light sheet being projected onto the in-plane velocity components measured by 2C-2D PIV, which produces a bias error in the 2C-2D PIV velocity fields [142]. The perspective error cannot be corrected with post-processing when only one camera is used to record the single-exposed PIV images. However, it can be reduced by using a long focal length imaging lens and placing the camera as far away from the imaging plane as possible. In the present experiment, a $250mm$ focal length lens is used, which allows the camera to be located approximately $1.5m$ from the measurement plane resulting in a maximum imaging angle at the corner of the image of 0.02 radians. Assuming that the out-of-plane displacements in the turbulent boundary layer have approximately the same magnitude as the wall-normal displacements, which is of the order of 1.5 pixels, the maximum perspective error introduced in the PIV measurement is expected to be 0.03 pixels. This additional bias error is less than the measurement uncertainty of 2C-2D cross-correlation digital PIV analysis [84] and would not be detectable in the measurement.

In this study, the streamwise, wall-normal and spanwise direction of the ZPG-TBL are denoted by x, y and z respectively, with the respective velocity components denoted by

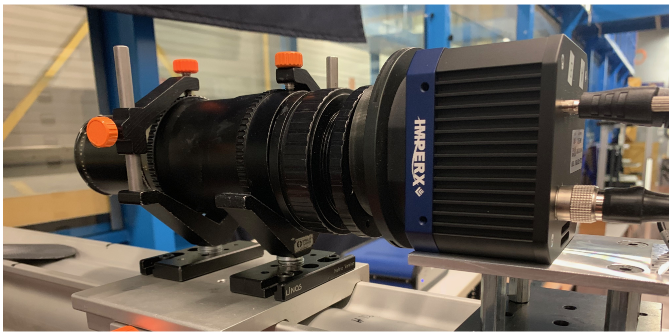

Figure 4.2: Imaging setup for the present experiment including a 47 MPixel CCD camera and a 250mm-focal-length telephoto lens with extension tube.

u, v and w. The mean velocities in the x, y and z are denoted by U, V and W respectively, while the corresponding fluctuating velocities are denoted by u', v' and w'. An overbar $\overline{\square}$ represents the ensemble average of the variables encompassed by it, while hatted variables $\hat{\square}$ represent normalised variables by a reference scale.

Table 4.1: The PIV acquisition parameters for ZPG-TBL measurements

Property	Symbol	Units	Value
Free stream velocity	U_∞	ms^{-1}	9.64
Friction Reynolds number	Re_τ		2,386
Number of samples	N		34,535
Field of View	FOV	mm	255×152
	FOV	δ	2.46×1.45
PIV final window size	IW_x	$pixel$	32
in streamwise direction	IW_x	μm	927
	IW_x^+	l^+	21.7
PIV final window size	IW_y	$pixel$	8
in wall-normal direction	IW_y	μm	232
	IW_y^+	l^+	5.42
PIV measurement volume	IW_z	μm	400
in spanwise direction	IW_z^+	l^+	4.68
Uncertainty in mean velocity	ϵ_U		0.825%
Uncertainty in the Reynolds normal stresses	$\epsilon_{uu}, \epsilon_{vv}$		0.381%
Uncertainty in the Reynolds shear stress	ϵ_{uv}		0.695%

4.2 Image dewarping procedure †

Since the severity of lens distortion typically increases monotonically from the centre of the lens towards its edge, large sensors are more prone to lens distortions and subsequently require the use of high quality long focal length lenses. Traditionally, lens distortion has been modelled using the Brown–Conrady model [143, 144] that separates distortion into a radial and tangential component, which are corrected independently. However, because the radial and tangential components are typically coupled in an optical system, this approach has not been found to be suitable, and more generalised distortion models, such as the use of a bicubic polynomial function (P3) and a second-order rational function (R2) have been proposed to rectify image distortion by Soloff et al. [145], Scarano et al. [146]. A polynomial containing the second-order and the fourth-order terms has also been suggested as a lens distortion model [147]. Correction of image distortion has been mainly investigated in the context of stereo PIV (SPIV) and tomographic PIV (TPIV) [148, 149], where it has been used to correct for the perspective error introduced by the position of the cameras. However, it is overlooked in the case of 2C-2D PIV and seldom corrected for or reported. Therefore, the awareness and significance of this source of error when using large imaging sensors in 2C-2D PIV needs to be raised.

This section also describes a detailed analysis of the uncertainty in the dewarping functions caused by the uncertainty in measuring the physical positions of the markers on the calibration target, as well as the uncertainty in measuring the position of the markers in the image of the calibration target for the second-order rational functions and third-order polynomials used to model lens distortion. This analysis found that the bias PIV error produced by the local lens distortion within an interrogation window is comparable or below the uncertainty of a typical PIV measurement and therefore, indistinguishable from the experimental uncertainty of 2C-2D PIV. This result suggested a simplified correction approach to 2C-2D PIV using large sensors affected by lens distortion. This new simpler and computationally more efficient approach is compared by applying it, and the more traditional approach of dewarping the raw single-exposed PIV images prior to 2C-2D cross-correlation digital PIV analysis, to high spatial resolution (HSR) single-exposed PIV images of a high Reynolds number zero-pressure-gradient turbulent boundary layer (ZPG-TBL). The comparative performance of both approaches is evaluated via the corresponding turbulent velocity statistics derived from the corrected HSR 2C-2D PIV of the high Reynolds number ZPG-TBL.

4.2.1 Image rectification procedure

The dewarping process of the raw single-exposed PIV images is performed in three steps. The first step is to select a suitable image distortion model and compute the parameters in the mapping function based on the measured locations of the markers on the calibration target and the markers on the image of the calibration target. An image of the calibration target used in these experiments is shown in figure 4.3. In the second step, the shape and position of a reference geometry obtained from PIV is used to correct any misalignment between the calibration target and the flow. Thirdly, the lens distortion correction is applied during the PIV analysis process. Each of these steps is now described in detail in the following three subsections.

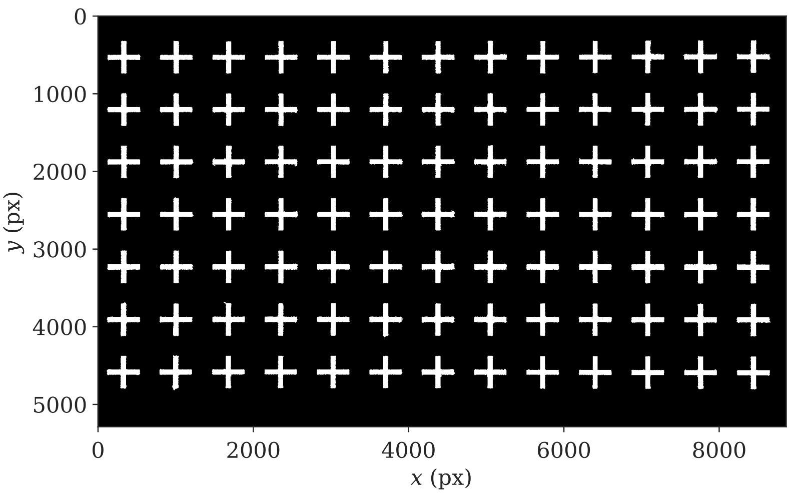

Figure 4.3: The preprocessed calibration target image. Because the lens distortion is very little, the distorted and correct positions and the shapes of the markers are visually undistinguishable when the whole image is presented.

4.2.1.1 Dewarping model selection and mapping function parameter estimation

In order to correct the distortion in the PIV images, a suitable mapping function must to be chosen that is based on the distortion characteristics of the imaging system. The free

† Content of section 4.2 has been published on Experiments in Fluids, see
Bihai Sun, Muhammad Shehzad, Daniel Jovic, Christophe Cuvier, Christian Willert, Yasar Ostovan, Jean-Marc Foucaut, Callum Atkinson, and Julio Soria. Distortion correction of two-component – two-dimensional piv using a large imaging sensor with application to measurements of a turbulent boundary layer flow at $Re_\tau = 2,386$. *Experiment in Fluids*, 2021

parameters in the mapping function are estimated from the location of known object points in object space and the location of the corresponding image points in image space. A simple first order rational (R1) mapping function that maps object points to corresponding image points is given as [150]:

$$\begin{aligned} \hat{x}_i &= \frac{a_{11}\hat{x}_o + a_{12}\hat{y}_o + a_{13}}{a_{31}\hat{x}_o + a_{32}\hat{x}_o + a_{33}}, \\ \hat{y}_i &= \frac{a_{21}\hat{x}_o + a_{22}\hat{y}_o + a_{23}}{a_{31}\hat{x}_o + a_{32}\hat{y}_o + a_{33}}, \\ a_{33} &= 1 \end{aligned} \tag{4.1}$$

where $(\hat{x}_o, \hat{y}_o)$ are the normalised coordinates of the object points and $(\hat{x}_i, \hat{y}_i)$ are those of the corresponding image points. Both coordinate systems assume to have their origin located on the centre marker of the calibration target where minimum lens distortion is expected. The eight unknown best fit coefficients are estimated using a nonlinear least-squares method such as the Levenberg-Marquardt method [151]. While it is straightforward to compute and apply the R1 dewarping function, it only allows for perspective projection of a rectangle onto a four-sided polygon, thus preserving the line-straightness, but does not correct any radial or tangential distortion in the PIV images, which is typically what is present when PIV images are recorded with a large array sensor. Therefore, correcting radial distortion requires a second-order rational function R2 [150]. R2 is a simple extension of the first-order polynomials in R1 to second-order given by:

$$\begin{aligned} \hat{x}_i &= \frac{a_{11}\hat{x}_o + a_{12}\hat{y}_o + a_{13} + a_{14}\hat{x}_o^2 + a_{15}\hat{x}_o\hat{y}_o + a_{16}\hat{y}_o^2}{a_{31}\hat{x}_o + a_{32}\hat{y}_o + a_{33} + a_{34}\hat{x}_o^2 + a_{35}\hat{x}_o\hat{y}_o + a_{36}\hat{y}_o^2}, \\ \hat{y}_i &= \frac{a_{21}\hat{x}_o + a_{22}\hat{y}_o + a_{23} + a_{24}\hat{y}_o^2 + a_{25}\hat{x}_o\hat{y}_o + a_{26}\hat{y}_o^2}{a_{31}\hat{x}_o + a_{32}\hat{y}_o + a_{33} + a_{34}\hat{x}_o^2 + a_{35}\hat{x}_o\hat{y}_o + a_{36}\hat{y}_o^2}, \\ a_{33} &= 1 \end{aligned} \tag{4.2}$$

More recently, [152] suggested a third-order polynomial function (P3) given by equation 4.3 for image dewarping because it can account and therefore, correct non-axisymmetric radial distortion. Although third and higher degree polynomial functions lack any physical interpretation, they provide a better fit to the measured distortion field and are less prone to numerical errors.

$$\begin{aligned} \hat{x}_i = a_{01} + a_{02}\hat{x}_o + a_{03}\hat{y}_o + a_{04}\hat{x}_o^2 + a_{05}\hat{x}_o\hat{y}_o + a_{06}\hat{y}_o^2 \\ + a_{07}\hat{x}_o^3 + a_{08}\hat{x}_o^2\hat{y}_o + a_{09}\hat{x}_o\hat{y}_o^2 + a_{10}\hat{y}_o^3, \\ \hat{y}_i = a_{11} + a_{12}\hat{x}_o + a_{13}\hat{y}_o + a_{14}\hat{x}_o^2 + a_{15}\hat{x}_o\hat{y}_o + a_{16}\hat{y}_o^2 \\ + a_{17}\hat{x}_o^3 + a_{18}\hat{x}_o^2\hat{y}_o + a_{19}\hat{x}_o\hat{y}_o^2 + a_{20}\hat{y}_o^3. \end{aligned} \tag{4.3}$$

The P3 and R2 mapping functions require the determination of 20 and 18 coefficients, respectively. The calibration image contains 91 markers providing sufficient data to determine the unknown coefficients in a least-square sense.

The process used to calculate the unknown coefficients of the mapping functions $\hat{x}_i = f_x(\hat{x}_o, \hat{y}_o)$ and $\hat{y}_i = f_y(\hat{x}_o, \hat{y}_o)$ is as follows:

1. The positions of the 91 markers $\{P_I\}$ in the image space of the calibration image are determined by cross-correlating the image with a marker template and finding the peak locations to sub-pixel accuracy using a 2D Gaussian fit [84]. The uncertainty in the marker positions in image space is estimated as an ensemble average of the uncertainties of a 2D Gaussian curve fit to the peak locations in the correlated calibration image, given as a standard uncertainty by $(\sigma_{x_i}, \sigma_{y_i}) = (0.057, 0.057)\ px$.

2. In object space, the horizontal and vertical distance $(\Delta x_o, \Delta y_o)_j$ between markers is measured from the calibration target, from which the mean distance between markers in the horizontal and vertical direction given by $(\overline{\Delta x_o}, \overline{\Delta y_o})$ with corresponding standard deviations of $(\sigma_{x_o}, \sigma_{y_o})$ are calculated. The latter is an estimate of the standard uncertainty in locating the markers in object space. For the present study, these values are: $\overline{\Delta x_o} = \overline{\Delta y_o} = 19.510\ mm$ and $\sigma_{x_o} = \sigma_{y_o} = 20\ \mu m$.

3. The magnification is estimated from the distance between the centre marker and the adjacent four markers around it in image space, since the distortion is minimum at the centre of the image.

4. The positions of the markers in object space $\{P_O\}$ are determined using the physical positions of the markers and the magnification found in the previous step.

5. The image space $\{P_I\}$ and the object space $\{P_O\}$ coordinates are measured relative to the marker in the centre of the image, which is defined as the origin of both the object and image Cartesian coordinate systems (*i.e.* P_{Oc} and P_{Ic}, respectively).

6. The Cartesian coordinate systems for image and object space are further normalized as follows:

$$\{\hat{P}_I\} = \frac{\{P_I\} - P_{Ic}}{L_{ref}} \tag{4.4}$$

$$\{\hat{P}_O\} = \frac{\{P_O\} - P_{Oc}}{L_{ref}}, \tag{4.5}$$

   where L_{ref} represents a reference scale, conveniently taken as the width of the image. The marker in the centre of the image is chosen as the origin for both object and image coordinates because this location is near the optical axis and represents a position with minimum optical distortion. The coordinates are normalised in both spaces to minimise numerical errors in the least square computation of the coefficients of the mapping functions. Figure 4.4 shows the object point coordinates along with arrows pointing towards the corresponding image point coordinates, clearly showing that there is very little distortion in the middle of the image compared to the edges and corners of the image, where there is considerable pincushion distortion. The reason for the larger distortion on the right side of the image compared to the left side is due to a small misalignment between the optical axis of the lens and the centre of the imaging sensor. Therefore, although the origin of the coordinate system is near the centre of the image, the centre of the lens distortion is shifted by a small distance towards the left.

7. Lastly, the coefficients of the R2 and P3 mapping functions are determined using the Levenberg-Marquardt method for nonlinear least-squares curve-fitting [151]. The characteristic parameters determined from the calibration image and used to estimate the free parameters in the mapping functions are summarised in table 4.2.

Table 4.2: The characteristic parameters to compute the dewarping coefficients of the equations 4.2 and 4.3.

Property	Symbol	Units	Measurements
Pitch of object points	$\overline{\Delta x_o}, \overline{\Delta y_o}$	(mm)	19.510 ± 0.020
Resolution	M	(px/mm)	34.538 ± 0.5
Center point of the image space	P_{Ic}	(px)	(4,380.356, 2,555.753)
Center point of the object space	P_{Oc}	(px)	(4,380.906, 2,559.182)
The maximum absolute error in curve fit (R2/P3)	$L_{ref}\left[\hat{P}_I - \left(f_x(\hat{P_O}), f_y(\hat{P_O})\right)\right]_{max}$	(px)	(1.577, 1.517)/(1.742, 1.290)
The mean error in curve fit (R2/P3)	$L_{ref}\overline{\hat{P}_I - \left(f_x(\hat{P_O}), f_y(\hat{P_O})\right)}$	(px)	(0.0, 0.0)/(0.0, 0.0)
The standard uncertainty in curve fit (R2/P3)	$L_{ref}\sigma_{[\hat{P}_I - \left(f_x(\hat{P_O}), f_y(\hat{P_O})\right)]}$	(px)	(0.836, 0.681)/(0.868, 0.508)

4.2.1.2 Aligning the flow with the calibration target

Since the mapping parameters are determined from the image of the calibration target and not the PIV images themselves, an error can be introduced due to the misalignment

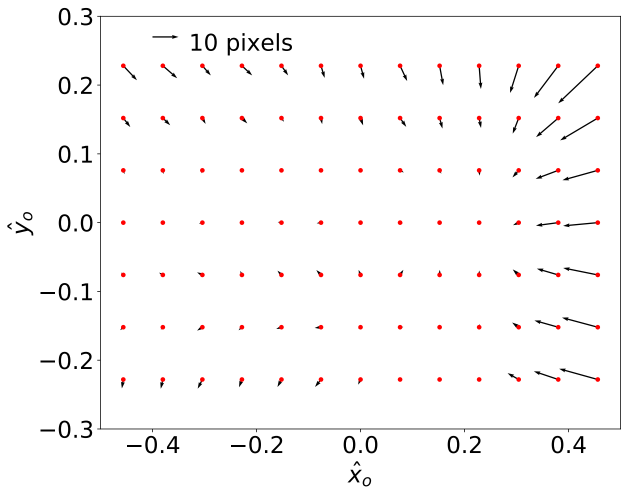

Figure 4.4: Object points (the red markers) with arrows pointing towards the corresponding image points. To help visualize, the arrows have been enlarged by a factor of 20.

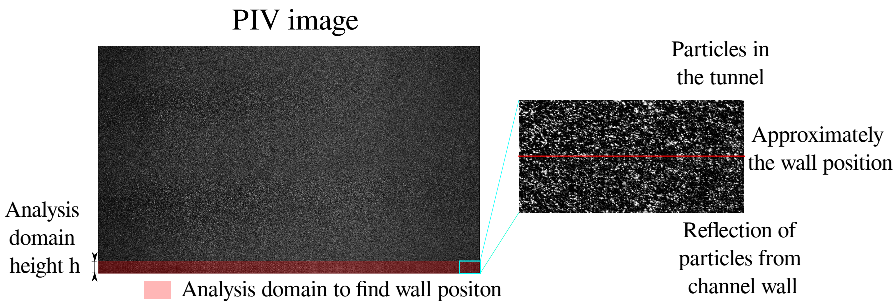

Figure 4.5: Sample image taken in the experiment, with analysis domain for wall position marked

between the mean free-stream flow direction and the calibration target. A minor rotation or translation in the out-of-plane direction will not significantly change the mapping function parameters, as the distortion of the lens will not change greatly over a small displacement in the out-of-plane direction. However, since the sensor size is large, any rotation of the calibration target in the in-plane direction will create a significant error in the dewarped image, especially near the corners. Therefore, the orientation of a reference geometry, for example, the wall in the boundary layer flow, needs to be determined from the PIV images to correct for any in-plane rotation of the calibration target relative to the flow. In order to perform the necessary correction, part of the tunnel wall, as well as the reflection of the particles from the glass tunnel floor are recorded in the PIV images, as shown in figure 4.5.

The 2C-2D cross-correlation digital PIV analysis of a sample of single-exposed PIV image pairs near the plate yields a mean streamwise velocity profile that is symmetric about the plate surface due to the plate surface reflection of the seed particles as shown in figure

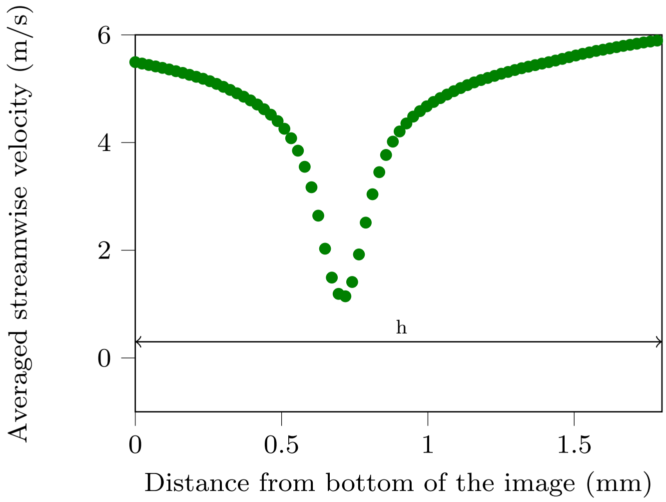

Figure 4.6: Streamwise velocity profile near the wall at one streamwise location, the line of symmetry in the velocity profile indicates the position of the wall at that streamwise location.

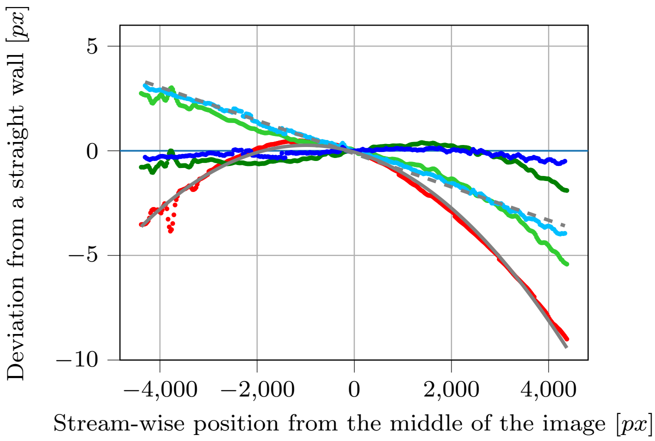

Figure 4.7: The apparent shape of the flat channel wall evaluated from the PIV analysis of original and dewarped images. •: Distorted image. •: Corrected image using R2 dewarping model. •: Corrected and rotated image using R2 dewarping model. •: Corrected image using P3 dewarping model. •: Corrected and rotated image using P3 dewarping model. —: Parabolic fit to distorted wall position. - - -: Linear fit to dewarped wall position (P3), rotation angle 0.04°.

4.6. Hence, the determination of the line of symmetry in the mean velocity profile yields an accurate determination of the location of the wall. The line of symmetry is found by a shift between the velocity profile with the flipped profile, d, which is determined to sub-pixel accuracy using a 1D Gaussian fit to the peak of the cross-correlation function. This allows the wall position at each x position along the wall to be calculated as:

$$\text{Wall position}(x) = \frac{h - d(x)}{2}. \tag{4.6}$$

This process is repeated to calculate the wall position for every streamwise location along the wall, yielding the shape of the wall along the streamwise direction, as shown in figure 4.7. Figure 4.7 shows that the wall shape before dewarping has a parabolic shape, and after dewarping the shape of the wall is approximately a straight line. However, even after dewarping, the wall is still not parallel with the x-axis but rotated clockwise at an angle of approximately 0.04 degrees due to the before mentioned possible in-plane small angular misalignment between the calibration target and the wind tunnel floor (*i.e.* the flat plate of the ZPG-TBL). Therefore, an additional rotational correction is necessary as part of the dewarping of the PIV images. The final mapping function, which includes the rotation, as well as dewarping is given by equation 4.7, where the mapping function can be either R2 or P3.

$$\begin{bmatrix} \hat{x}_i \\ \hat{y}_i \end{bmatrix} = \begin{bmatrix} \cos(\theta) & -\sin(\theta) \\ \sin(\theta) & \cos(\theta) \end{bmatrix} \times \begin{bmatrix} \hat{x}_{i(mapping\ function)} \\ \hat{y}_{i(mapping\ function)} \end{bmatrix} \tag{4.7}$$

Note that since this equation maps from object space to the image space, the negative value of the angle found in figure 4.7 should be used for the rotation angle θ. The maximum deviation of the measured wall profile from the straight and horizontal position before and after dewarping is summarised in table 4.3.

Table 4.3: The maximum deviation of the measured wall profile from straight and horizontal position before and after dewarping

Condition	Maximum deviation from the horizontal position (px) [μm, l^+]
Distorted	9.00 [260, 6.10]
Dewarped by R2	5.42 [157, 3.67]
Dewarped by R2 and rotated	1.90 [54.9, 1.29]
Dewarped by P3	3.98 [115, 2.70]
Dewarped by P3 and rotated	0.62 [17.9, 0.42]

4.2.1.3 Dewarping of PIV images

The estimated mapping function and rotation angle can now be applied to all of the raw PIV images. For each pixel coordinate in object space, the corresponding coordinate in the image space is calculated using equation 4.7. Since the corresponding coordinates might not be at an exact pixel position, their values are bicubicly interpolated using the nearest sixteen pixels. The calculated image coordinates that lie outside the image are given a zero intensity value.

A section of a PIV image before (*i.e.* raw image) and after dewarping (*i.e.* corrected image) is shown in figure 4.8. Figure 4.8 also shows that a region of 32 $\times$ 8 pixels, corresponding to the final PIV interrogation window size, does not show any deformation after dewarping, even in the corner of the PIV images where the distortion is maximum. Calculations of the mapped coordinates of the interrogation window borders indicates that the maximum deformation of the IW is estimated to be 0.08 pixels, which is comparable to the measurement uncertainty of 2C-2D cross-correlation digital PIV analysis. Therefore, this level of bias error is within the resolving power and experimental uncertainty of 2C-2D cross-correlation digital PIV analysis [84] and is not detectable in the 2C-2D PIV measurement.

The particle shapes and sizes have also been compared before and after dewarping of the single-exposed PIV images with the results given in figure 4.9. Since the particle images have approximately an average diameter of 2 pixels, it is impossible to detect any change in the particle shape from the PIV images. In order to better show the change in the shape of the particles after dewarping, the distorted shape of a two-pixel diameter circle at the position of maximum distortion is calculated analytically using the dewarping functions. These are the results presented in figure 4.9, which shows that the change in the size of the particles is less than 2%. Therefore, it is expected that the difference between the cross-correlation function shape will be insignificant between 2C-2D cross-correlation digital PIV analysis based on the raw single-exposed PIV images and the dewarped single-exposed PIV images and hence, on the uncertainty of the PIV measurement. Furthermore, pixel-locking behaviour [153] might be affected by the distortion as the particle size is slightly changed. However, since the shape and size of the particles in the single-exposed PIV images does not change significantly between the raw and dewarped single-exposed PIV images, the dewarping process does not result in any additional pixel locking in the PIV measurement as demonstrated by the results shown in figure 4.10, which shows the histograms of the sub-pixel displacement based on 2C-2D cross-correlation digital PIV analysis based on raw and dewarped single-exposed PIV images, indicating that pixel locking is minimal in both cases.

Based on these findings, it is reasonable to assume that the velocity vector measurement will not change between 2C-2D cross-correlation digital PIV analysis based on the raw single-exposed PIV images and those based on the dewarped single-exposed PIV images within the experimental uncertainty of 2C-2D cross-correlation digital PIV. However, the positions of the velocity vector measurements need to be corrected to account for optical distortion. Based on this conclusion, an alternative approach that avoids the

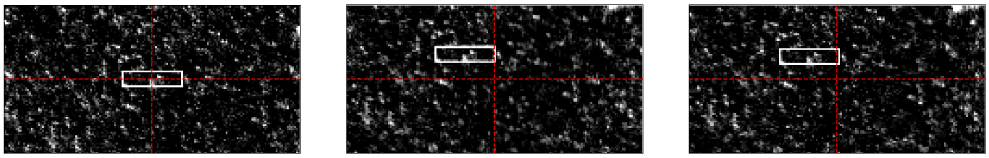

(a) (b) (c)

Figure 4.8: A section of: (a) the distorted image, (b) the corrected image using R2 model and (c) the corrected image using P3 model. The sections are taken where the distortion is maximum in the full image, and an interrogation window is shown as the white box in all three figures. The red dashed line marks the origin of the image section. Note the interrogation window doesn't change its shape before and after distortion correction, but is only shifted.

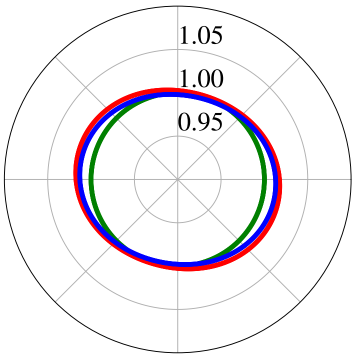

Figure 4.9: Shape of the distorted particle with a diameter of 2 pixels located at the position of maximum distortion, calculated using the R2 and P3 mapping functions. —: The shape of the correct particle. —: The shape of the distorted particle using the R2 dewarping function. —: The shape of the distorted particle using the P3 dewarping function. Note that the difference between the corrected and distorted particle shapes has been exaggerated.

computationally expensive dewarping process of the raw single-exposed PIV images is proposed. In this alternative approach, the velocity vectors are determined using 2C-2D cross-correlation digital PIV analysis of the raw (*i.e.* distorted) single-exposed PIV images. This is then followed by correcting the spatial position of the centre of the PIV interrogation window using the mapping function determined through the image calibration. The two methods available to yield corrected velocity fields using the mapping functions determined through calibration are described in the flow charts shown in figure 4.11, with the former labelled as Method I and named as dewarping the images prior to PIV analysis, while the latter is labelled Method II and named as correcting the velocity field after PIV analysis on the raw (*i.e.* distorted) images. The results of these two approaches are compared in section 4.2.3.

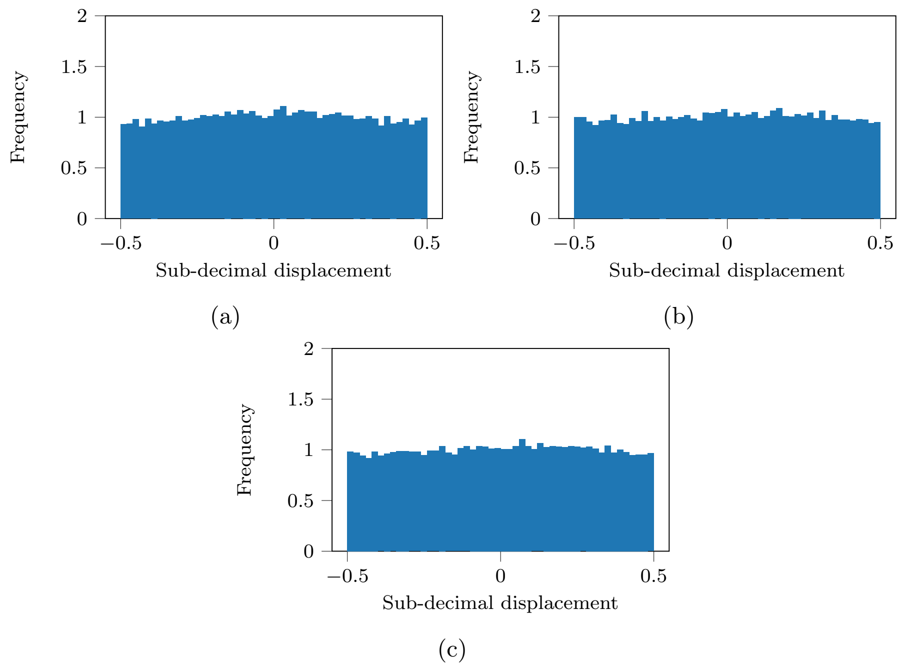

Figure 4.10: Probability density functions of the sub-pixel residual displacement of 2C-2D cross-correlation digital PIV of: (a) calculated using distorted images, (b) calculated from the dewarped images using the R2 model (c) calculated from the dewarped images using the P3 model.

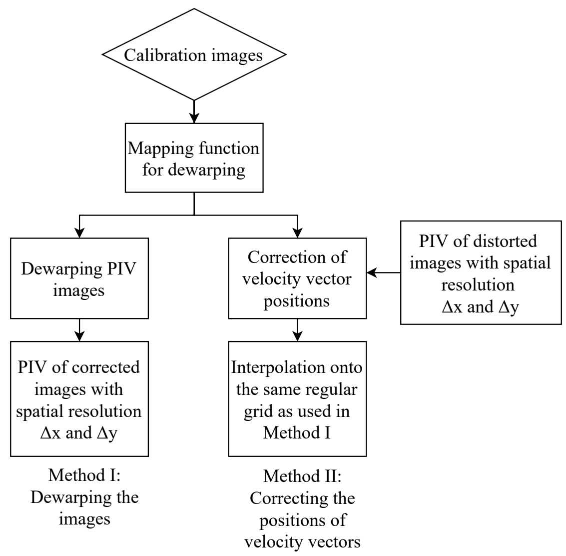

Figure 4.11: Flowcharts describing the two methods implemented for image dewarping: Method I – dewarping the images before performing PIV analysis and Method II – dewarping the velocity field after PIV analysis of the raw (*i.e.* distorted) images.

4.2.2 Sensitivity analysis of the mapping functions

Monte Carlo simulations have been used to investigate the uncertainty in the mapping functions and their sensitivity to the change in object and image spaces within their corresponding uncertainties. The uncertainty in the coefficients is a result of the mapping function parameter estimation. The procedure of the Monte Carlo simulations is as follows:

1. Generate sample spaces $\{\hat{P}_I\}_n$ and $\{\hat{P}_O\}_n$ as N sets of 91 positions of the markers, distributed with an average of zero pixels from the measured position and a standard deviation equivalent to the measurement standard uncertainty.
2. For each set in the sample space, compute the sample mapping functions $(f_x, f_y)_n$
3. Compute the residual error after dewarping for each marker j in each set, *i.e.* $\epsilon_{j_n} = L_{ref}\left(\hat{P}_{In} - \left(f_x(\hat{P}_O), f_y(\hat{P}_O)\right)\right)_n$
4. Repeat steps (1) to (3) to generate an error sample space of size N.
5. Using the error sample space of size N from step (4), compute the joint probability distribution functions (JPDFs), ϵ_j for each of the 91 markers.

The JPDFs of ϵ_j using a sample size $N = 500,000$ are given in figure 4.12 for the R2 and P3 mapping functions. These results show that with 95% confidence the residual error using R2 at all marker locations except one is within two pixels, which is less than 0.02% of the length of the sensor. The uncertainty of the mapping using P3 is slightly better than that for R2, as its residual error is less for most marker locations. Hence, the computed mapping functions can be applied to correct the image distortion introduced into 2C-2D single-exposed PIV images due to the usage of large sensors, since a statistically insignificant additional uncertainty is introduced into the dewarping correction due to measurement uncertainty of the object and image marker positions, when their determination is within the uncertainties specified in table 4.2.

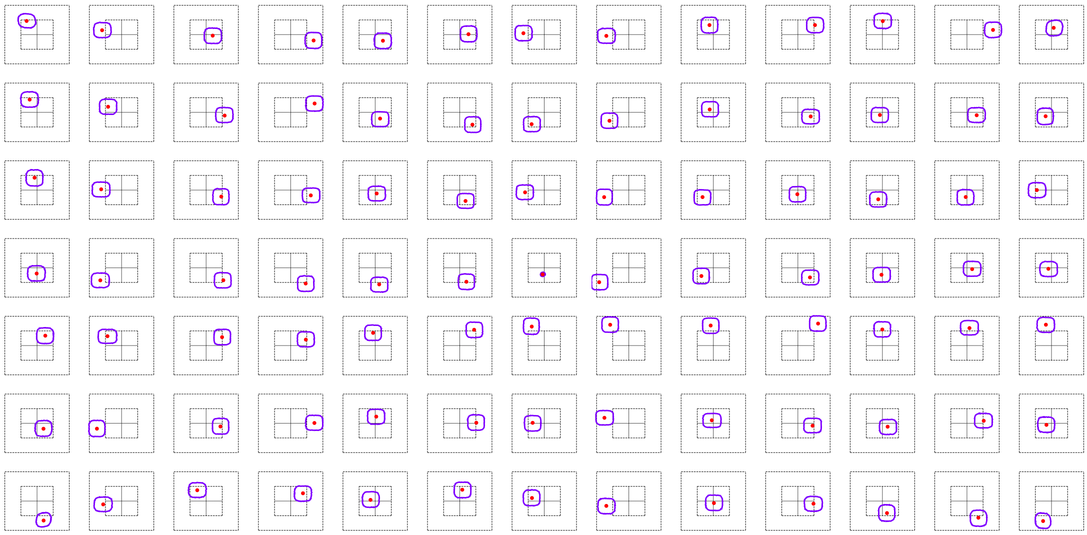

(a)

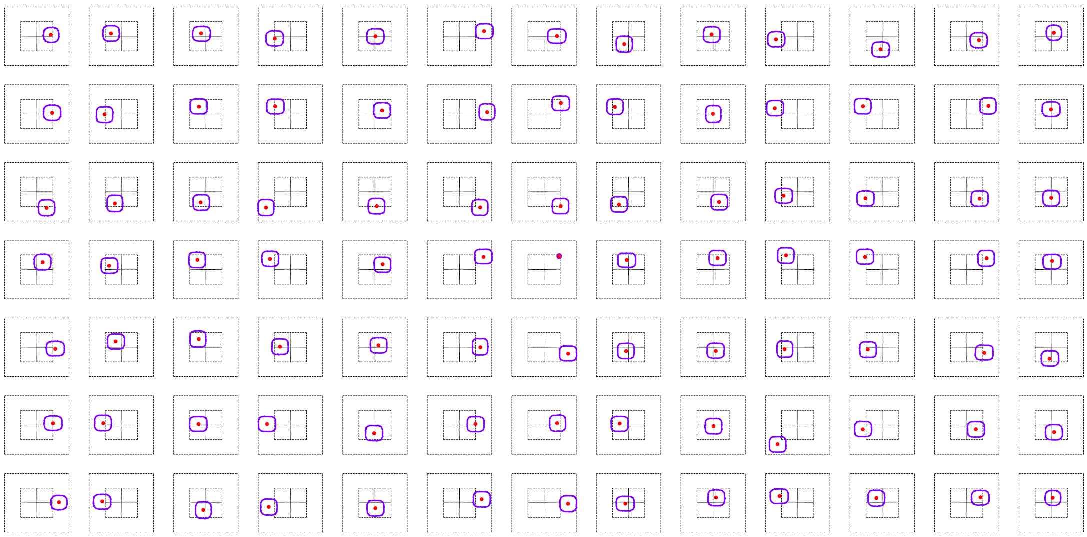

(b)

Figure 4.12: Results of the sensitivity analysis showing the joint JPDFs of the residual error of the mapping functions at the locations of the calibration markers for: (a) R2 mapping function (b) P3 mapping function. See (c) for the nomenclature of the JPDFs.

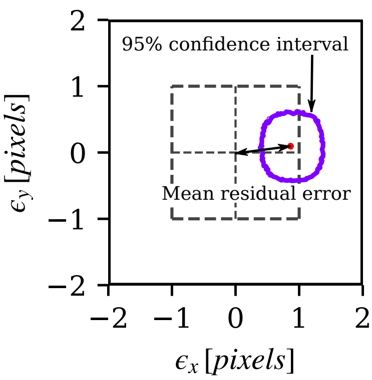

(c)

4.2.3 Image distortion correction results

In order to assess how lens distortion affects 2C-2D PIV measurements, and ascertain the appropriateness and perfromance of the two image dewarping models, as well as the two approaches depicted in figure 4.11 to correct for lens distortion of single-exposed PIV images, the first- and second-order statistics of the velocity field of the ZPG-TBL are presented and compared with those measured in the same facility under similar flow condition in a previous experimental campaign (EuHIT experiment) [138], as well as first- and second-order statistics of the velocity field of a ZPG-TBL DNS with $Re_\theta = 6,500$ [154]. The PIV data provided from the EuHIT database was processed using an interrogation window size of $20^+ \times 5^+$ in the streamwise and wall-normal directions for $y < 5mm$ with the superscript $^+$ denoting viscous units. Thus, the spatial resolution is similar to the data presented in this paper. However, since the sensor used in the EuHIT measurement is only 35% of the size of the sensor used in the presented study and a Zeiss 300 mm/f2.8 telephoto lens is used, therefore the lens distortion in the EuHIT data set is minimal. Assuming lens distortion to be the same for both experiments, the estimated error introduced by lens distortion is about 0.2%. For $y > 5mm$ the velocity fields were measured using SPIV, which includes correction for any image distortion through the SPIV image calibration process. So, the first- and second-order statistics profiles provided from the EuHIT experiment are deemed to be image distortion-free, and are used as a baseline to estimate the accuracy of the image dewarpping methods presented in this paper.

The boundary layer characteristics calculated from the mean profile based on dewarped 2C-2D PIV analysis presented in table 4.4 compare favourably with the boundary layer statistics measured in the EuHIT experiment. The mean streamwise velocity profiles are given and compared in figure 4.13. These results show that, in the wall region, the mean streamwise velocity profile measured based on the raw distorted images deviates from the EuHIT profile with a maximum difference of as much as 80%, clearly illustrating that lens distortion leads to significant errors in these measurements and must be corrected. The maximum deviation of the profile is near the wall, which is near the edge of the image where lens distortion is a maximum.

Table 4.4: Turbulent boundary layer characteristics compared with EuHIT experiment [138]

	U_∞ (m/s)	δ_{99} (mm)	u_τ (m/s)	Re_τ
Current experiment	9.64	103	0.348	2,386
EuHIT	9.64	104	0.346	2,360

The profile determined from 2C-2D PIV based on the dewarped images using the R2 mapping function starts to deviate from the EuHIT data for $y^+ < 7$, with the maximum difference compared to the EuHIT measurements remaining similar to that determined using the raw distorted images. The application of the P3 mapping function to dewarp the raw PIV images prior to 2C-2D cross-correlation digital PIV analysis or position correction after 2C-2D cross-correlation digital PIV analysis of raw PIV images yields mean streamwise velocity profiles that are in agreement with both the EuHIT measurements, as well as the more highly resolved DNS data, which is also shown for comparison. This clearly indicates that most of the lens distortion can be corrected with a suitable image dewarping mapping function. Furthermore, these results also show that there is no significant difference between the mean velocity profiles resulting from the two distortion correction approaches depicted in figure 4.11.

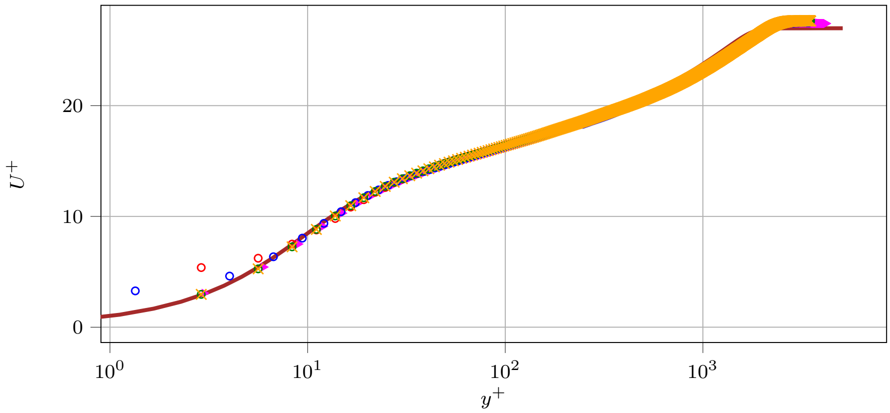

Figure 4.13: Mean streamwise velocity profile in wall units. The profile is compared with an experimental data taken in similar flow conditions (EuHIT Experiment) [138], as well as DNS simulation with $Re_\theta = 6500$ [154] —: DNS. ◀: EuHIT. ○: Distorted. ○: Corrected using Method I, R2 model. ○: Corrected using Method I, P3 model. ×: Corrected using Method II, P3 model

The measured Reynolds stress profiles are presented in figure 4.14 and compared with the profiles from the EuHIT experiment as well as the highly resolved DNS data. These results show that dewarping does not affect the $\overline{u'v'}^+$ and $\overline{v'v'}^+$ profiles as much as the $\overline{u'u'}^+$ profile. However, the profiles based on the raw distorted PIV images are slightly lower than the profiles based on the dewarped PIV images. The $\overline{u'u'}^+$ profile based on the raw PIV images is up to 12% lower than the profile from the EuHIT experiment with the peak slightly shifted to a higher y^+ value. The difference in the profile is largely corrected by employing the R2 mapping function in the PIV image dewarping. The profile based on PIV images dewarped using the P3 dewarping model corrects all the lens distortion with the results agreeing well with the previous EuHIT experiment measurements. Once again, the profiles of the second order statistics produced using the dewarping Method I and Method II shown in figure 4.11 agree with each other within experimental uncertainty.

The results show that Method I and Method II to correct lens distortion in 2C-2D PIV provide similar precision and uncertainty as far as the first and second order velocity statistics are concerned. However, Method II is more computationally efficient compared to Method I, so Method II is the recommended approach to correcting lens distortions in 2C-2D PIV.

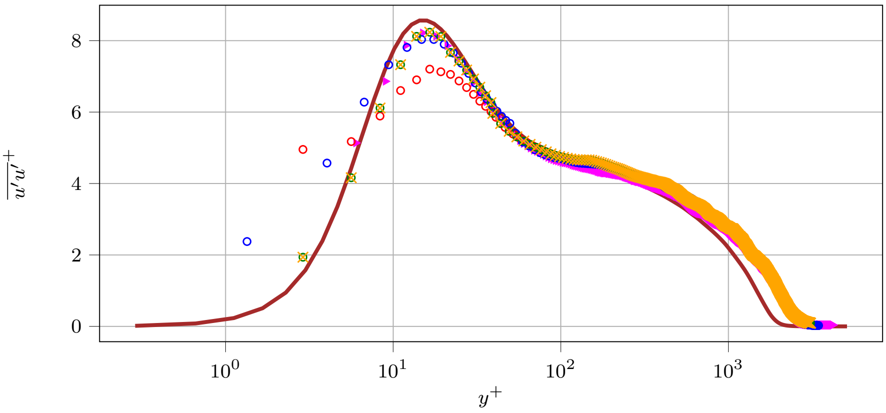

(a)

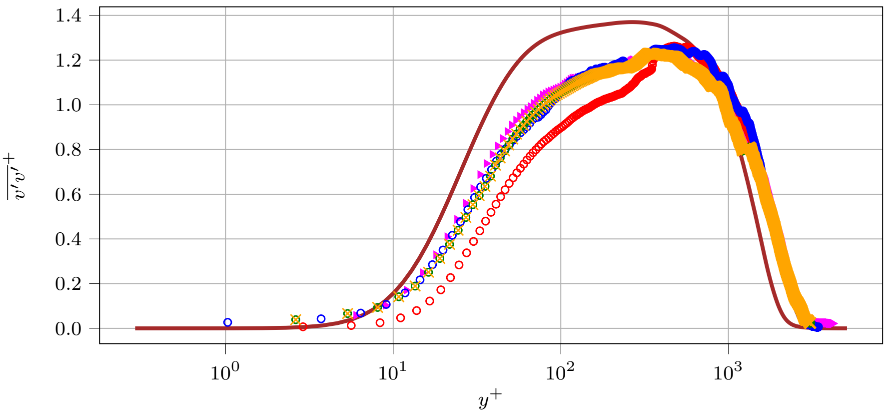

(b)

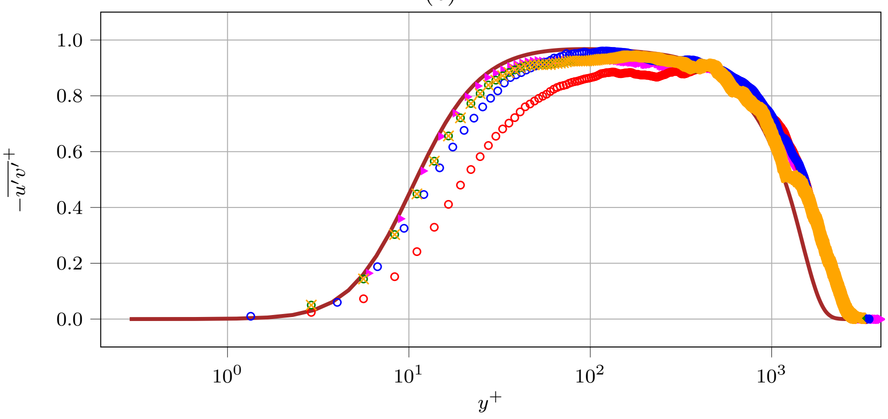

(c)

Figure 4.14: (a) Streamwise Reynolds stress profile ($\overline{u'u'}^+$), (b) wall-normal Reynolds stress profile ($\overline{v'v'}^+$) and (c) Reynolds shear stress profile ($-\overline{u'v'}^+$) The profiles are compared with experimental data taken under similar flow conditions (EuHIT Experiment) [138], as well as a DNS simulation with $Re_\theta = 6500$ [154] —: DNS. ◀: EuHIT. ○: Distorted. ○: Corrected using Method I, R2 model. ○: Corrected using Method I, P3 model. ×: Corrected using Method II, P3 model

4.3 POD analysis using 2C-2D PIV data

This section discusses the process of the POD analysis is using the 2C-2D PIV velocity fields and the convergence of the POD analysis. The key idea of POD is to decompose the input fields into a linear combination of eigenvectors which attempts to contain as much energy of the input as possible in each eigenvector, with those eigenvectors called the POD modes. Therefore, although the size, strength and time persistence of individual flow structures vary in the turbulent flow, there will be a correlation between the same type of flow structure, which can be identified by POD. Lumley [140] explored this idea and was the first to apply this technique to identify coherent structures in the turbulent shear flows. The POD method has since been widely used to study different flow structures [155–158], such as large scale motions in the wall-bounded turbulent flows [159]. Large scale motions in the wall-bounded turbulent flows are spatially long and wide flow structures that are up to 3 δ in size in the streamwise direction and nearly occupy the entire boundary layer thickness in the wall normal direction [160]. Because other flow structures co-exist and overlap with the large scale motions, they are difficult to identify directly from the velocity fields. However, because of their high contribution to the fluctuating velocity and relative invariance in time, they can be easily separated from the rest of the flow structures using POD, and are typically represented by the most energetic POD mode.

In section 4.3.1, the theoretical background of the classic POD and snapshot POD methods are introduced. Section 4.3.2 will apply the POD method to the 2C-2D velocity fields, with section 4.3.3 presents a study of the convergence of the POD modes.

4.3.1 Proper orthogonal decomposition

In this study, the POD is applied to the 2C-2D fluctuating velocity fields, so considering the following fields,

$$\mathbf{u}(x,y,t) = \begin{bmatrix} u'(x,y,t) \\ v'(x,y,t) \end{bmatrix} \tag{4.8}$$

where (x, y) is the coordinate of the measurements, and t represents the statistically independent velocity fields produced at different times, also called snapshots. Note that although different snapshots are usually produced by measuring the flow at different times, the POD result does not depend on the acquisition order or time interval between the snapshots.

A POD snapshot vector can then be produced by flattening the $u(x, y, t)$ and $v(x, y, t)$ fields and concatenating them into a single one-dimensional vector. The data set for POD analysis is constructed by stacking the POD snapshot vectors into a matrix, as follows.

$$\mathbf{X} = \begin{bmatrix} u(1,1,1) & \dots & u(N_x, N_y, 1) & v(1,1,1) & \dots & v(N_x, N_y, 1) \\ u(1,1,2) & \dots & u(N_x, N_y, 2) & v(1,1,2) & \dots & v(N_x, N_y, 2) \\ \vdots & & \vdots & \vdots & & \vdots \\ u(1,1,N_t) & \dots & u(N_x, N_y, N_t) & v(1,1,N_t) & \dots & v(N_x, N_y, N_t) \end{bmatrix} \tag{4.9}$$

The order of flattening the $u(x, y, t)$ and $v(x, y, t)$ fields does not affect the POD result, as long as the resultant POD modes are unflattened in the same way. If the POD method is applied to higher dimensional data with more variables, the POD snapshot vector and the data matrix $\mathbf{X}$ can be constructed in a similar way.

The aim of POD is to use the velocity data matrix $\mathbf{X}$ to find a decomposition of $\mathbf{u}(x, y, t)$ in the form of

$$\mathbf{u}(x, y, t) = \sum_{j=1}^{N} a_j(t)\phi_j(x, y), \tag{4.10}$$

to capture as much energy as possible by a minimal number of orthogonal POD modes $\phi_j(x, y)$. Traditional POD method solves this problem by performing the eigenvalue decomposition on the covariance matrix of $\mathbf{X}^T$, as following,

$$\mathbf{R}_{\text{Traditional}}\phi_j = \lambda_j\phi_j \tag{4.11}$$

where $\mathbf{R}_{\text{Traditional}} = \mathbf{X}\mathbf{X}^T$ and λ_j is the eigenvalue of the j^{th} POD mode, representing the kinetic energy captured. Because the size of the velocity data matrix $\mathbf{X}$ is $(2 \times N_x \times N_y) \times N_t$, the size of $\mathbf{R}_{Traditional}$ is $(2 \times N_x \times N_y)^2$. In a typical experiment $N_t \ll (2 \times N_x \times N_y)$, which indicates that the size of the covariance matrix can be reduced by defining $\mathbf{R}_{\text{Snapshot}} = \mathbf{X}^T\mathbf{X}$, which has a size of $N_t^2 \ll (2 \times N_x \times N_y)^2$. This was first recognised by Sirovich [161] and is used in the snapshot POD method. The eigenvalue decomposition using $\mathbf{R}_{Snapshot}$ results in the same eigenvalues as the classical method, with the POD modes calculated from the eigenvectors,ψ_j, as follows,

$$\phi_j = \mathbf{X}\boldsymbol{\psi}_j\frac{1}{\sqrt{\lambda_j}} \tag{4.12}$$

Equation 4.12 can also be written as,

$$\mathbf{X} = \mathbf{\Phi}\mathbf{\Sigma}\mathbf{\Psi}^T \tag{4.13}$$

where $\mathbf{\Phi} = [\boldsymbol{\phi}_1\ \boldsymbol{\phi}_2\ \ldots\ \boldsymbol{\phi}_{N_t}]$ contains the POD modes, $\mathbf{\Psi} = [\boldsymbol{\psi}_1\ \boldsymbol{\psi}_2\ \ldots\ \boldsymbol{\psi}_{N_t}]$ contains the time coefficients, and the diagonal of $\mathbf{\Sigma}$ contains the square root of the eigenvalues. Equation 4.13 has the same form as the singular value decomposition of $\mathbf{X}$. Thus, using the snapshot POD method the POD modes can be calculated directly from the singular value decomposition of the data matrix $\mathbf{X}$.

4.3.2 Decomposed modes from velocity fields

The eigenvalues of the POD modes and their accumulated sum is presented in the figure 4.15. These results show that the first mode contains 12% of the total energy in the flow, whereas the first 18 modes can recover 50% of the total energy in the flow. The slow convergence rate of the POD modes is an indicative of the complex multi-scale behaviour of the turbulent boundary layer flow.

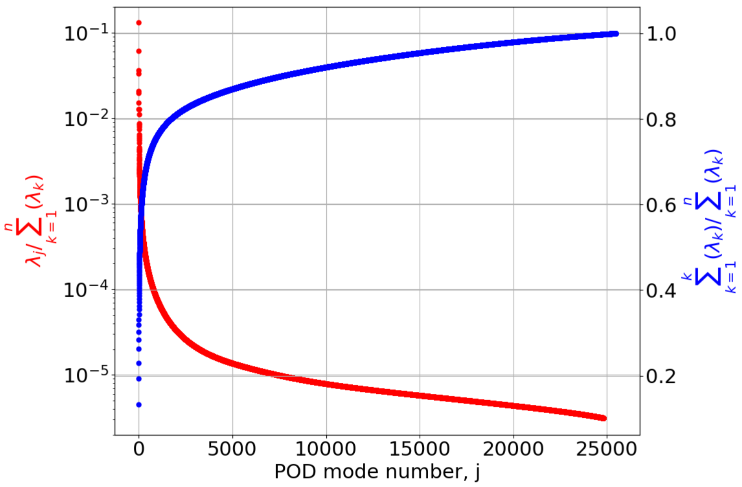

Figure 4.15: Eigenvalues of the POD modes and their cumulative sum as a fraction of the total energy of all modes.

The first ten most energetic POD modes are shown in the figure 4.16. The most energetic mode shown in figure 4.16a presents a single flow structure that occupies nearly the entire boundary layer, with a stream-wise extent that is indicated to be larger than one boundary layer thickness, so it is identified to be the large scale motion. These results show that as the mode number increases, the scales of the flow structure becomes smaller, and its contribution to the total turbulent kinetic energy of the flow decreases.

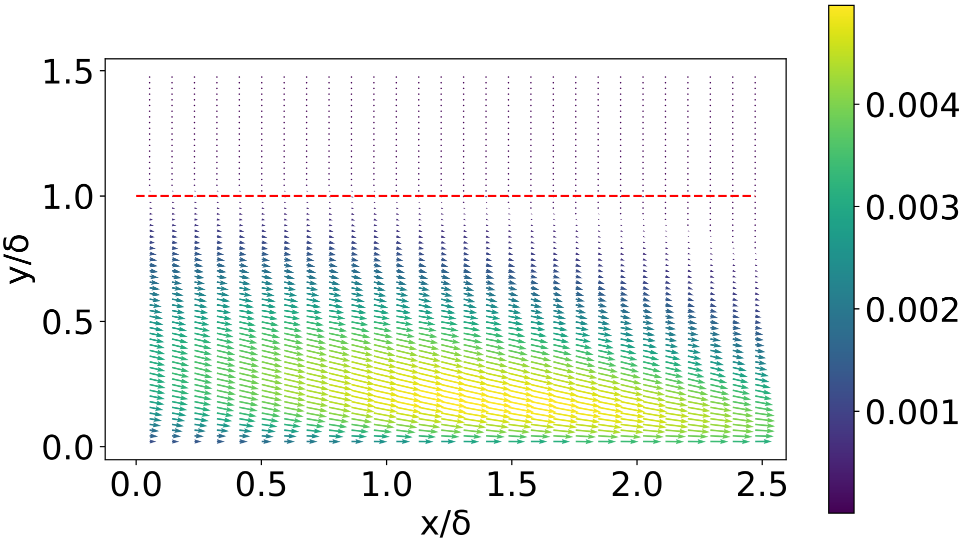
1.5
1.0
0.5
0.0
y/δ
0.0 0.5 1.0 1.5 2.0 2.5
x/δ
0.004
0.003
0.002
0.001

(a)

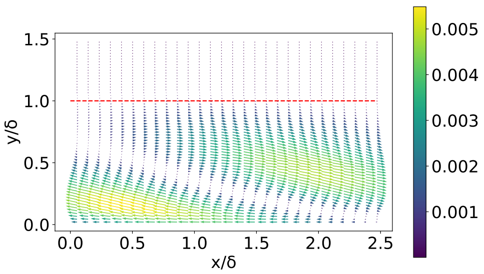
1.5
1.0
0.5
0.0
y/δ
0.0 0.5 1.0 1.5 2.0 2.5
x/δ
0.005
0.004
0.003
0.002
0.001

(b)

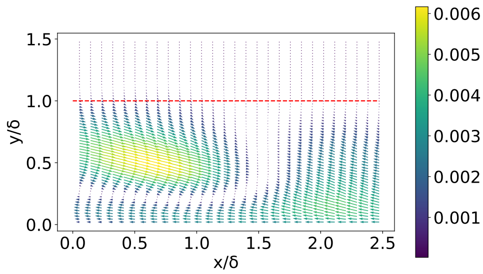
1.5
1.0
0.5
0.0
y/δ
0.0 0.5 1.0 1.5 2.0 2.5
x/δ
0.006
0.005
0.004
0.003
0.002
0.001

(c)

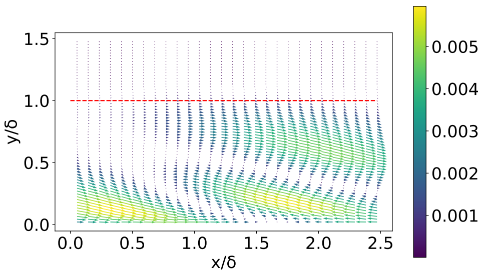
1.5
1.0
0.5
0.0
y/δ
0.0 0.5 1.0 1.5 2.0 2.5
x/δ
0.005
0.004
0.003
0.002
0.001

(d)

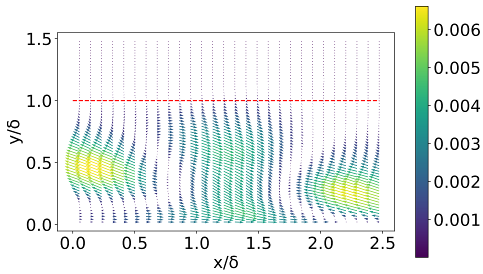
1.5
1.0
0.5
0.0
y/δ
0.0 0.5 1.0 1.5 2.0 2.5
x/δ
0.006
0.005
0.004
0.003
0.002
0.001

(e)

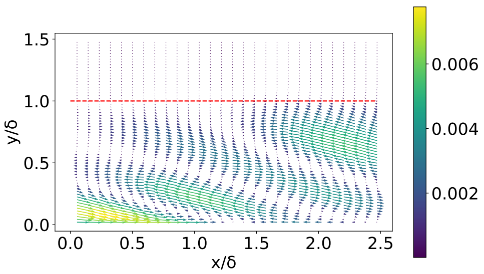
1.5
1.0
0.5
0.0
y/δ
0.0 0.5 1.0 1.5 2.0 2.5
x/δ
0.006
0.004
0.002

(f)

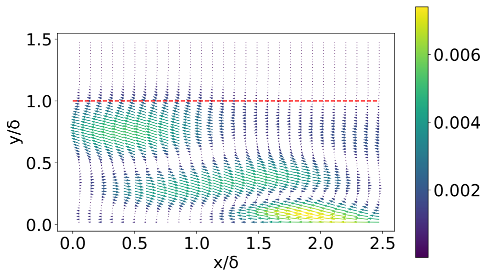
1.5
1.0
0.5
0.0
y/δ
0.0 0.5 1.0 1.5 2.0 2.5
x/δ
0.006
0.004
0.002

(g)

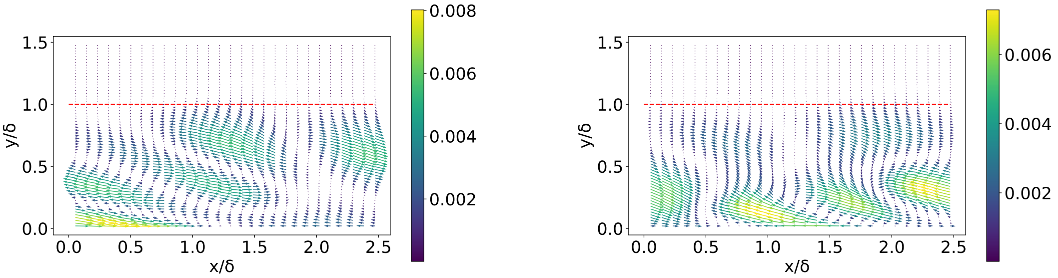

(h) (i)

Figure 4.16: Velocity fluctuation vector plot of the first nine most energetic POD modes. The colour bar and the colour of the vectors represent the velocity fluctuation magnitude. The red dashed line represents the boundary layer thickness.

4.3.3 Mode convergence of proper orthogonal decomposition

Since POD is a purely data-driven process, the calculated POD modes and eigenvalues only reflect the true physics with a small uncertainty if sufficient snapshots are provided to be representative of the physical phenomenon. The POD analysis is deemed to have converged, when the POD modes and eigenvalues no longer change due to the addition of further snapshots. Therefore, the study of the rate of convergence of the POD analysis and to determine the requirement of the number of snapshots for convergence, was performed. N_s sets of randomly chosen snapshots from the measurement of the same flow were chosen for the POD analysis. The statistics of the eigenvalues of the POD analysis was computed from these samples.

Five cases of POD analysis with different numbers of snapshots are presented. The number of snapshots, N_s, used for each case, as well as the number of repetition, N_R, per velocity snapshot matrix size to calculate the statistics of the eigenvalues, are summarised in table 4.7.

Table 4.7: The size of POD analysis and the repetition of analysis performed to calculate the statistics of POD mode convergence

Case number	Number of snapshots used for POD analysis, N_s	Repetitions to calculate eigenvalue statistics, N_R
1	2,500	5,000
2	5,000	3,000
3	7,500	1,000
4	12,500	1,000
5	20,000	1,000

The averaged eigenvalues calculated using different snapshots and their accumulated sum are shown in figure 4.17. From the normalised mean eigenvalue plot, the most energetic mode contains about 13% of the total kinetic energy in the flow, and the profiles of eigenvalues calculated from different cases collapse up to the 30$^{\text{th}}$ mode, which has a normalised eigenvalue of 0.003, i.e. 0.3% of the total TKE. For the less energetic modes, more snapshots used in the analysis result in a lower eigenvalue, but the difference between the profile calculated using 20,000 snapshots and all snapshots is less than 10^{-6}, suggesting nearly all modes in the physical system can be resolved using the available snapshots. From the normalised mean eigenvalue plot, the first 30 modes contain 46% of TKE, with a collapse of the profiles from different cases.

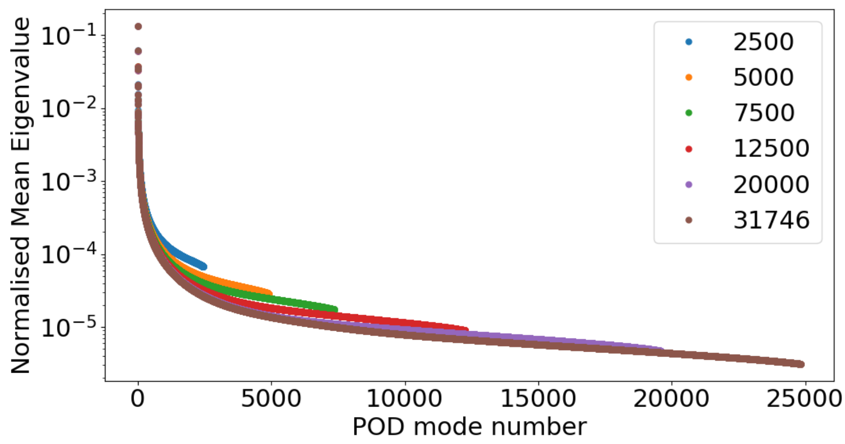

(a)

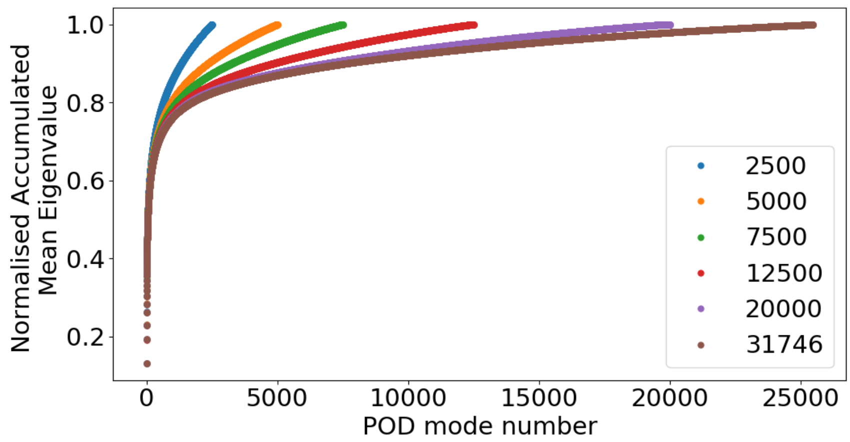

(b)

Figure 4.17: a) Averaged eigenvalue in each case normalised by the sum of averaged eigenvalue. Eigenvalues calculated from all snapshots available (31,746 snapshot) are also included for reference. b) Accumulated sum of the eigenvalues shown in a). The figures are truncated at mode number 25,000 for clarity.

Although the mean eigenvalue profile is similar for different cases, the standard deviation of the eigenvalues differs with the number of snapshots used, as shown in figure 4.18.

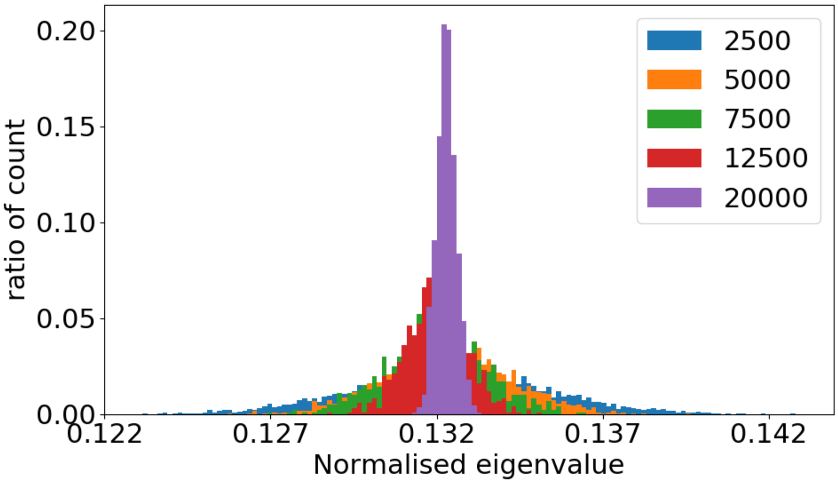

(a)

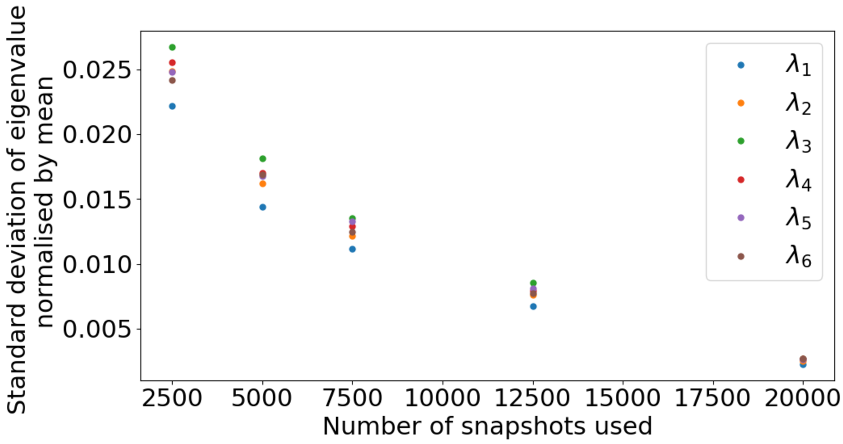

(b)

Figure 4.18: a) Distribution of the first eigenvalue as a function of the number of snapshots used for POD analysis b) The standard deviation of the first 6 eigenvalues normalised by the averaged eigenvalues for different number of snapshot used for POD analysis.

These results show that the distribution of the eigenvalues is approximately Gaussian for all the cases, with a peak that narrows as more snapshots are used, which is indicative of the convergence of the POD analysis. In addition, figure 4.18b shows that the first six eigenvalues converge at a similar rate, with the first eigenvalue converging slightly faster than other eigenvalues. In order to reach a standard deviation of less than 1% of the mean eigenvalues, at least 10,000 snapshots are required for the POD analysis.

4.4 Contribution of large scale motion to skin friction

In this section, the contribution of the large scale motions to the turbulent generation term in the RD decomposition of the skin friction is analysed using conditional statistics. Section 4.4.1 presents the theoretical background of the Renard-Deck decomposition of the skin friction coefficient and the physical interpretation of the decomposed terms. Section 4.4.2 presents the turbulent production term of the RD-decomposition calculated from the large-scale motion dominated snapshots to study how LSM contributes to that term.

4.4.1 Renard-Deck decomposition

Renard and Deck [141] present a decomposition (RD decomposition) of the skin friction coefficient based on the mean kinetic energy budget of the fluid motion in an absolute frame of reference. The decomposition is given by

$$\begin{aligned} C_f = & \underbrace{\frac{2}{U_e^3}\int_0^\infty \mu \left(\frac{\partial U}{\partial y}\right)^2 dy}_{C_{fa}} + \underbrace{\frac{2}{U_e^3}\int_0^\infty -\langle u'v'\rangle \frac{\partial U}{\partial y} dy}_{C_{f_b}} \\ & + \underbrace{\frac{2}{U_e^3}\int_0^\infty (U-U_e)\frac{\partial}{\partial y}\left(\frac{\tau}{\rho}\right) dy}_{C_{f_c}} \end{aligned}, \tag{4.14}$$

where

$$\tau = \mu\left(\frac{\partial U}{\partial y}\right) - \langle u'v'\rangle. \tag{4.15}$$

The frame of reference travels at the same rate as the free-stream undisturbed flow, U_0, thus the undisturbed flow will appear to be stationary. The only assumption made when deriving this equation is that the instantaneous streamwise velocity is zero at the wall, which allows blowing or suction at the wall. However, neither blowing nor suction is present in the flow studied. The RD decomposition decomposes the skin friction into physically interpretable terms that are local at each streamwise position. The first term, C_{f_a} represents the viscous dissipation of the mean streamwise kinetic energy, the second term, C_{f_b}, represents the production of the turbulent kinetic energy from the mean streamwise kinetic energy and the last term, C_{f_c}, accounts for the growth of the boundary layer effect.

4.4.2 Conditional statistics of the turbulent production term in the RD decomposition

As shown in figure 4.16a, nearly all non-zero velocity vectors in the LSM have a positive fluctuating streamwise velocity and a negative fluctuating wall normal velocity. Therefore, the presence of LSM will have a strong association with the Reynolds shear stress $\langle u'v' \rangle$. The viscous dissipation term, C_{f_a}, of the RD decomposition depends only on the mean values of the fluid field and has no contribution from the turbulence, and hence the LSMs. The boundary layer grows slowly in a ZPG-TBL, hence, the boundary layer growth term, C_{f_c}, is negligible. Therefore, only Reynolds stress term, C_{f_b}, is important with respect to the turbulence, and hence the LSMs dependent, and is the term of relevance to turbulence and the effect of coherent structures. So this term is the subject of subsequent analysis.

LSM dominated velocity field snapshots are identified using the time coefficient of the first POD mode, ϕ_1, presented in figure 4.19. The distribution is Gaussian-like, and since all the velocity vectors of the first POD mode are positive in the stream-wise direction, a positive time coefficient corresponds to a high-momentum LSM, where the instantaneous velocity of the flow structure is higher than the mean velocity, and a negative time coefficient corresponds a low-momentum LSM. Furthermore, the absolute value of the time coefficient represents the strength of LSM present in that snapshot. Therefore, the following criterion is used to determine that a snapshot is LSM dominated,

$$\left|\phi_{1,n}\right| > K\sigma_{\phi_1}, \tag{4.16}$$

where $\phi_{1,n}$ represents the time coefficient of the first POD mode for snapshot n, and σ_{ϕ_1} represents the standard deviation of the time coefficient for all the snapshots. A higher K value represents a tighter selection criterion, yielding the selection of the snapshots with higher LSM strength.

In this study, a number of K values: 0.5, 1, 1.5, 2, 2.5 are used to perform the study of the sensitivity analysis of the Reynolds stress term to K. The number of snapshots available for each K value is summarised in table 4.8.

The proportion of C_{f_b} in the the skin friction coefficient (C_{f_b}/C_f) is given as a function of x position in figure 4.20. C_f is calculated from the gradient of the mean stream-wise velocity profile at the wall, and the proportion of C_{f_a} is plotted for comparison. This results show that LSM dominated snapshots results in an increase of C_{f_b}, indicating that the LSMs are a significant contributor to the turbulent production term in the RD decomposition of the skin friction.

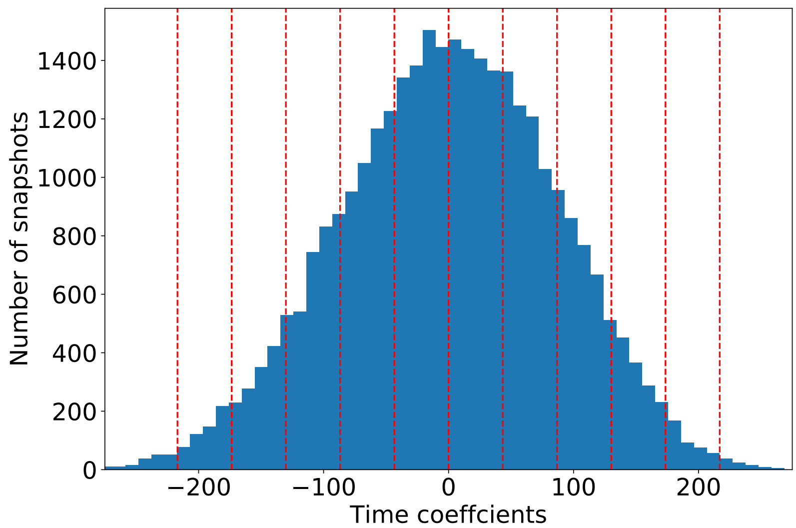

Figure 4.19: Distribution of the time coefficient of the first POD modes. The red dashed line represents the positions of $\pm 2.5\sigma$, $\pm 2\sigma$, $\pm 1.5\sigma$, $\pm\sigma$, $\pm 0.5\sigma$ and the mean value.

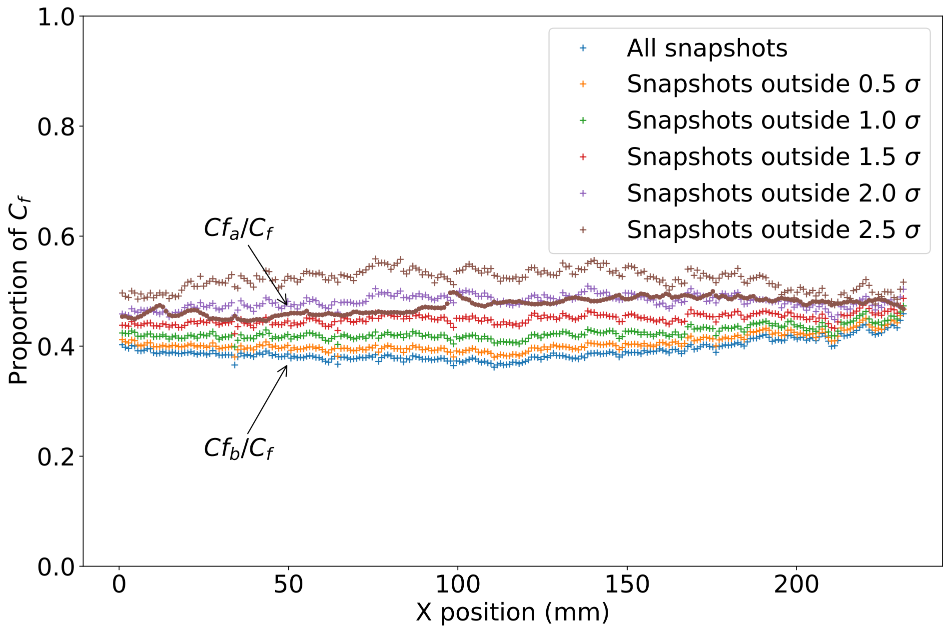

Figure 4.20: Proportions of C_{f_a} and C_{f_b} of the total wall friction C_f for different K values

Table 4.8: The number of snapshots for each K value when calculating the conditional statistics

K value	Number of snapshots
0.5	24,513
1	17,825
1.5	12,148
2	7,662
2.5	4,387

Also shown in the figure 4.20, the sum of C_{f_a} and C_{f_b} terms only account for about 90% of the total wall skin friction coefficient measured. One possible reason is that the $\langle u'v' \rangle$ term determined from the PIV experiment is lower than the real value because of the spatial averaging within the interrogation windows, leading to an underestimate of the C_{f_b} term. Another possible explanation is that the C_{f_c} term, even though much smaller than the rest two terms, also has some contribution to the total wall skin friction. Because two differentiation operations are required to calculate the C_{f_c} term, the measured velocity fields are too noisy to produce an accurate estimation with low uncertainty to establish its significance.

Chapter 5

Conclusion

The key methods and findings of this thesis are summarised as follows:

- A novel 4D-DHPIV/PTV method is described which, in addition to including the standard digital hologram reconstruction, incorporates advanced digital filtering to remove the virtual image effect, 3-dimensional volume deconvolution to reduce the depth-of-focus problem and the virtual image, followed by an efficient one-pass 3-dimensional clustering algorithm coupled with a predictive inverse reconstruction approach to increase the particle reconstruction dynamic range and 3-dimensional reconstruction domain, which is accelerated using particle position prediction.

  – The uncertainty of this method is studies through simulated holograms, and how particle concentration, as well as shot noise present in the hologram, affect the measurement uncertainty is explored. The result shows that 4D-DHPIV/PTV can detect 70% of all particles even for high particle concentration, whereas the direct method at the lowest concentration detects at best 35% of all particles. The bias error does not exceed 0.25 λ in the in-plane direction, while it stays under 1.5 λ in the out-of-plane direction. Standard uncertainty does not exceed 3.5 λ in the in-plane direction, and 8 λ in the out-of-plane direction for all but the highest concentration case, where the standard uncertainty in the out-of-plane direction is around 12 λ. In addition, the shot noise in the hologram does not affect the detection rate of the particles as long as the SNR is higher than 10. The detection rate of the iterative method is about 90%, compared to 50% for the direct method. The bias error increases from 0.2 λ to 0.5 λ for in-plane direction and from 0.1 λ to 1.8 λ for out-of-plane direction as noise is added to the hologram. The standard uncertainty remains between 2 λ – 3 λ for the in-plane direction for all noisy images, but the standard uncertainty in the out-of-plane increases from 6 λ in the noise-free case to 10 λ in the lowest signal to noise ratio of 5 dB.

  - The ability of the 4D-DHPIV/PTV method to measure flow field is demonstrated in a micro-channel measurement, which required the development of a more accurate particle model for phase-changing particles used in water-based experiments. The measurement error due to the different refractive index along the optical path was also corrected. The experiment illustrates that with the 4D-DHPIV/PTV method, the velocity in the channel can be measured with a standard uncertainty of 0.38%, 0.93% and 0.85% of the maximum stream-wise velocity in x, y and z directions, respectively.

- This thesis presents high-resolution 2C-2D PIV measurement of a zero-pressure-gradient turbulent boundary layer. The experiment incorporates a large size sensor with 47 MPx to achieve a final interrogation window size of the measurement is 21.7 wall units in stream-wise direction and 5.42 in wall-normal direction, while covering a field of view of 2.5 boundary layer thickness in stream-wise direction and 1.5 boundary layer thickness in wall-normal direction.

  - In the process of analysing the PIV image acquired in the 2C-2D PIV measurement, the problem of lens distortion is identified. In order to correct the lens distortion, a classical image dewarping method is implemented, which consists of three steps. First, a dewarping model suitable for the type of lens distortion is selected, and the free model parameters are found from the calibration image. In this study, the results of using a second-order rational function (R2) and a bicubic polynominal (P3) have been investigated and mutually compared. Then, a PIV analysis near a reference geometry, which in this case is a flat plate used in the ZPG-TBL experiment, is performed to align the calibration target with the flow. Finally, the mapping function is applied to the PIV measurement, with two approaches investigated. The first approach is to dewarp the images before PIV analysis, and the second one is to dewarp the PIV velocity fields produced by the distorted image pairs. The result shows that the lens distortion can create up to 100% error in the Reynolds normal stress, especially near the wall. Also, the results demonstrate that the use of the P3 dewarping model to correct lens distortion yields better results than the R2 dewarping model. Furthermore, both approaches for the P3 dewarping model yield results which are statistically indistinguishable. As dewarpping the PIV velocity fields produced by the distorted image pairs is more efficient than dewarpping individual PIV images, the former one is recommended

- Proper orthogonal decomposition is used to decompose the velocity fields acquired by the 2C-2D PIV measurement, and the large scale motion is extracted from the PIV measurement by the most energetic POD modes.
  - A convergence test of the POD analysis is performed by randomly sampling 2C-2D velocity fields of the same turbulent boundary layer flow and study the statistics of the eigenvalues resulting from POD as a function of the number of snapshots used. The result shows that the averaged eigenvalues of the first 30 most energetic modes, which contain around 46% of the flow energy, do not change if more 2,500 snapshots are used for POD analysis. However, the standard deviations of the resulting eigenvalues reduce as more snapshots are included, and 10,000 snapshots are required for the POD analysis to achieve a standard deviation of 1% of mean for the first six eigenvalues.
- The contribution of the large scale motions to the skin friction coefficient is studied through a Renald-Deck decomposition of skin friction coefficient. Renald-Deck decomposition decomposes the skin friction coefficient into viscous dissipation term, turbulent kinetic energy production term and the boundary layer growth term. The turbulent kinetic energy production term is the most associated with large scale motions, and it is found to increase under the influence of large scale motions through a conditional statistics analysis. This result shows the large scale motions' vital role in turbulent production and Reynolds stress generation.

Appendix A

Fresnel and Fraunhofer Diffraction

Fresnel and Fraunhofer diffraction equations are approximations to the Angular spectrum method introduced in section 3.1.1. Although they are not implemented in the 4D-DHPIV/PTV algorithm developed in this thesis, they enable the calculation of the diffraction pattern of simple geometries such as a pinhole, and can provide some analytical insight to the holograms produced by the particles. Thus, they are discussed in this appendix.

A.1 Fresnel diffraction

Sherman [162] showed that the angular spectrum propagation equation is equivalent to the first Rayleigh-Sommerfeld diffraction formula, as following:

$$U(x, y, z) = \frac{z}{j\lambda} \iint_{\Sigma} U(\xi, \eta) \frac{\exp{(jkr_{01})}}{r_{01}^2} \, d\xi \, d\eta, \tag{A.1}$$

where (x, y) and (ξ, η) are the coordinate systems in the image and diffraction plane, respectively, z is the propagation distance, and r_{01} is distance between the propagation and image coordinates given by

$$r_{01} = z\sqrt{1 + \left(\frac{x - \xi}{z}\right)^2 + \left(\frac{y - \eta}{z}\right)^2}. \tag{A.2}$$

The major difficulty of solving the Rayleigh-Sommerfeld diffraction formula is the integration of the r_{01} term, as there is no analytical solution to the integration. Therefore, an approximation is made to the r_{01} term. Considering the function $\sqrt{1+b}$, it can be binomial expanded as follows,

$$\sqrt{1+b} = 1 + \frac{1}{2}b - \frac{1}{8}b^2 + \cdots , \tag{A.3}$$

The Fresnel diffraction applies the binomial expansion to r_{01} and retaining only the first two terms, yields

$$r_{01} \approx z \left[1 + \frac{1}{2}\left(\frac{x-\xi}{z}\right)^2 + \frac{1}{2}\left(\frac{y-\eta}{z}\right)^2 \right]. \tag{A.4}$$

The condition for this approximation to be valid is that the second order term contribute less than one radian to the resulting phase change, which can be expressed as,

$$z^3 \gg \frac{\pi}{4\lambda}\left[(x-\xi)^2 + (y-\eta)^2\right]^2_{\max}. \tag{A.5}$$

This shows that for the Fresnel diffraction to be accurate, the viewing position can't be too far away from the centreline of the beam, therefore, the approximation used in the Fresnel diffraction is also called a paraxial approximation. For an aperture size of $1\mu m$ illuminated by a $532nm$ laser and captured by a $20mm \times 20mm$ sensor, the distance between the sensor and the particle has to satisfy $z \gg 250mm$. Substituting the equation A.4 back to equation A.1 results in

$$U(x,y,z) = \frac{e^{jkz}}{j\lambda z} \iint_{-\infty}^{\infty} U(\xi,\eta) \exp\left\{ j\frac{k}{2z}\left[(x-\xi)^2 + (y-\eta)^2\right]\right\} d\xi\, d\eta\ , \tag{A.6}$$

which is the Fresnel diffraction equation. Equation A.6 can be recognised as a convolution between the image $U(\xi,\eta)$ and the diffraction kernel,

$$h(x,y) = \frac{e^{jkz}}{j\lambda z} \exp\left[j\frac{k}{2z}\left(x^2+y^2\right)\right] \tag{A.7}$$

Another way to view equation A.6 is to expand the quadrant phase term and move the $\exp\left[j\frac{k}{2z}\left(x^2+y^2\right)\right]$ term out of the integral since it does not depend on ξ or η, resulting in

$$U(x, y, z) = \frac{e^{jkz}}{j\lambda z} e^{j\frac{k}{2z}\left(x^2+y^2\right)} \iint_{-\infty}^{\infty} \left\{U(\xi, \eta) e^{j\frac{k}{2z}\left(\xi^2+\eta^2\right)}\right\} e^{-j\frac{2\pi}{\lambda}(x\xi+y\eta)}\, d\xi\, d\eta \ . \tag{A.8}$$

Besides the multiplication factors in the front, the Fresnel diffraction is a Fourier transform of the aperture modified by a quadratic phase exponential.

A.2 Fraunhofer diffraction

aFraunhofer diffraction further approximates the Rayleigh-Sommerfeld diffraction formula by only considering the first term of the binomial expansion of the term r_{01}, thus, $r_{01} \approx z$. Under this approximation, the quadratic phase term in equation A.7 is approximately one, resulting in,

$$U(x, y, z) = \frac{e^{jkz}}{j\lambda z} e^{j\frac{k}{2z}\left(x^2+y^2\right)} \iint_{-\infty}^{\infty} U(\xi, \eta) e^{-j\frac{2\pi}{\lambda}(x\xi+y\eta)}\, d\xi\, d\eta \ . \tag{A.9}$$

The integral of the equation A.9 is recognised as the Fourier transform of the $U(\xi, \eta)$, which can be written as

$$U(x, y, z) = \frac{e^{jkz}}{j\lambda z} e^{j\frac{k}{2z}\left(x^2+y^2\right)} \mathscr{F}\left(U(\xi, \eta)\right) \ . \tag{A.10}$$

The condition necessary for this approximation to apply is

$$z^3 \gg \frac{k\left(\xi^2+\eta^2\right)_{\max}}{2}. \tag{A.11}$$

A.3 Fraunhofer diffraction hologram of a particle

This section presents the calculation of the hologram produced by a particle illuminated by a planar wave using Fraunhofer Diffraction. The model of the particle is a circular block of radius r_0 illuminated by a planar wave of amplitude A. Without loss of generality, the phase of the illumination wave is assumed to be zero at the particle plane. The transmitted light field can be expressed in cylindrical coordinates as,

$$U(r,0) = \begin{cases} 0, & r \le r_0; \\ A, & r > r_0; \end{cases} . \tag{A.12}$$

A.3.1 Fraunhofer diffraction equation for radially symmetric function

In order to transform the Fraunhofer diffraction equation, represented by equation A.10, into cylindrical coordinate system, the following transformations are made:

$$\begin{aligned} x &= r\cos(\theta) \\ y &= r\sin(\theta) \\ f_x &= \rho\cos(\phi) \\ f_y &= \rho\sin(\phi) \end{aligned} \tag{A.13}$$

where θ and r denote the circumferential and radial directions of the coordinates, with ϕ and ρ denoting the frequencies in those directions. In order to transform the Fourier operator to cylindrical coordinates, first consider the Fourier transformation in Cartesian coordinates,

$$\mathscr{F}(U) = \iint_{-\infty}^{\infty} U(\xi,\eta)e^{-j\frac{2\pi}{\lambda}(x\xi+y\eta)}\, d\xi\, d\eta\ , \tag{A.14}$$

Substitute equation A.13 into equation A.14, and for a circular symmetric function $U(r)$,

$$\begin{aligned} \mathscr{F}(U(r)) &= \int_0^{2\pi} d\theta \int_0^{\infty} rU(r)e^{-j2\pi\rho r\left(\sin(\theta)\sin(\phi)+\cos(\theta)\cos(\phi)\right)}\, dr \\ &= \int_0^{2\pi} d\theta \int_0^{\infty} rU(r)e^{-j2\pi\rho r\cos(\theta-\phi)}\, dr \\ &= \int_0^{\infty} rU(r) \int_0^{2\pi} e^{-j2\pi\rho r\cos(\theta-\phi)}\, d\theta\, dr \end{aligned} \tag{A.15}$$

Using the identity of the Bessel functions, $J_0(x) = \frac{1}{2\pi}\int_0^{2\pi} e^{-jx\cos(\theta-\phi)}\, d\theta$, where J_0 is the Bessel function of the first kind and zeroth order,

$$\mathscr{F}(U(r)) = 2\pi \int_0^{\infty} rU(r)J_0\left(2\pi\rho r\right) dr\ \ . \tag{A.16}$$

Equation A.16 is also known as Fourier-Bessel Transform, which is denoted by $\mathscr{B}()$. Therefore, for a circularly symmetric function, its Fraunhofer diffraction pattern can be calculated by,

$$U(r,z)=\frac{e^{jkz}}{j\lambda z}e^{j\frac{kr^2}{2z}}\mathscr{B}(U(r,0))_{\rho=\frac{r}{\lambda z}}\ . \tag{A.17}$$

A.3.2 Application of Fraunhofer diffraction function to the particle model

Substituting equation A.12 to equation A.17,

$$U(r,z)=\frac{e^{jkz}}{j\lambda z}e^{j\frac{kr^2}{2z}}\mathscr{B}\left(A-A\ \text{Step}\left(\frac{r}{r_0}\right)\right)_{\rho=\frac{r}{\lambda z}}\ , \tag{A.18}$$

where the step function, Step(x) is one when x is smaller or equal to one and zero otherwise. Because of the linearity of the Fourier transform, $\mathscr{B}\Big(A-A\ \text{Step}\left(r/r_0\right)\Big)=A\mathscr{B}(1)-A\mathscr{B}\Big(\text{Step}\left(r/r_0\right)\Big)$, thus,

$$U(r,z)=\frac{Ae^{jkz}}{j\lambda z}e^{j\frac{kr^2}{2z}}\mathscr{B}(1)_{\rho=\frac{r}{\lambda z}}-\frac{Ae^{jkz}}{j\lambda z}e^{j\frac{kr^2}{2z}}\mathscr{B}\left(\text{Step}\left(\frac{r}{r_0}\right)\right)_{\rho=\frac{r}{\lambda z}}\ . \tag{A.19}$$

The first term of equation A.19 represents the propagation of a planar wave, which represents a phase change of kz, therefore

$$U(r,z)=Ae^{jkz}-\frac{Ae^{jkz}}{j\lambda z}e^{j\frac{kr^2}{2z}}2\pi\int_0^{r_0}rJ_0\left(2\pi\rho r\right)dr\,|_{\rho=\frac{r}{\lambda z}}\ . \tag{A.20}$$

Define $r'=2\rho r\pi$, then $dr=\frac{1}{2\rho\pi}\,dr'$ and $r=\frac{r'}{2\rho\pi}$,

$$U(r,z)=Ae^{jkz}-\frac{Ae^{jkz}}{j\lambda z}e^{j\frac{kr^2}{2z}}\frac{1}{2\rho^2\pi}\int_0^{2\rho\pi r_0}r'\left(J_0(r')\right)dr'\,|_{\rho=\frac{r}{\lambda z}}\ . \tag{A.21}$$

Using the identity $\int_0^x rJ_0(r)\,dr=xJ_1(x)$,

$$\begin{aligned}U(r,z)&=Ae^{jkz}-\frac{Ae^{jkz}}{j\lambda z}e^{j\frac{kr^2}{2z}}\left(\frac{r_0}{\rho}J_1(2\pi\rho r_0)\right)_{\rho=\frac{r}{\lambda z}}\\&=Ae^{jkz}-\frac{Ae^{jkz}}{j\lambda z}e^{j\frac{kr^2}{2z}}\left(\frac{r_0\lambda z}{r}J_1\left(\frac{2\pi r r_0}{\lambda z}\right)\right)\ .\end{aligned} \tag{A.22}$$

The hologram generated is the squared amplitude of the light field, therefore,

$$H(r,z) = \text{abs}\left[Ae^{jkz} - \frac{Ae^{jkz}}{j\lambda z}e^{j\frac{kr^2}{2z}}\left(\frac{r_0\lambda z}{r}J_1\left(\frac{2\pi r r_0}{\lambda z}\right)\right)\right]^2 . \tag{A.23}$$

The radial profile of a simulated hologram using equation A.23 compared with the profile calculated using angular spectrum method is presented in figure A.1. The result shows that equation A.23 captures well the frequency and general shape of the hologram, however, the peak value and the decay rate of the profile is underestimated. Under the simulation condition, $\frac{2z^3}{k\left(\xi^2+\eta^2\right)_{\max}} = 50$ which is not much bigger than 1, therefore the criteria for Fraunhofer diffraction regime is not strictly satisfied, which can explain the difference in profile observed in figure A.1.

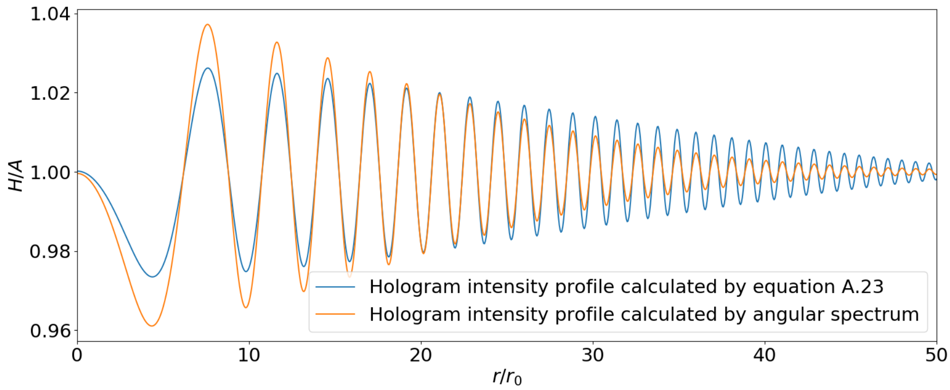

Figure A.1: Radial profile of the simulated holograms using angular spectrum method and equation A.23, the particle has a radius of $58\mu m$ located at $1m$ away from the imaging plane. The hologram is captured by a virtual imaging sensor of size 4096×4096 pixels with pixel size $5.86\mu m$.

Bibliography

[1] Bihai Sun, Asif Ahmed, Callum Atkinson, and Julio Soria. A novel 4D digital holographic PIV/PTV (4D-DHPIV/PTV) methodology using iterative predictive inverse reconstruction. *Measurement Science and Technology*, 31(10):104002, 7 2020. doi: 10.1088/1361-6501/ab8ee8. URL https://doi.org/10.1088/1361-6501/ab8ee8.

[2] Bihai Sun, Muhammad Shehzad, Daniel Jovic, Christophe Cuvier, Christian Willert, Yasar Ostovan, Jean-Marc Foucaut, Callum Atkinson, and Julio Soria. Distortion correction of two-component – two-dimensional piv using a large imaging sensor with application to measurements of a turbulent boundary layer flow at $Re_\tau = 2,386$. *Experiment in Fluids*, 2021.

[3] Muhammad Shehzad, Bihai Sun, Daniel Jovic, Christophe Cuvier, Christian Willert, Yasar Ostovan, Jean-Marc Foucaut, Callum Atkinson, and Julio Soria. Investigation of large scale motions in zero and adverse pressure gradient turbulent boundary layers using high-spatial-resolution PIV. *Experimental Thermal and Fluid Science*, 2021.

[4] Julio Soria, Bihai Sun, Asif Ahmed, and Callum Atkinson. 4D digital holographic PIV/PTV with 3D volume deconvolution and predictive inverse reconstruction. In *13th International Symposium on Particle Image Velocimetry*, Jul 2019.

[5] Bihai Sun, Asif Ahmed, Callum Atkinson, and Julio Soria. Using a new 4D digital holographic PIV/PTV (4D-DHPIV/PTV) methodology to measure wall-bounded shear flows. In *13th International Symposium on Particle Image Velocimetry*, Jul 2019.

[6] Bihai Sun, Asif Ahmed, Callum Atkinson, and Julio Soria. The effect of shot noise on the accuracy of particle positions in hologram reconstruction using an inverse method. In *IX Australian Conference on Laser Diagnostics*, Dec 2019.

[7] Asif Ahmed, Bihai Sun, Victor J. Cadarso, Callum Atkinson, and Julio Soria. Enhancing digital holographic microscopic PIV by exploiting the contrast inversion

property of weak scattering tracer particles. In *IX Australian Conference on Laser Diagnostics*, Dec 2019.

[8] Asif Ahmed, Bihai Sun, Victor J. Cadarso, and Julio Soria. 3D localization of the tracer particles in digital inline holographic microscopy PIV/PTV: do the bright regions in the intensity reconstruction volume really correspond to the tracer particles? In *73rd Annual Meeting of the APS Division of Fluid Dynamics*, Nov 2020.

[9] L. Prandtl. Über Flüssigkeitsbewegung bei sehr kleiner Reibung. In *Verhandlungen des dritten internationalenMathematiker-Kongresses*, Heidelberg, 1904. doi: 10.1007/978-3-662-11836-8_43.

[10] S. J. Kline, W. C. Reynolds, F. A. Schraub, and P. W. Runstadler. The structure of turbulent boundary layers. *Journal of Fluid Mechanics*, 30(4):741–773, 1967. ISSN 14697645. doi: 10.1017/S0022112067001740.

[11] S. Robinson. Coherent Motions In The Turbulent Boundary Layer. *Annual Review of Fluid Mechanics*, 23(1):601–639, 1991. ISSN 00664189. doi: 10.1146/annurev.fluid.23.1.601.

[12] Stephen B. Pope. *Turbulent Flows*. Cambridge University Press, aug 2000. ISBN 9780521591256. doi: 10.1017/CBO9780511840531. URL https://www.cambridge.org/core/product/identifier/9780511840531/type/book.

[13] Lewis F. Richardson. Atmospheric diffusion shown on a distance-neighbour graph. *Proceedings of the Royal Society of London. Series A, Containing Papers of a Mathematical and Physical Character*, 110(756):709–737, apr 1926. ISSN 0950-1207. doi: 10.1098/rspa.1926.0043. URL https://royalsocietypublishing.org/doi/10.1098/rspa.1926.0043.

[14] A. Kolmogorov. The Local Structure of Turbulence in Incompressible Viscous Fluid for Very Large Reynolds' Numbers. *Akademiia Nauk SSSR Doklady*, 30:301–305, January 1941.

[15] Osborne Reynolds. IV. On the dynamical theory of incompressible viscous fluids and the determination of the criterion. *Philosophical Transactions of the Royal Society of London. (A.)*, 186:123–164, dec 1895. ISSN 0264-3820. doi: 10.1098/rsta.1895.0004. URL https://royalsocietypublishing.org/doi/10.1098/rsta.1895.0004.

[16] E. Buckingham. On Physically Similar Systems; Illustrations of the Use of Dimensional Equations. *Physical Review*, 4(4):345–376, oct 1914. ISSN 0031-899X. doi:

10.1103/PhysRev.4.345. URL https://link.aps.org/doi/10.1103/PhysRev.4.345.

[17] J. Klewicki, P. Fife, T. Wei, and P. McMurtry. Overview of a methodology for scaling the indeterminate equations of wall turbulence. *AIAA Journal*, 44(11): 2475–2481, 2006. ISSN 00011452. doi: 10.2514/1.18911.

[18] Philippe R. Spalart. Direct simulation of a turbulent boundary layer up to R θ = 1410. *Journal of Fluid Mechanics*, 187:61–98, feb 1988. ISSN 0022-1120. doi: 10.1017/S0022112088000345. URL https://www.cambridge.org/core/product/identifier/S0022112088000345/type/journal{_}article.

[19] Anthony F Molland and Stephen R Turnock. Physics of control surface operation. In *Marine Rudders and Control Surfaces*, pages 21–56. Elsevier, 2007. ISBN 9780750669443. doi: 10.1016/B978-075066944-3/50006-8. URL https://linkinghub.elsevier.com/retrieve/pii/B9780750669443X50008https://linkinghub.elsevier.com/retrieve/pii/B9780750669443500068.

[20] F R Hama. Boundary-layer transition induced by a vibrating ribbon on a flat plate. *Proc. Heat Transfer and Fluid Mech. Inst.*, pages 92–105, 1960.

[21] Yonghua Yan, Caixia Chen, Huankun Fu, and Chaoqun Liu. DNS study on Λ-vortex and vortex ring formation in flow transition at mach number 0.5. *Journal of Turbulence*, 15(1):1–21, 2014. doi: 10.1080/14685248.2013.871023.

[22] T Theodorsen. Mechanism of turbulence. *Proc. Midwest. Conf. Fluid Mech. 2nd,Columbus, Ohio*, 1719:1–18, 1952.

[23] C. B. Lee and J. Z. Wu. Transition in wall-bounded flows. *Applied Mechanics Reviews*, 61(1-6):0308021–03080221, 2008. ISSN 00036900. doi: 10.1115/1.2909605.

[24] Cunbiao Lee and Xianyang Jiang. Flow structures in transitional and turbulent boundary layers, 2019. ISSN 10897666. URL https://aip.scitation.org/doi/abs/10.1063/1.5121810.

[25] M. R. Head and P. Bandyopadhyay. New aspects of turbulent boundary-layer structure. *Journal of Fluid Mechanics*, 107(11):297–338, 1981. ISSN 14697645. doi: 10.1017/S0022112081001791.

[26] Xiaohua Wu and Parviz Moin. Direct numerical simulation of turbulence in a nominally zero-pressure-gradient flat-plate boundary layer. *Journal of Fluid Mechanics*, 630:5–41, 2009. ISSN 00221120. doi: 10.1017/S0022112009006624.

[27] Ronald J. Adrian. Hairpin vortex organization in wall turbulence. *Physics of Fluids*, 19(4), 2007. ISSN 10706631. doi: 10.1063/1.2717527.

[28] Jigen Zhou, Ronald J. Adrian, and S. Balachandar. Autogeneration of near-wall vortical structures in channel flow. *Physics of Fluids*, 8(1):288–290, 1996. ISSN 10706631. doi: 10.1063/1.868838.

[29] J. Zhou, R. J. Adrian, S. Balachandar, and T. M. Kendall. Mechanisms for generating coherent packets of hairpin vortices in channel flow. *Journal of Fluid Mechanics*, 387:353–396, 1999. ISSN 00221120. doi: 10.1017/S002211209900467X.

[30] R. J. Adrian, C. D. Meinhart, and C. D. Tomkins. Vortex organization in the outer region of the turbulent boundary layer. *Journal of Fluid Mechanics*, 422: 1–54, 2000. ISSN 00221120. doi: 10.1017/S0022112000001580.

[31] Promode R. Bandyopadhyay. TURBULENCE SPOT-LIKE FEATURES OF A BOUNDARY LAYER. *Annals of the New York Academy of Sciences*, 404(1 Fourth Intern):393–395, may 1983. ISSN 0077-8923. doi: 10.1111/j.1749-6632.1983.tb19504.x. URL http://doi.wiley.com/10.1111/j.1749-6632.1983.tb19504.x.

[32] M. S. Chong, A. E. Perry, and B. J. Cantwell. A general classification of three-dimensional flow fields. *Physics of Fluids A: Fluid Dynamics*, 2(5):765–777, may 1990. ISSN 0899-8213. doi: 10.1063/1.857730. URL http://aip.scitation.org/doi/10.1063/1.857730.

[33] John W. Brooke and T. J. Hanratty. Origin of turbulence-producing eddies in a channel flow. *Physics of Fluids A: Fluid Dynamics*, 5(4):1011–1022, apr 1993. ISSN 0899-8213. doi: 10.1063/1.858666. URL http://aip.scitation.org/doi/10.1063/1.858666.

[34] C. R. Smith, J. D. A. Walker, A. H. Haidari, and U. Sobrun. On the dynamics of near-wall turbulence. *Philosophical Transactions of the Royal Society of London. Series A: Physical and Engineering Sciences*, 336(1641):131–175, 1991. ISSN 0962-8428. doi: 10.1098/rsta.1991.0070. URL https://royalsocietypublishing.org/doi/10.1098/rsta.1991.0070.

[35] J. Kim and J. Lim. A linear process in wall-bounded turbulent shear flows. *Physics of Fluids*, 12(8):1885–1888, 2000. ISSN 10706631. doi: 10.1063/1.870437.

[36] H. T. Kim, S. J. Kline, and W. C. Reynolds. The production of turbulence near a smooth wall in a turbulent boundary layer. *Journal of Fluid Mechanics*, 50(1): 133–160, 1971. ISSN 14697645. doi: 10.1017/S0022112071002490.

[37] C. R. Smith and S. P. Metzler. The characteristics of low-speed streaks in the near-wall region of a turbulent boundary layer. *Journal of Fluid Mechanics*, 129: 27–54, 1983. ISSN 14697645. doi: 10.1017/S0022112083000634.

[38] R. E. Falco. Coherent motions in the outer region of turbulent boundary layers. *Physics of Fluids*, 20(10), 1977. ISSN 10706631. doi: 10.1063/1.861721.

[39] C. C. Chu and R. E. Falco. Vortex ring/viscous wall layer interaction model of the turbulence production process near walls. *Experiments in Fluids*, 6(5):305–315, 1988. ISSN 07234864. doi: 10.1007/BF00538821.

[40] R. E. Falco. A coherent structure model of the turbulent boundary layer and its ability to predict Reynolds number dependence. *Philosophical Transactions of the Royal Society of London. Series A: Physical and Engineering Sciences*, 336(1641): 103–129, 1991. ISSN 0962-8428. doi: 10.1098/rsta.1991.0069.

[41] N. Hutchins and Ivan Marusic. Evidence of very long meandering features in the logarithmic region of turbulent boundary layers. *Journal of Fluid Mechanics*, 579: 1–28, 2007. ISSN 00221120. doi: 10.1017/S0022112006003946.

[42] A. A. Townsend. *The turbulent boundary layer*, pages 1–15. Springer Berlin Heidelberg, Berlin, Heidelberg, 1958. ISBN 978-3-642-45885-9. doi: 10.1007/978-3-642-45885-9_1. URL https://doi.org/10.1007/978-3-642-45885-9_1.

[43] P. Bradshaw. 'Inactive' motion and pressure fluctuations in turbulent boundary layers. *Journal of Fluid Mechanics*, 30(2):241–258, 1967. ISSN 14697645. doi: 10.1017/S0022112067001417.

[44] A. Favre, J. Gaviglio, and R. Dumas. Structure of velocity space-time correlations in a boundary layer. *Physics of Fluids*, 10(9), 1967. ISSN 10706631. doi: 10.1063/1.1762432.

[45] D. J. Tritton. Some new correlation measurements in a turbulent boundary layer. *Journal of Fluid Mechanics*, 28(3):439–462, 1967. ISSN 14697645. doi: 10.1017/S0022112067002216.

[46] Ron F. Blackwelder and Leslie S.G. Kovasznay. Time scales and correlations in a turbulent boundary layer. *Physics of Fluids*, 15(9):1545–1554, 1972. ISSN 10706631. doi: 10.1063/1.1694128.

[47] K. J. Bullock, R. E. Cooper, and F. H. Abernathy. Structural similarity in radial correlations and spectra of longitudinal velocity fluctuations in pipe flow. *Journal of Fluid Mechanics*, 88(3):585–608, 1978. ISSN 14697645. doi: 10.1017/S0022112078002293.

[48] Z. Liu, R. J. Adrian, and T. J. Hanratty. Large-scale modes of turbulent channel flow: Transport and structure. *Journal of Fluid Mechanics*, 448:53–80, 2001. ISSN 00221120. doi: 10.1017/s0022112001005808.

[49] Romain Mathis, Nicholas Hutchins, and Ivan Marusic. Large-scale amplitude modulation of the small-scale structures in turbulent boundary layers. *Journal of Fluid Mechanics*, 628:311–337, 2009. ISSN 00221120. doi: 10.1017/S0022112009006946.

[50] O Reynolds. On the action of rain to calm the sea. *Proc. Liter. Phil. Soc. Manchester*, XIV:72–74, 1875.

[51] Giuseppe P. Russo. Flow visualization. In *Aerodynamic Measurements*, chapter 6, pages 161–216. Woodhead Publishing, 2011. ISBN 978-1-84569-992-5.

[52] Francis R. Hama. Streaklines in a perturbed shear flow. *Physics of Fluids*, 5(6): 644–650, 1962. ISSN 10706631. doi: 10.1063/1.1706678.

[53] M. D. Atkins and M. F. Boer. Flow Visualization. In *Application of Thermo-Fluidic Measurement Techniques: An Introduction*, pages 15–59. Butterworth-Heinemann Books, 2016. ISBN 9780128098745. doi: 10.1016/B978-0-12-809731-1.00002-2.

[54] Abdullah M. Kuraan and Ömer Savaş. Smoke streak visualization of steady flows over a spinning cone at angle of attack in flight. *Journal of Visualization*, 23(2): 191–205, 2020. ISSN 18758975. doi: 10.1007/s12650-019-00621-1.

[55] F R Hama and J. Nutant. Detailed flow-field observations in the transition process in a thick boundary layer. *Heat Transfer & Fluid Mechanics Institute*, pages 77–93, 1963.

[56] Cun Biao Lee. New features of CS solitons and the formation of vortices. *Physics Letters, Section A: General, Atomic and Solid State Physics*, 247(6):397–402, 1998. ISSN 03759601. doi: 10.1016/S0375-9601(98)00582-9.

[57] J. W. Elder. An experimental investigation of turbulent spots and breakdown to turbulence. *Journal of Fluid Mechanics*, 9(2):235–246, 1960. ISSN 14697645. doi: 10.1017/S0022112060001079.

[58] John Hall Gladstone and T. P. Dale. XIV. Researches on the refraction, dispersion, and sensitiveness of liquids. *Philosophical Transactions of the Royal Society of London*, 153:317–343, dec 1863. ISSN 0261-0523. doi: 10.1098/rstl.1863.0014. URL https://royalsocietypublishing.org/doi/10.1098/rstl.1863.0014.

[59] Y E Htun, Zay Yar, and Myo Myint. Some Principles of Flow Visualization Techniques in Wind Tunnels. *International Journal of Advances in Science Engineering and Technology*, 4(4):2321–9009, 2016. URL http://iraj.in.

[60] G Comte-Bellot. Hot-Wire Anemometry. *Annual Review of Fluid Mechanics*, 8(1):209–231, jan 1976. ISSN 0066-4189. doi: 10.1146/annurev.fl.08.010176.001233. URL http://www.annualreviews.org/doi/10.1146/annurev.fl.08.010176.001233.

[61] A. E. KENNELLY, C. A. WRIGHT, and J. S. VAN BYLEVELT. The convection of heat from small copper wires. *Transactions of the American Institute of Electrical Engineers*, 28:363–393, 1909. ISSN 00963860. doi: 10.1109/T-AIEE.1909.4768172.

[62] S. Corrsin. Turbulence: Experimental Methods. *Handbuch der Physik*, 3:524–590, January 1963. doi: 10.1007/978-3-662-10109-4_4.

[63] G. Comte-Bellot and J. P. Schon. Harmoniques crees par excitation parametrique dans les anemometres a fil chaud a intensite constante. *International Journal of Heat and Mass Transfer*, 12(12):1661–1677, 1969. ISSN 00179310. doi: 10.1016/0017-9310(69)90099-4.

[64] B. J. Bellhouse and D. L. Schultz. The determination of fluctuating velocity in air with heated thin film gauges. *Journal of Fluid Mechanics*, 29(2):289–295, 1967. ISSN 14697645. doi: 10.1017/S0022112067000813.

[65] Stanley Corrsin. Extended applications of the hot-wire anemometer. *Review of Scientific Instruments*, 18(7):469–471, 1947. ISSN 00346748. doi: 10.1063/1.1740981.

[66] Mahinder S. Uberoi and Leslie S. G. Kovasznay. On mapping and measurement of random fields. *Quarterly of Applied Mathematics*, 10(4):375–393, 1953. ISSN 0033-569X. doi: 10.1090/qam/51466.

[67] Giuseppe P. Russo. 3 - hot wire anemometer. In Giuseppe P. Russo, editor, *Aerodynamic Measurements*, pages 67–98. Woodhead Publishing, 2011. ISBN 978-1-84569-992-5. doi: https://doi.org/10.1533/9780857093868.67. URL https://www.sciencedirect.com/science/article/pii/B9781845699925500036.

[68] Finn E Jorgensen. *How to measure turbulence with hot-wire anemometers - A practical guide*. Dantec Dynamics, 2002.

[69] J. H. Citriniti and W. K. George. Reconstruction of the global velocity field in the axisymmetric mixing layer utilizing the proper orthogonal decomposition. *Journal of Fluid Mechanics*, 418:137–166, 2000. ISSN 00221120. doi: 10.1017/S0022112000001087.

[70] P. M. Ligrani and P. Bradshaw. Spatial resolution and measurement of turbulence in the viscous sublayer using subminiature hot-wire probes. *Exp. Fluids*, 5(6 , 1987, p.407-417.), 1987. ISSN 07234864.

[71] N. Hutchins, T. B. Nickels, I. Marusic, and M. S. Chong. Hot-wire spatial resolution issues in wall-bounded turbulence. *Journal of Fluid Mechanics*, 635:103–136, 2009. ISSN 00221120. doi: 10.1017/S0022112009007721.

[72] Jerry Westerweel, Gerrit E. Elsinga, and Ronald J. Adrian. Particle image velocimetry for complex and turbulent flows. *Annual Review of Fluid Mechanics*, 45:409–436, 2013. ISSN 00664189. doi: 10.1146/annurev-fluid-120710-101204.

[73] H. Z. Cummins, N. Knable, and Y. Yeh. Observation of diffusion broadening of rayleigh scattered light. *Phys. Rev. Lett.*, 12:150–153, Feb 1964. doi: 10.1103/PhysRevLett.12.150. URL https://link.aps.org/doi/10.1103/PhysRevLett.12.150.

[74] Zhan Qi Tang, Nan Jiang, Andreas Schröder, and Reinhard Geisler. Tomographic PIV investigation of coherent structures in a turbulent boundary layer flow. *Acta Mechanica Sinica/Lixue Xuebao*, 28(3):572–582, 2012. ISSN 05677718. doi: 10.1007/s10409-012-0082-y.

[75] L. Kourentis and E. Konstantinidis. Uncovering large-scale coherent structures in natural and forced turbulent wakes by combining PIV, POD, and FTLE. *Experiments in Fluids*, 52(3):749–763, 2012. ISSN 07234864. doi: 10.1007/s00348-011-1124-0.

[76] D. R. Sabatino and T. Rossmann. Tomographic PIV measurements of a regenerating hairpin vortex. *Experiments in Fluids*, 57(1):1–13, 2016. ISSN 07234864. doi: 10.1007/s00348-015-2089-1.

[77] C. D. Tomkins and R. J. Adrian. Spanwise structure and scale growth in turbulent boundary layers. *Journal of Fluid Mechanics*, 490:37–74, 2003. ISSN 00221120. doi: 10.1017/S0022112003005251.

[78] Donald B. Altman. Statistics of optimal particle streak photography. *Physics of Fluids A*, 3(9):2132–2137, 1991. ISSN 08998213. doi: 10.1063/1.857895.

[79] R.K. Erf. Application of laser speckle to measurement. *Laser Appl.*, 4(1):69, 1980.

[80] Christopher J. D. Pickering and Neil A. Halliwell. Speckle photography in fluid flows: signal recovery with two-step processing. *Applied Optics*, 23(8):1128, 1984. ISSN 0003-6935. doi: 10.1364/ao.23.001128.

[81] Ronald J. Adrian. Scattering particle characteristics and their effect on pulsed laser measurements of fluid flow: speckle velocimetry vs particle image velocimetry. *Applied Optics*, 23(11):1690, 1984. ISSN 0003-6935. doi: 10.1364/ao.23.001690.

[82] Ronald J. Adrian. Particle-imaging techniques for experimental fluid mechanics. *Annual Review of Fluid Mechanics*, 23(1):261–304, 1991. ISSN 00664189. doi: 10.1146/annurev.fl.23.010191.001401.

[83] C. E. Willert and M. Gharib. Digital particle image velocimetry. *Experiments in Fluids*, 10(4):181–193, jan 1991. ISSN 0723-4864. doi: 10.1007/BF00190388. URL http://link.springer.com/10.1007/BF00190388.

[84] Julio Soria. An investigation of the near wake of a circular cylinder using a video-based digital cross-correlation particle image velocimetry technique. *Exp. Thermal Fluid Sci.*, 12:221–233, 1996.

[85] Christian E. Willert. High-speed particle image velocimetry for the efficient measurement of turbulence statistics. *Experiments in Fluids*, 56(1), 2015. ISSN 07234864. doi: 10.1007/s00348-014-1892-4.

[86] L. Adrian, R.J. Adrian, and J. Westerweel. *Particle Image Velocimetry*. Cambridge Aerospace Series. Cambridge University Press, 2011. ISBN 9780521440080.

[87] Markus Raffel, Christian E Willert, Fulvio Scarano, Christian J Kähler, Steven T Wereley, and Jürgen Kompenhans. *Particle Image Velocimetry: A Practical Guide*. Springer, 2018. ISBN 978-3-319-68852-7. URL https://doi.org/10.1007/978-3-319-68852-7{_}1.

[88] Julio Soria. Digital particle image velocimetry. In *Digital Optical Measurement: Techniques and Applications*, Artech House applied photonics series, pages 347–375. Artech House, 2015. ISBN 9781608078066. URL https://books.google.com.au/books?id=3U0KrgEACAAJ.

[89] D. P. Hart. PIV error correction. *Experiments in Fluids*, 29(1):13–22, 2000. ISSN 07234864. doi: 10.1007/s003480050421.

[90] M. Raffel, B. Leitl, and J. Kompenhans. Data Validation for Particle Image Velocimetry. *Laser Techniques and Applications in Fluid Mechanics*, pages 210–226, 1993. doi: 10.1007/978-3-662-02885-8_14.

[91] Jerry Westerweel and Fulvio Scarano. Universal outlier detection for PIV data. *Experiments in Fluids*, 39(6):1096–1100, dec 2005. ISSN 0723-4864. doi: 10.1007/s00348-005-0016-6. URL http://link.springer.com/10.1007/s00348-005-0016-6.

[92] John Griffin, Todd Schultz, Ryan Holman, Lawrence S. Ukeiley, and Louis N. Cattafesta. Application of multivariate outlier detection to fluid velocity measurements. *Experiments in Fluids*, 49(1):305–317, jul 2010. ISSN 0723-4864.

doi: 10.1007/s00348-010-0875-3. URL http://link.springer.com/10.1007/s00348-010-0875-3.

[93] M. Gaydon, M. Raffel, C. Willert, M. Rosengarten, and J. Kompenhans. Hybrid stereoscopic particle image velocimetry. *Experiments in Fluids*, 23(4):331–334, 1997. ISSN 07234864. doi: 10.1007/s003480050118.

[94] A. K. Prasad and R. J. Adrian. Stereoscopic particle image velocimetry applied to liquid flows. *Experiments in Fluids*, 15(1):49–60, 1993. ISSN 07234864. doi: 10.1007/BF00195595.

[95] Theodor Scheimpflug. Improved Method and apparatus for the Systematic Alteration or Distortion of Plane Pictures and Images by Means of Lenses and Mirrors for Photography and for other purposes, 1904. URL http://www.trenholm.org/hmmerk/TSBP.pdf.

[96] Markus Raffel, Christian E. Willert, Fulvio Scarano, Christian J. Kähler, Steven T. Wereley, and Jürgen Kompenhans. Stereoscopic PIV. In *Particle Image Velocimetry*, pages 285–307. Springer International Publishing, Cham, 2018. doi: 10.1007/978-3-319-68852-7_8. URL http://link.springer.com/10.1007/978-3-319-68852-7_8.

[97] A. K. Prasad. Stereoscopic particle image velocimetry. *Experiments in Fluids*, 29(2):103–116, aug 2000. ISSN 0723-4864. doi: 10.1007/s003480000143. URL http://link.springer.com/10.1007/s003480000143.

[98] G. E. Elsinga, F. Scarano, B. Wieneke, and B. W. van Oudheusden. Tomographic particle image velocimetry. *Experiments in Fluids*, 41(6):933–947, Dec 2006. ISSN 1432-1114. doi: 10.1007/s00348-006-0212-z.

[99] Callum Atkinson and Julio Soria. An efficient simultaneous reconstruction technique for tomographic particle image velocimetry. *Experiments in Fluids*, 47(4):553, 2009. doi: 10.1007/s00348-009-0728-0. URL https://doi.org/10.1007/s00348-009-0728-0.

[100] Daniel Schanz, Sebastian Gesemann, and Andreas Schröder. Shake-The-Box: Lagrangian particle tracking at high particle image densities. *Experiments in Fluids*, 57(5), 2016. ISSN 07234864. doi: 10.1007/s00348-016-2157-1.

[101] Callum Atkinson, Sebastien Coudert, Jean-Marc Foucaut, Michel Stanislas, and Julio Soria. The accuracy of tomographic particle image velocimetry for measurements of a turbulent boundary layer. *Experiments in Fluids*, 50(4):1031–1056, Apr 2011. ISSN 1432-1114. doi: 10.1007/s00348-010-1004-z.

[102] Jesse Belden, Tadd T Truscott, Michael C Axiak, and Alexandra H Techet. Three-dimensional synthetic aperture particle image velocimetry. *Measurement Science and Technology*, 21(12):125403, nov 2010. doi: 10.1088/0957-0233/21/12/125403.

[103] E. H. Adelson and J. Y. A. Wang. Single lens stereo with a plenoptic camera. *IEEE Transactions on Pattern Analysis and Machine Intelligence*, 14(2):99–106, Feb 1992. ISSN 1939-3539. doi: 10.1109/34.121783.

[104] Timothy W Fahringer, Kyle P Lynch, and Brian S Thurow. Volumetric particle image velocimetry with a single plenoptic camera. *Measurement Science and Technology*, 26(11):115201, 2015.

[105] Shengxian Shi, Junfei Ding, T H New, and Julio Soria. Light-field camera-based 3D volumetric particle image velocimetry with dense ray tracing reconstruction technique. *Experiments in Fluids*, 58(7):78, 2017.

[106] Shengxian Shi, Junfei Ding, Callum Atkinson, Julio Soria, and T. H. New. A detailed comparison of single-camera light-field piv and tomographic piv. *Experiments in Fluids*, 59(3):46, Feb 2018. ISSN 1432-1114. doi: 10.1007/s00348-018-2500-9.

[107] Nicolas A Buchmann, Christian E Willert, and Julio Soria. Pulsed, high-power LED illumination for tomographic particle image velocimetry. *Experiments in Fluids*, 53:1545–1560, 2012.

[108] Julio Soria. Three-component three-dimensional (3c-3d) fluid flow velocimetry for flow turbulence investigations. In *21st Australasian Fluid Mechanics Conference, Adelaide, Australia 10-13 December 2018*, 2018.

[109] Shawn K. Reinink and Metin I. Yaras. Study of coherent structures of turbulence with large wall-normal gradients in thermophysical properties using direct numerical simulation. *Physics of Fluids*, 27(6), 2015. ISSN 10897666. doi: 10.1063/1.4922388.

[110] Yi Jun Dai, Wei Xi Huang, and Chun Xiao Xu. Coherent structures in streamwise rotating channel flow. *Physics of Fluids*, 31(2), 2019. ISSN 10897666. doi: 10.1063/1.5051750.

[111] D. Gabor. A new microscopic principle. *Nature*, 161(4098):777–778, 1948. ISSN 1476-4687. doi: 10.1038/161777a0.

[112] Brian J. Thompson, John H. Ward, and William R. Zinky. Application of Hologram Techniques for Particle Size Analysis. *Applied Optics*, 6(3):519, 1967. ISSN 0003-6935. doi: 10.1364/ao.6.000519.

[113] Sébastien Coëtmellec, Cristina Buraga-Lefebvre, Denis Lebrun, and Cafer Özkul. Application of in-line digital holography to multiple plane velocimetry. *Measurement Science and Technology*, 12(9):1392–1397, aug 2001. doi: 10.1088/0957-0233/12/9/303.

[114] Shigeru Murata and Norifumi Yasuda. Potential of digital holography in particle measurement. *Optics & Laser Technology*, 32(7):567 – 574, 2000. ISSN 0030-3992. doi: https://doi.org/10.1016/S0030-3992(00)00088-8. Optical methods in heat and fluid flow.

[115] Gang Pan and Hui Meng. Digital holography of particle fields: reconstruction by use of complex amplitude. *Appl. Opt.*, 42(5):827–833, Feb 2003. doi: 10.1364/AO.42.000827.

[116] K von Ellenrieder and J Soria. Experimental measurements of particle depth of field in digital holography. In *International Workshop on Holographic metrology in Fluid Mechanics*, 2003.

[117] Julio Soria, Bihai Sun, Asif Ahmed, and Callum Atkinson. 4d digital holographic piv/ptv with 3d volume deconvolution and predictive inverse reconstruction. In *13th International Symposium on Particle Image Velocimetry, Munich July 22-24*, 2019.

[118] V Palero, M P Arroyo, and J Soria. Digital holography for micro-droplet diagnostics. *Experiments in Fluids*, 43(2):185–195, August 2007.

[119] Mie G. Beitrage Zur Optik Truber Medien, Speziell Kolloidaler Metallosungen. *Annalen Der Physik*, 25(3):377–445, 1908.

[120] Ludvig Valentin Lorenz. Lysbevaegelsen i og uden for en af plane lysbolger belyst kugle. *Det Kongelige Danske Videnskabernes Selskabs Skrifter*, 6(6):1–62, 1890.

[121] W. J. Wiscombe. Improved Mie scattering algorithms. *Applied Optics*, 19(9):1505–1509, 1980.

[122] C F Bohren and D R Huffman. *Absorption and Scattering by Small Particles*. WILEY-VCH Verlag GmbH, 1983.

[123] Laurence Wilson and Rongjing Zhang. 3d localization of weak scatterers in digital holographic microscopy using rayleigh-sommerfeld back-propagation. *Opt. Express*, 20(15):16735–16744, Jul 2012. doi: 10.1364/OE.20.016735.

[124] Joseph W. Goodman. *Introduction to Fourier optics*. New York : W.H. Freeman, fourth edition. edition, 2017.

[125] Julio Soria, Callum Atkinson, and Nicolas Buchmann. Hybrid piv-particle tracking technique applied to high reynolds number turbulent boundary layer measurements. In *67th Annual Meeting of the APS Division of Fluid Dynamics*, 2014.

[126] Tatiana Latychevskaia, Fabian Gehri, and Hans-Werner Fink. Depth-resolved holographic reconstructions by three-dimensional deconvolution. *Opt. Express*, 18 (21):22527–22544, Oct 2010. doi: 10.1364/OE.18.022527.

[127] William Hadley Richardson. Bayesian-based iterative method of image restoration∗. *J. Opt. Soc. Am.*, 62(1):55–59, Jan 1972. doi: 10.1364/JOSA.62.000055.

[128] L. B. Lucy. An iterative technique for the rectification of observed distributions. *Astron. J.*, 79:745–754, 1974. doi: 10.1086/111605.

[129] J. Hoshen and R. Kopelman. Percolation and cluster distribution. i. cluster multiple labeling technique and critical concentration algorithm. *Phys. Rev. B*, 14: 3438–3445, Oct 1976. doi: 10.1103/PhysRevB.14.3438.

[130] Ferréol Soulez, Loïc Denis, Corinne Fournier, Éric Thiébaut, and Charles Goepfert. Inverse-problem approach for particle digital holography: accurate location based on local optimization. *J. Opt. Soc. Am. A*, 24(4):1164–1171, Apr 2007. doi: 10.1364/JOSAA.24.001164.

[131] Richard H Byrd, Peihuang Lu, Jorge Nocedal, and Ciyou Zhu. A Limited Memory Algorithm for Bound Constrained Optimization. *SIAM Journal on Scientific Computing*, 16(5):1190–1208, September 1995.

[132] Charles Boncelet. Chapter 7 - image noise models. In Al Bovik, editor, *The Essential Guide to Image Processing*, pages 143 – 167. Academic Press, Boston, 2009. ISBN 978-0-12-374457-9. doi: https://doi.org/10.1016/B978-0-12-374457-9.00007-X.

[133] Rafael C. Gonzalez; Richard E. Woods. *Digital Image Processing*. Pearson, 3 edition, 2008. ISBN 9780131687288.

[134] Y. Wu and K. T. Christensen. Spatial structure of a turbulent boundary layer with irregular surface roughness. *Journal of Fluid Mechanics*, 655:380–418, 2010. ISSN 00221120. doi: 10.1017/S0022112010000960.

[135] Anne Marie Schreyer, Jean J. Lasserre, and Pierre Dupont. Development of a Dual-PIV system for high-speed flow applications. *Experiments in Fluids*, 56(10): 1–12, 2015. ISSN 07234864. doi: 10.1007/s00348-015-2053-0.

[136] D. A. Sergeev and A. A. Kandaurov. Investigation of free convection in the cubic cave with PIV and POD methods. *Scientific Visualization*, 11(3):103–110, 2019. ISSN 20793537. doi: 10.26583/sv.11.3.09.

[137] C M de Silva, E P Gnanamanickam, C Atkinson, N A Buchmann, J Hutchins, N Soria, and I. Marusic. High spatial range velocity measurements in a high Reynolds number turbulent boundary layer. *Physics of Fluids*, 26(2):025117, 2014.

[138] C. Cuvier, S. Srinath, M. Stanislas, J. M. Foucaut, J. P. Laval, C. J. Kähler, R. Hain, S. Scharnowski, A. Schröder, R. Geisler, J. Agocs, A. Röse, C. Willert, J. Klinner, O. Amili, C. Atkinson, and J. Soria. Extensive characterisation of a high reynolds number decelerating boundary layer using advanced optical metrology. *Journal of Turbulence*, 18(10):929–972, 2017. doi: 10.1080/14685248.2017.1342827.

[139] R. Konrath and W. Schröder. Telecentric lenses for imaging in particle image velocimetry: a new stereoscopic approach. *Experiments in Fluids*, 33(5):703–708, nov 2002. ISSN 0723-4864. doi: 10.1007/s00348-002-0531-7. URL http://link.springer.com/10.1007/s00348-002-0531-7.

[140] J.L. Lumley. The structure of inhomogeneous turbulent flows. *Proceedings of the international colloquium*, pages 166–167, 1967. ISSN 00976156.

[141] Nicolas Renard and Sébastien Deck. A theoretical decomposition of mean skin friction generation into physical phenomena across the boundary layer. *Journal of Fluid Mechanics*, 790:339–367, 2016. ISSN 14697645. doi: 10.1017/jfm.2016.12.

[142] Jong-Hwan Yoon and Sang-Joon Lee. Direct comparison of 2D PIV and stereoscopic PIV measurements. *Measurement Science and Technology*, 13(10):1631–1642, oct 2002. ISSN 0957-0233. doi: 10.1088/0957-0233/13/10/317. URL https://iopscience.iop.org/article/10.1088/0957-0233/13/10/317.

[143] Duane C. Brown. Close-range camera calibration. *Photogrammetric Engineering*, 37(8):855–866, 1971.

[144] A. E. Conrady. Decentred Lens-Systems. *Monthly Notices of the Royal Astronomical Society*, 79(5):384–390, 03 1919. ISSN 0035-8711. doi: 10.1093/mnras/79.5.384. URL https://doi.org/10.1093/mnras/79.5.384.

[145] S M Soloff, R J Adrian, and Z-C Liu. Distortion compensation for generalized stereoscopic particle image velocimetry. *Measurement Science and Technology*, 8(12):1441–1454, dec 1997. doi: 10.1088/0957-0233/8/12/008. URL https://doi.org/10.1088/0957-0233/8/12/008.

[146] F. Scarano, L. David, M. Bsibsi, and D. Calluaud. S-PIV comparative assessment: image dewarping+misalignment correction and pinhole+geometric back projection. *Experiments in Fluids*, 39(2):257–266, aug 2005. ISSN 0723-4864. doi: 10.1007/s00348-005-1000-x. URL http://link.springer.com/10.1007/s00348-005-1000-x.

[147] Tianshu Liu, L. N. Cattafesta, R. H. Radeztsky, and A. W. Burner. Photogrammetry Applied to Wind-Tunnel Testing. *AIAA Journal*, 38(6):964–971, jun 2000. ISSN 0001-1452. doi: 10.2514/2.1079. URL https://arc.aiaa.org/doi/10.2514/2.1079.

[148] F Scarano, L David, M Bsibsi, and D Calluaud. S-piv comparative assessment: image dewarping+ misalignment correction and pinhole+ geometric back projection. *Experiments in fluids*, 39(2):257–266, 2005.

[149] Callum Atkinson and Julio Soria. An efficient simultaneous reconstruction technique for tomographic particle image velocimetry. *Experiments in Fluids*, 47(4-5):553–568, oct 2009. ISSN 0723-4864. doi: 10.1007/s00348-009-0728-0. URL http://link.springer.com/10.1007/s00348-009-0728-0.

[150] Christian Willert. Stereoscopic digital particle image velocimetry for application in wind tunnel flows. *Measurement science and technology*, 8(12):1465, 1997.

[151] Kenneth Levenberg. A method for the solution of certain non-linear problems in least squares. *Quart. Appl. Math.*, 2:164–168, 1944. doi: 10.1090/qam/10666.

[152] Zhongwei Tang, Rafael Grompone Von Gioi, Pascal Monasse, and Jean-Michel Morel. A Precision Analysis of Camera Distortion Models. *IEEE Transactions on Image Processing*, 26(6):2694 – 2704, March 2017. doi: 10.1109/TIP.2017.2686001. URL https://hal-enpc.archives-ouvertes.fr/hal-01556898.

[153] A. K. Prasad, R. J. Adrian, C. C. Landreth, and P. W. Offutt. Effect of resolution on the speed and accuracy of particle image velocimetry interrogation. *Experiments in Fluids*, 13(2-3):105–116, jun 1992. ISSN 0723-4864. doi: 10.1007/BF00218156. URL http://link.springer.com/10.1007/BF00218156.

[154] Juan A. Sillero, Javier Jiménez, and Robert D. Moser. Two-point statistics for turbulent boundary layers and channels at reynolds numbers up to $\delta + \approx 2000$. *Physics of Fluids*, 26(10):105–109, 2014. doi: 10.1063/1.4899259.

[155] Philip Holmes, John L. Lumley, and Gal Berkooz. *Turbulence, Coherent Structures, Dynamical Systems and Symmetry*. Cambridge University Press, oct 1996. ISBN 9780521551427. doi: 10.1017/CBO9780511622700. URL https://www.cambridge.org/core/product/identifier/9780511622700/type/book.

[156] Robert D. Moser and Parviz Moin. Characteristic-eddy decomposition of turbulence in a channel. *Journal of Fluid Mechanics*, 200:471–509, 1989. ISSN 14697645. doi: 10.1017/S0022112089000741.

[157] K. Oberleithner, M. Sieber, C. N. Nayeri, C. O. Paschereit, C. Petz, H. C. Hege, B. R. Noack, and I. Wygnanski. Three-dimensional coherent structures in a swirling jet undergoing vortex breakdown: Stability analysis and empirical mode construction. *Journal of Fluid Mechanics*, 679:383–414, 2011. ISSN 00221120. doi: 10.1017/jfm.2011.141.

[158] J. P. Bonnet, D. R. Cole, J. Delville, M. N. Glauser, and L. S. Ukeiley. Stochastic estimation and proper orthogonal decomposition: Complementary techniques for identifying structure. *Experiments in Fluids*, 17(5):307–314, 1994. ISSN 07234864. doi: 10.1007/BF01874409.

[159] Leo H. O. Hellström, Ivan Marusic, and Alexander J. Smits. Self-similarity of the large-scale motions in turbulent pipe flow. *Journal of Fluid Mechanics*, 792:R1, apr 2016. ISSN 0022-1120. doi: 10.1017/jfm.2016.100. URL https://www.cambridge.org/core/product/identifier/S0022112016001002/type/journal_article.

[160] B.J Balakumar and R.J Adrian. Large- and very-large-scale motions in channel and boundary-layer flows. *Philosophical Transactions of the Royal Society A: Mathematical, Physical and Engineering Sciences*, 365(1852):665–681, mar 2007. ISSN 1364-503X. doi: 10.1098/rsta.2006.1940. URL https://royalsocietypublishing.org/doi/10.1098/rsta.2006.1940.

[161] Lawrence Sirovich. Turbulence and the dynamics of coherent structures. I. Coherent structures. *Quarterly of Applied Mathematics*, 45(3):561–571, 1987. ISSN 0033-569X. doi: 10.1090/qam/910462.

[162] George C. Sherman. Application of the Convolution Theorem to Rayleigh's Integral Formulas. *Journal of the Optical Society of America*, 57(4):546, apr 1967. ISSN 0030-3941. doi: 10.1364/JOSA.57.000546. URL https://www.osapublishing.org/abstract.cfm?URI=josa-57-4-546.